UNIVERSITÀ DEGLI STUDI DI PARMA

DIPARTIMENTO DI FISICA

Transport phenomena in X and γ ray semi-insulator detector: A new charge correction approach

Massimiliano Zanichelli

Thesis submitted for the award of the degree of Ph.D. in Physics

Dottorato di Ricerca in Fisica

Supervisor: Dott. Maura Pavesi

XXI Ciclo – Gennaio 2010

Contents

TRANSPORT PHENOMENA IN X AND γ RAY SEMI-INSULATOR DETECTORS: A NEW CHARGE CORRECTION APPROACH

January 22, 2010

Abstract

This research is part of the broader project of study and application of II-VI semi-insulating materials and especially of Cadmium and Zinc Telluride ($Cd_{1-x}Zn_xTe$ $CdZnTe$ or CZT). The current interest about these ternary compounds, such as semi-insulating materials for high energy photon detectors is mainly due to their high energy-gap that makes these materials ideal for applications at room temperature avoiding noise problems due to leakage current. Within this class of materials CZT is particularly appreciated both for the high-stopping power, due to the high atomic number of its components and its crystal structure, and for the high transport properties if compared to those of similar semiconductors. For these reasons CZT arises as an ideal candidate for high energy detector. The applications are numerous in several areas as security and environmental monitoring, storage of radioactive materials, medical instrumentation, space applications, astrophysics and cosmology.
The problems of purity and homogeneity of the material are still far from being resolved. For this reason transport properties are still limited as compared to those of silicon, germanium and gallium arsenide, also in relation to the size of developed sensors (even several cubic centimeters). On increasing the photon energy the mean absorption depth arises with detriment of charge collection and spectroscopic property, with a consequent line broadening. In addition still persist difficulties regarding passivation and realization of contacts that could ensure low noise and an efficient charge collection.
The main purpose of this work is to study charge collection processes and signal deterioration causes, improving the growth process and identifying appropriate methodologies for charge deficit correction, in order to create an electronic circuitry for data acquisition and signal correction.
The experimental activity was focused on the study of material grown by the Technology Group of IMEM-CNR Institute of Parma. This material have been grown with B_2O_3 Vertical Bridgman technique and used to create high energy detectors (10-700keV). The work can be divided into three main parts:

1. The material characterization, by means of photo-induced current, $I-V$ characteristics and X and γ spectroscopy, to characterize the material and in particular to analyze bulk an superficial defects, impurity levels and the consequent transport properties in devices made by technology group of IMEM Institute.

2. The second one consists of theoretical model assessment to describe the material photo-response and the electronic read-out chain in order to obtain both the shape of the electronic signal and transport property informations. These model could be useful to correct the charge deficit through the information concerning the photon absorption depth in the crystal.

3. The third part concerns the development of data acquisition, filtering system and data elaboration.

After a brief introduction about the fundamental issues involved, we make a careful analysis of these three aspects mentioned above. Finally we will discuss the thesis conclusions and the possible developments of this research. Other complementary activities, that play a minor role in the this research, can be found in the appendix.

Chapter 1

Introduction

1.1 Thesis Subject

CZT My research activity mainly focuses on transport properties in Cadmium Zinc Telluride $Cd_{1-x}Zn_xTe$ (or more briefly CdZnTe or CZT). Semiconductor materials are preferred in radiation detection because of the higher radiation stopping-power, if compared with other systems, for example gas detectors, or scintillators.
The fundamental requirement for an high energy radiation detector are:

- High stopping-power. This property allows to obtain a good photon collection efficiency in small volumes.
- High resistivity, to reduce leakage current and then the noise associated.
- Low energy activation, to achieve good signals
- And finally, good transport properties, really important to obtain fast detector and also with spectroscopic properties.

CZT is an ideal candidate for these applications, indeed the high Z-number ad the crystallographic structure ensure an high stopping power, if compared with other semiconductor as Silicon, Germanium and Gallium Arsenide; moreover the energy gap near $1.6eV$ allows to obtain high resistivity materials with not too high energy activation ($5eV$ for couple electron-hole) while the state of art in CZT technology enables to achieve good but not jet excellent transport properties.

Charge Collection As already said, transport properties play a crucial role in radiation semiconductor detector. When an high energy photon collides with the crystal lattice, a number of couple electron-hole are generated proportionally to the photon energy. If we suppose the existence of an electric field inside the crystal, the two kind of carriers (electrons and holes) will be separated by them

and both will move to the respective collection electrodes with speed proportional to carrier mobility μ and field intensity. Moving to the electrodes, carriers induce, on these last ones, a charge proportional to the carrier displacement (as shown in figure 1.1) in according to the *Ramo-Shockley theorem* (R-S theorem) [1] [2]. This theorem states that the induced charge on whatever electrodes by an unitary charge motion is given by the integral of a "*weighting field*"along the charge path. The weighting field is a quantity with physical dimensions of a reciprocal length which measures the coupling between the carrier path and the electrode; it is determined only by the system geometry.
In their motion toward electrodes the carriers experience trapping phenomena, then the collected charge is, in general, lower than the generated charge because of the limited carrier life-time τ. This phenomenon becomes more noticeable increasing the distance between the photon impact and the collecting electrodes. So the charge collection efficiency becomes dependent on the photon-lattice impact position, then starting from two photons with same energy but different impact position, we will detect different amounts of charge.

1.1.1 Thesis structure

The thesis is composed of five chapters

Material In this first chapter we describe the material, its fundamental properties, the growing procedures and the the detector preparative. In particular we will underline the transport properties because they are fundamental for the further discussions.

Photocurrent and high energy Spectroscopy The second chapter concerns the experimental study of transport properties of CZT grown by the Technology Group of IMEM-CNR Institute of Parma with B_2O_3 encapsulated vertical Bridgmann technique. We characterize the material by means of photo-induced current, $I-V$ characteristics and X and γ spectroscopy, to evaluate the material resistivity, to analyze bulk and superficial defects and to reveal impurity levels. Moreover fitting the data arising from X and γ spectroscopy and photocurrent techniques with Hecht's and Many's equations[3] [4] it is also possible to get the mobility-lifetime product and information concerning the surface recombination rate.

Theoretical Models In the third chapter we discuss the mathematical models describing the signal generation carried out by the detector and read-out electronics. We modelize the transport phenomena resolving the Boltzmann's equation under different approximations. Similar efforts to calculate the density and the dynamic of free carriers have been done by Hecht [3], Zanio [5] et others [6] [7] and recently by Bale and Szeles [8] [9] [10] with a more general approach that takes in account the field perturbations due to the spatial charge. The screening effect of the spatial charge it has been faced also by Kubat and Franc

in [11] and [12]. From the electron and the hole transport dynamics, applying the R-S Theorem, we can calculate the induced charge and, finally, convolving with the read-out transfer function, the output signals. The obtained functional form depend on the time t and on the impact position $\vec{x}_0$ but also on the transport parameters, as mobility μ, life-time τ and detrapping-time τ_d both for electrons and holes, and on the circuital characteristic-times of the read-out electronic (in our case only the integration effective time τ_i).
These models can be useful both to correct the charge collected with the position information, improving the spectroscopy, and to obtain the transport parameters, fitting these curves on the experimental data.

Experimental Part The experimental part concerns the creation of a data acquisition and filtering system and also of the fitting programs to test the theoretical models. We started with the creation of an electronic read-out chain to shape the signal and we have came to an acquisition and filtering system implemented in Labview on two National Instrument digitizers. During this phase we have succeeded in reducing over ten times the noise level. A big effort has been performed to create the fitting programs. Indeed, as we will see later, because of both the number of fitting and the model complexity, the fundamental constraint is the efficiency in the numeric calculations: we have reduced the computation time more then 10000 times with respect the first version.

Discussions In this last section we present the preliminary results of data analysis. This part is already far to be completed, because of the difficulties to obtain low noisy data, for the fitting procedure. Some difficulties could came from the hypotheses. Indeed we have done two fundamental approximations in our calculations: the spatial uniformity of both the electric field (planar detector) and the transport properties. Later, in the last chapter we will hint at all these aspects and we discuss the perspectives of this work.

1.2 Physical background

In this section we deal with physical phenomena involved in the thesis, giving only the fundamental results and avoiding en excessive deepening.

1.2.1 Ramo-Shockley Theorem

The R-S theorem is a corollary of the classical electromagnetic theory. This theorem states that the induced charge $Q_i(t)$ on whatever electrode, due to the motion of a charge Q_0 is given by the variation of a "*weighting potential*" $W(\vec{x})$ along the unitary charge path in according with the relation.

$$Q_i(t) - Q_i(0) = Q_0 \left(W(\vec{x}(t) - W(\vec{x}(0))\right) \tag{1.1}$$

In the differential form we can write:

$$dQ = Q_0 \vec{w} \cdot \vec{dx} \tag{1.2}$$

then, for a semiconductor material, we can write $\vec{v} = \mu \vec{E}$ and we have:

$$I(t) = \frac{dQ}{dt} = Q_0 \vec{w} \cdot \vec{v} = Q_0 \vec{w} \cdot \mu \vec{E} \tag{1.3}$$

Where $\vec{w} = \nabla W$ is the "*weighting field*", $\vec{v}$ the carrier speed, μ the carrier mobility, and $\vec{E}$ the electric field. The weighting field (or potential) related to

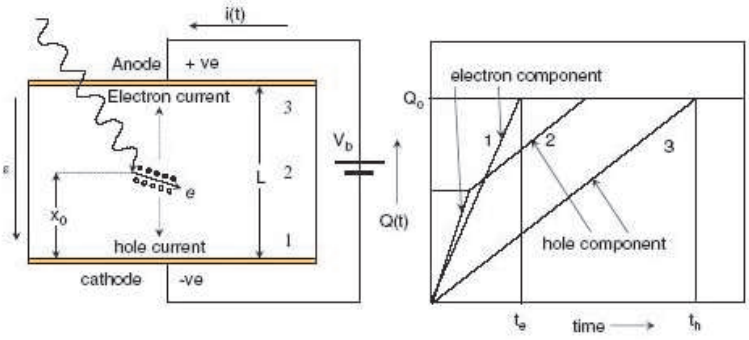

Figure 1.1: Electron and hole contributes to the charge collected by the sensor

the ith electrode can be calculated setting the electric potential of this electrode to $1V$ and placing the others to $0V$. It is very important to note that in general the weighting field is different from the electric field inside the semiconductor. A wider examination of this argument can be found in [13] and [14]

1.2.2 Interaction radiation-matter

When a photon flow $I(x)$ crosses an homogeneous medium, it will be reduced according to the relation

$$I(x) = I_0 e^{-\mu x} = I_0 e^{-\frac{x}{\lambda(\epsilon)}} \tag{1.4}$$

where x is the thickness of material crossed, λ is the attenuation length dependent on the photon energy ϵ and $\mu = \frac{1}{\lambda}$ is the attenuation coefficient. The photons during the path can loss energy or can be absorbed mainly because of three different processes:

- Photoelectric effect, It is overriding at low energies, when the photon energy is some times lower than the energy associated to the electron rest mass (i.e. for $h\nu < 200keV$).
- Compton effect, It is predominant when $h\nu$ is between $200keV$ and some MeV

- Electron-positron couple production, at very high energies, with a threshold of $2m_ec^2 = 1.022MeV$.

where m_e is the electron rest mass, h the Plank constant and c the light speed. For each ones of these different effect it is possible to define an energy dependent attenuation length that is proportional to the cross section of the involved process.

For the photoelectric effect, when the photon energy $h\nu$ is more greater than the energies involved with the K shell transitions, we can express the cross section as [15, 16]:

$$\sigma_{ph} = 4\sqrt{2}\sigma_T Z^5 \alpha^4 \left(\frac{m_e c^2}{h\nu}\right)^{\frac{7}{2}} \tag{1.5}$$

where $\sigma_T = \frac{8}{3}\pi r_e^2$ is the Thomson cross section with r_e classical electron radius, α the fine-structure constant and Z the atomic number. An analogous formulas is found for energies near the K_α and K_β lines, but depending on the 4th power of Z [15].

The total Compton cross section for low energies becomes the Thomson cross section while for energies $h\nu >> m_ec^2$ we have the Klain-Nishima limit:

$$\sigma_{KN} = \pi r_e^2 \frac{m_e c^2}{h\nu}\left[\ln\left(\frac{2h\nu}{m_e c^2}\right) + \frac{1}{2}\right] \tag{1.6}$$

A general formulas for couple e^-e^+ generation [15] is more complicated and not so useful in this contest because we even work under the couple generation threshold.

Because these phenomena do not exclude each others, it is possible to define a comprehensive attenuation length

$$\frac{1}{\lambda} = \frac{1}{\lambda_{ph}} + \frac{1}{\lambda_{comp}} + \frac{1}{\lambda_{cp}} \tag{1.7}$$

Often in place of using the attenuation length λ, it is employed the mass attenuation coefficient $\frac{\mu}{\rho}$, where ρ is the material density.
Especially when we deal with material composed by different elements (as in the CZT case), this form could be very useful, because the total mass attenuation coefficient can be calculated, in this way

$$\frac{\mu}{\rho}_T = \sum_i \omega_i \frac{\alpha_i}{\rho_i} \tag{1.8}$$

starting from those of the components, where ω_i are the relative weight fraction of the starting components.

Once an high energy photon has been absorbed or has transferred part of its energy to the crystal, this energy ionizes a number of electron-hole pairs proportional to the released energy, according to the relation

$$N_0 = \frac{h\nu}{E_{ion}} \tag{1.9}$$

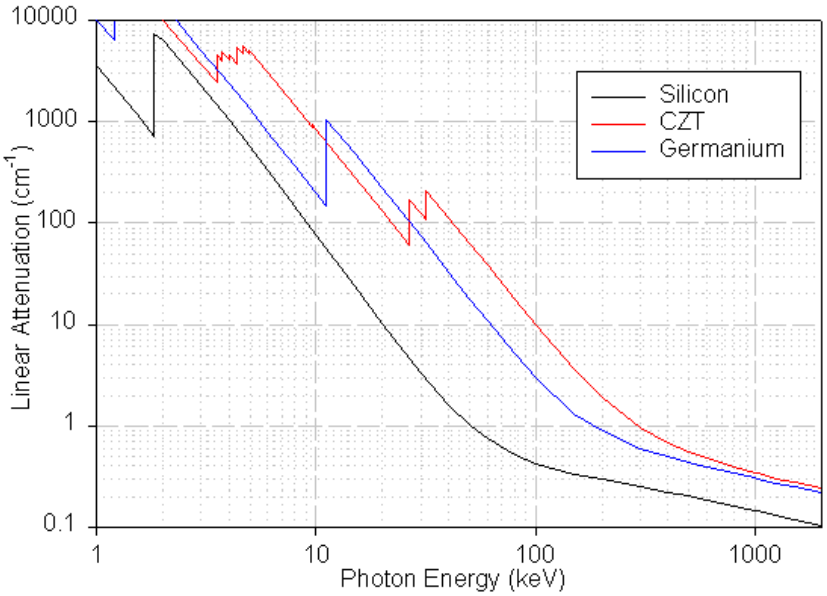

Figure 1.2: Comparison between the reciprocal attenuation lengths for Silicon (black), Germanium (blue) and CZT (red)

where E_{ion}, is the mean energy required to create an $e-h$ pair, follows the empirical relation

$$E_{ion} = 2.8E_G + 0.6 \tag{1.10}$$

For CZT with a zinc fraction of 0.1 at room temperature E_{ion} results to be $5.0eV$.

1.2.3 Semiconductor Physics

Current density In this section we want only resume some fundamental results in semiconductor physics. When an electric field $\vec{E}$ is present inside a semiconductor, the total current density $\vec{J}$ follows the relation

$$\begin{aligned} \vec{J} &= \vec{J_e} + \vec{J_h} = \\ &= (\sigma_{\mathbf{e}} + \sigma_{\mathbf{h}})\vec{E} = \sigma\vec{E} \end{aligned} \tag{1.11}$$

where σ and $\sigma_{\approx}$ are the conductivity tensors for electrons and holes. For an isotropic material σ and $\sigma_{\approx}$ are scalars and

$$\sigma_e = en\mu_e \tag{1.12}$$

$$\sigma_h = ep\mu_h \tag{1.13}$$

with

$$\mu = \frac{e\tau}{m_c^*} \tag{1.14}$$

where n, p, μ_e and μ_p are respectively the density of electrons and holes and the relative mobilities, e is the electron charge and m_c^* the carrier effective mass. Considering also the diffusion term for each current component J_c we can write:

$$\vec{J_c} = \rho_c \mu_c \vec{E} - \kappa D_c \vec{\nabla} \rho_c \tag{1.15}$$

where D_c is the diffusion coefficient and κ is the carrier sign ($+1$ in the hole case and -1 in the electron one). The resistivity value is defined by the relation

$$\rho = \frac{1}{\sigma} \tag{1.16}$$

Semiconductor in thermal equilibrium In thermal equilibrium we can obtain these quantity from the relations

$$\begin{aligned} n(T) &= N_C exp\left\{-\frac{E_C - E_F}{KT}\right\} = \\ &= 2\left(\frac{2\pi m_e^* KT}{h^2}\right)^{\frac{3}{2}} exp\left\{-\frac{E_C - E_F}{KT}\right\} \end{aligned} \tag{1.17}$$

and

$$\begin{aligned} p(T) &= N_V exp\left\{-\frac{E_F - E_V}{KT}\right\} = \\ &= 2\left(\frac{2\pi m_h^* KT}{h^2}\right)^{\frac{3}{2}} exp\left\{-\frac{E_F - E_V}{KT}\right\} \end{aligned} \tag{1.18}$$

from which

$$\begin{aligned} n(T)p(T) &= N_C N_V exp\left\{-\frac{E_C - E_V}{KT}\right\} = \\ &= 4\left(\frac{2\pi}{h^2}\sqrt{m_e^* m_h^*} KT\right)^3 exp\left\{-\frac{E_G}{KT}\right\} \end{aligned} \tag{1.19}$$

For an intrinsic material $n(T) = p(T)$, then

$$\begin{aligned} n_i^2(T) &= p_i^2(T) = n(T)p(T) = \\ &= N_C N_V exp\left\{-\frac{E_G}{KT}\right\} \end{aligned} \tag{1.20}$$

from which:

$$n_i(T) = p_i(T) =$$

$$= 2\left(\frac{2\pi m_0^*}{h^2}\sqrt{\frac{m_e^* m_h^*}{m_0^{*2}}}KT\right)^{\frac{3}{2}} exp\left\{-\frac{E_G}{2KT}\right\} \tag{1.21}$$

Boltzmann equation and transport properties The general description of transport phenomena in semiconductors is given by the Boltzmann equation.

$$\frac{\partial \rho}{\partial t} = G - U - \vec{\nabla} \cdot \vec{J} \tag{1.22}$$

This equation is a generalized continuity equation, to include the generation and destruction (trapping and recombination) processes in the description of electric transport phenomena. G and U indeed are respectively the generation and the destruction rate (i.e. the number of carriers generated or destroyed in a unitary volume per second) and $\vec{J}$ is the current density. Because of the recombination process, in semiconductors we have two coupled Boltzmann equations: one for the electrons and another for the holes. If we consider an intrinsic semi-insulator material the recombination processes are negligible because normally we have $\Delta n = \Delta p >> n_i = p_i$; then we can considerate separately the two equations.

Charge losses Let's suppose to give at the time $t = 0$ an excess of carrier $\Delta n = \Delta p >> n_i = p_i$ so that we can neglect n_i and p_i. Due to the limited values of carrier transport properties μ and τ, the carriers experience a damping processes that quench the carrier excess. These processes are trapping, detrapping and recombination. If we suppose no detrapping processes we can suppose that the excess of free decays exponentially to zero. Instead in absence of recombination processes, but in presence of detrapping, theoretically an excess of free carrier survives until their complete collection and with an infinite integration time we should collect all the generated carriers. In practice this situation never occurs and the system thermalizes in some characteristic time. Besides recombination and, above all, trapping and detrapping phenomena affect the system response, mainly because of the finite integration time of the read-out electronics causing charge losses in particular when the collecting time creases. The fundamental parameters involved in the time response of a material are the carrier mobilities μ_e and μ_h (being related to the carrier speeds and then the detector response time), the trapping times τ_{te} and τ_{th}, the detrapping times τ_{de} and τ_{dh}, and the recombination time τ_r.
In the further chapters we re-discuss all these aspects facing the problem of a possible modelization to describe the signal generation.

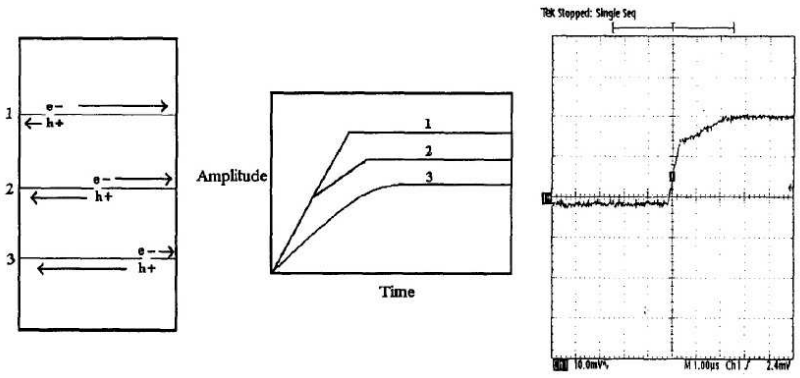

Figure 1.3: Charge pulses at different absorption depth

Chapter 2

Material

2.1 Overview

Cadmium Zinc Telluride (CdZnTe or CZT) is a ternary alloy of II-VI semiconductor family. Indeed Tellurium is an element of VI° group while Zinc and Cadmium are transition metals with the shell d totally filled and then properties similar to the II° group ones. The atomic number of these three elements are respectively 52, 48 and 30. These high atomic numbers ensure a very high stopping power. In fact the stopping power is proportional to Z^{γ}, where the value of γ is between 4 and 5. Normally the CZT employed in radiation detectors has a fraction of zinc not larger than 0.2 (normalizing the sum of Zinc and Cadmium atom fraction to 1). This involves, as we will see later, an energy gap of about $1.5 - 1.6eV$ and then the possibility to ensure a very low leakage current once compensated. An other important feature is the good transport properties in comparison with other similar semiconductor.

2.1.1 CZT as a Radiation Detector

CZT realize a good compromise between several important properties for a radiation detector material:

- High stopping power
- Achievable semi-insulator characteristics (very high resistivity, over 10^{10} Ωcm).
- Environmental working temperature (High bandgap)
- Good transport properties.

All these characteristics make CZT ideal for radiation detection aims.

2.1.2 Crystallographic and Band Structure

CZT inherits from both CdTe and ZnTe compounds several properties, as crystallographic cubic zincblende and band structure. The alloy $Cd_{1-x}Zn_xTe$ can be ideally regarded as a CdTe crystal with Zn atoms randomly substituted for a fraction x of Cd atoms. The differences in the lattice constants and in the gap energy of CdTe and ZnTe imply that this substitution is accompanied by some change in the average unit cell dimension and in the gap magnitude.
Regarding the crystal structure, Vegard's law [17] give us a good lattice constant linear approximation:

$$a(x) = a_1 x + a_2(1 - x) \tag{2.1}$$

where a_1 and a_2 are respectively the lattice constant of ZnTe and CdTe.
About the band structure we can note that the band structure CdTe and ZnTe are quite similar. Both semiconductors, indeed, presents direct bandgaps of magnitude respectively of $1.5eV$ and $2.2eV$ at room temperature. CZT inherits this characteristic and its energy gap increases with parabolic characteristic between these two values on varying the Zn fraction from 0 to 1.
The direct bandgap makes these compounds interesting for optical applications and also very sensitive to optical stimulations, so that, optical characterization techniques, as photoluminescence and photocurrent, are ideal to study their properties.
Concerning the CdTe and ZnTe structure, there are four valence bands to accommodate the eight valence electrons for primitive cell. The degeneracy of heavy-hole and light-hole bands and the degeneracy at $k = 0$ of the split-of band with the heavy-hole and light-hole bands, are removed by spin-orbit interaction. Because of the spherical shape of the constant energy surface, the effective masses are given simply by the reciprocal of the curvature of energy band in k-space at $k = 0$:

$$\frac{1}{m^*} = \left(\frac{2\pi}{h}\right)^2 \frac{\partial^2 E}{\partial k^2} \tag{2.2}$$

Both CdTe and ZnTe have relatively low effective masses for electrons, giving reasonably good transport properties. For holes we must remember that there are several effective masses, one for each different band. In this case it is possible to define an average effective mass. In particular we have two different average masses, one regarding the states density

$$m^*_{dh} = \left({m^*_{hh}}^{3/2} + {m^*_{lh}}^{3/2}\right)^{\frac{2}{3}}$$

and the other regarding the transport phenomena

$$m^*_{ch} = \frac{{m^*_{dh}}^{3/2}}{{m^*_{hh}}^{1/2} + {m^*_{lh}}^{1/2}}$$

where m^*_{hh} and m^*_{lh} are respectively the heavy-hole and the light-hole effective masses. The question of the band structure of $Cd_{1-x}Zn_xTe$ or any ternary

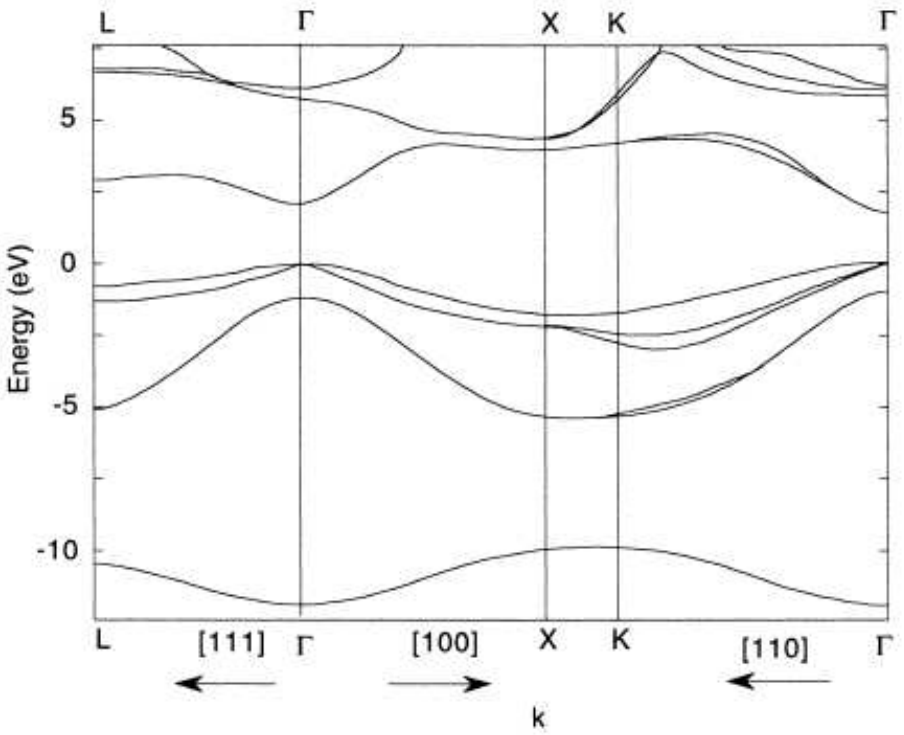

Figure 2.1: CdTe Band structure

semiconductor is a fairly difficult one, because the translational simmetry is broken by the local composition fluctuations. A starting point for the calculations is that the crystal potential is a linear interpolation between those of the two constituents. This implies that the bandgap should vary linearly with the zinc concentration. As we have already said the $E_g(x)$ function (energy gap on varying the Zn fraction) is always found with some curvature and can usually be fitted to a quadratic curve. An empirical expression of $E_g(x,T)$ in eV is given by

$$\begin{aligned} E_g(x) &= E_0(T) + (\Delta E - a)x + ax^2 = \\ &= 1.606 + 0.38x + 0.463x^2 - \frac{4.510^{-4}T^2}{264+T} \end{aligned} \tag{2.3}$$

Where T is the temperature in K, the constant term is the gap value for CdTe at $0K$, the linear coefficient ΔE is the Energy gap difference between ZnTe and CdTe, and the quadratic coefficient a is called *bowing parameter* and arises from short-range disorder [18].

2.2 Defects

As reminded in the introduction in the equation 1.21, for an ideal intrinsic semiconductor the concentration of free electron n equals the concentration of free holes p, so we can write

$$np = n^2 = p^2 = N_c N_v \exp\left\{-\frac{E_g}{KT}\right\}$$

where

$$\begin{aligned} N_c &= 2\left(\frac{2\pi m_e^* KT}{h^2}\right)^{\frac{3}{2}} \\ N_v &= 2\left(\frac{2\pi m_h^* KT}{h^2}\right)^{\frac{3}{2}} \end{aligned}$$

The values obtained for n at $300K$ is $6.9 \cdot 10^5 cm^{-3}$ and starting from theoretical calculations it could be possible achieve resistivity values of about $10^8 \Omega \cdot cm$, but in reality it is hard achieve values greater than $10^6 \Omega \cdot cm$ without compensation with some kind of dopant as indium or chlorine.
At room temperature, indeed the conduction is due to native defects present in the crystal. Then we'll take into account mainly those defects that affects the transport properties. Those can be divided, principally, in three families:

- Structural defects like vacancies, interstitial, anti-sites, cracks, dislocations, and precipitates.
- Dopant impurities embodied in the crystal.
- Point structural defects bound to impurity states (e.g. A center).

In the first case the most important defects affecting the detector behavior are cadmium vacancy V_{Cd}, interstitial cadmium Cd_i and tellurium anti-site Te_{Cd}. The cadmium vacancy is responsible for two acceptor levels

$$V_{Cd} + e^- \rightarrow V_{Cd}^-$$

$$V_{Cd}^- + e^- \rightarrow V_{Cd}^{2-}$$

associated by Szeles [19] to two energy levels at $130meV$ and $210meV$ under the conduction band edge. The concentration of these two defects is correlated to the growth technique carried out starting from a Tellurium-enriched melt. As we'll see this tellurium excess is really important in the compensation process. In the same way the interstitial cadmium give two donor levels

$$Cd_i \rightarrow Cd_i^+ + e^-$$

$$Cd_i^+ \rightarrow Cd_i^{2+} + e^-$$

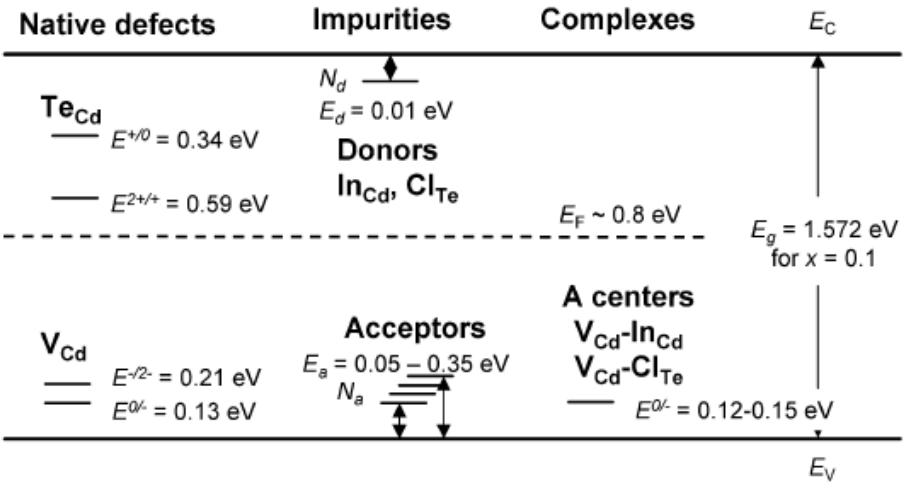

Figure 2.2: Defect levels in CZT crystals reported in [19]

The tellurium anti-site defect introduces a trap level at $0.59eV$ under the conduction band and it seems to be fundamental to lock the Fermi level near the mid-gap.

A comment about cracks, dislocations and precipitates is due. Cracks result mostly from thermal stress, most likely during the crystal call down and were found to have a direct correlation to the leakage current; regions along and near the cracks exhibit as much as three orders of magnitude higher leakage current than regions away from the cracks. The enhanced leakage current along the cracks is most likely originated from the impurities, tellurium or processing solutions which can decorate or infiltrate the cracks [17].

The dislocations and precipitates arise from thermal stress, stoichiometric deviation, and crystal disorder. The former could interact together to create grain boundaries while the latter, mainly constitute of tellurium in excess, produce low-resistivity regions in the crystal (tellurium has a low resistivity because of its low band-gap of $0.33eV$). In particular precipitates concentrate themselves in correspondence of other defect or grain boundaries creating low resistivity path; both can be reduced with a thermal annealing. For CZT, especially when grown by the high-pressure Bridgman method, most of the impurities in CZT have segregation coefficients that are less than one (e.g. Li, Na, Ca, Cr, Fe, Mn, Ni, Ag, In, Sn, Sb, Tl, Bi, P, Ti, V, Si, Pb, Cu, and Ga), which leads to an accumulation of the impurities in the last-to-freeze section of the ingot [17]. As a consequence of the segregation of impurities the crystal quality is often degraded in the portion near the heel. The presence of impurities and defect inside the CdZnTe as-grown involves the addiction of dopant into the starting materials to make intrinsic the semiconductor. For this reason in semi-insulators the major impurities contribution is due to the dopant, normally used to compensate

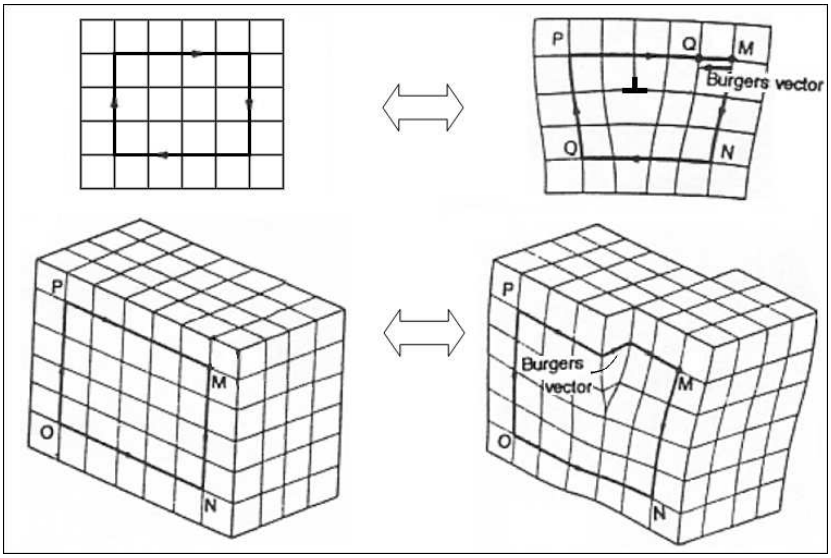

Figure 2.3: Dislocations

the semiconductor (i.e. indium and chlorine). These two elements, substituting respectively cadmium and tellurium, act as donors giving shallow levels with ionization energy around $10mV$ under the conduction band.
Interesting are also complexes between punctual structural defects and impurities, like A-center $(V_{Cd}^{2-}, D^{+})^{-}$ involved in the auto-compensation mechanism, where D is the dopant element. Our samples are $CdZnTe : In$ and in this case the A-center is localized in the range $120 - 150mV$ [19] above the valence band: then it behaves as an acceptor level.

2.3 Compensation and Auto-Compensation

For radiation detector materials the minimalum acceptable resistivity is approximately $10^{8}\Omega cm$ and $10^{9}\Omega cm$ or above is desirable. For this reason the synthesis starts from very high purity components and, because of native defects and residual impurities, continues with the introduction of dopant to compensate the material. To compensate a semiconductor there must be a mechanism by which it is possible achieve a delicate balance between donors and acceptors, or, in an other way, the presence of deep level to pin the Fermi level in the mid-gap neighborhood. To compensate the semiconductor in absence of any other defect near the mid-gap it is necessary that the concentration of center D^{+} equals the concentration of V_{Cd}^{2-} with good approximation. Indeed, because of in the intrinsic CZT there is a free carrier concentration of about $7 \cdot 10^{5}cm^{-3}$ and the chemical impurity concentration of starting materials is about $10^{16}cm^{-3}$ we

should obtain at least a balance of one part for 10^{10}. For this reason it is generally accepted that high resistivity in CZT is achieved through a balance between deep levels and shallow donors. The presence in CZT of some kind of defect as Te_{Cd} near the mid-gap with a concentration of almost $10^{14}cm^{-3}$ makes things better, but it is not yet enough. Indeed the dopant concentration that we can control is at most $10^{16}cm^{-3}$. There must be another mechanism involved in compensation of CZT crystals. This mechanism is named auto-compensation and it has not yet definitively explained. For Indium doped CZT the native ingots are p-type semiconductors. At the beginning, increasing the dopant concentration (Indium is a donor) we increase the free electron one, obtaining a semi-insulator characteristic. Boosting beyond the ingots indium content increase the number of neutral complexes $(V_{Cd}^{-}In^{+})^{0}$ and $(V_{Cd}^{2-}2In^{+})^{0}$ and, more again, the concentration of charge complex $(V_{Cd}^{2-}In^{+})^{-}$ to the detriment of the V_{Cd}^{2-} and V_{Cd}^{-} defect density. The last complex is called A-center and plays a role of acceptor; so the deep levels can more easily fix the Fermi energy near the mid-gap, and we can obtain a CZT with semi-insulator characteristics.

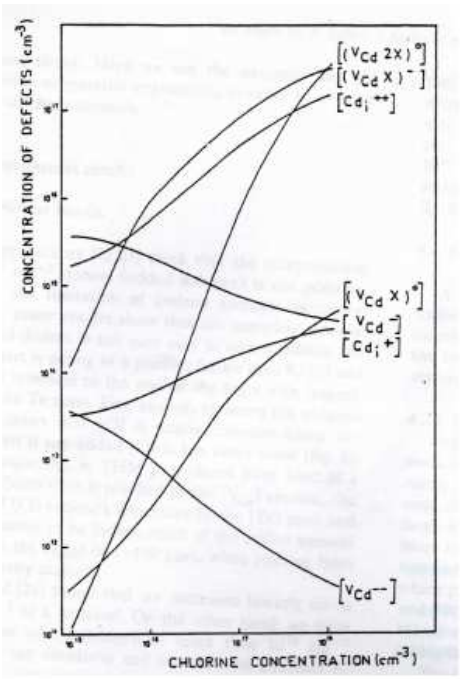

Figure 2.4: Defects concentration on varying the temperature

2.4 Growing Methods

A number of methods have been successfully employed in the growth of CdZnTe for substrate applications, including the traveling wave heater Bridgman physical vapor growth and vapor phase epitaxy [17].
The Bridgman method is actually the most employed for growing the CZT crystal. It involves the movement of a crucible containing the melt through a furnace designed to provide a suitable temperature profile. The furnace may be either vertical or horizontal. The crucible may be transported through the heater, or the crucible is stationary with a moving heater, or alternatively, both stationary and the temperature profile altered by a programmed temperature controller. Detailed description of this method and its variants are available in literature, for example in [17].

2.4.1 B_2O_3 Encapsulated Vertical Bridgman

The method employed to grow our CZT detector is a low pressure vertical Bridgman modified, developed by the technology group of IMEM-CNR institute of Parma. In the next paragraph below, we report the description of method used to grow our materials as described by Zappettini et all in [20].

Growth The charge material is pre-synthesized starting from 7N (Cd) and 6N (Zn) elements according to a process described elsewhere [21]. After the synthesis, the charge is heat-treated at about $870°C$ in order to obtain a reproducible charge composition. The pre-synthesized material is charged inside a quartz ampoule and covered by a boron oxide pellet (water content: $200ppm$, 99.9995% nominal purity). The growth apparatus is shown in Fig. 2.5. When the furnace is heated up, the boron oxide melts and covers the crystal. The growth chamber is pressurized to 5–10 atm in order to avoid the charge decomposition. Finally, the charge is melted and the growth procedure starts. After the growth, the crystal is easily removed from the crucible by putting it into water: the boron oxide dilates, breaks the quartz ampoule and the crystal can be easily removed. No significant difference was ever found between the weight of the polycrystalline charge and of the grown crystal. This means that the encapsulation by means of boron oxide is effective in avoiding material decomposition during the growth. In Fig. 2.6 two inch crystals are shown. The crystals show shiny surfaces that are uncommon in the case of the growth of CdZnTe by vertical Bridgman. Moreover, a closer look at Fig. 2.6 reveals that the surface of the crystal is characterized by rings normal to the growth direction, that are typical of the crystals grown free from the contact with a crucible, as in the case of the Czochralski growth.
Also, the CZT crystals grown in untreated quartz ampoules are known to suffer the problem of sticking to the crucible, which is considered one of the causes for the formation of spurious nuclei. On the contrary, we did not observe any trace of sticking in our crystals. These characteristics can be explained if we make the hypothesis that boron oxide not only covers the top of the melt, but also

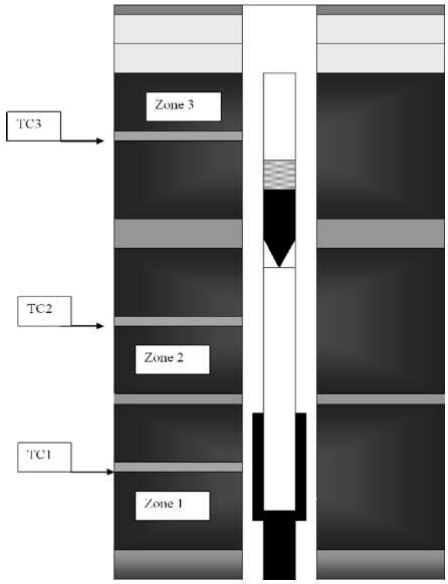

Figure 2.5: Boron oxide vertical Bridgman apparatus

Figure 2.6: 2-inch crystal grown by B_2O_3 encapsulated vertical Bridgman apparatus

fully encapsulates the melt. In order to confirm this point, in Fig. 2.7 crystal only partially removed from the growth crucibles are shown. Traces of boron oxide are clearly visible on the crystal surface and between the crystal and the crucible walls.

The boron oxide layer is about 100–150μm thick, both in the case of 1-inch and 2-inch crystals. Crystals with large single grains were grown also using quartz crucibles (Fig. 2.8). This is a proof of the effectiveness of the full encapsulation, as it is known that it is difficult to obtain good crystals in quartz ampoules:

Figure 2.7: A CdZnTe crystal still partially inside the quartz crucible

this is the reason why people usually cover the quartz ampoules with a graphite layer.

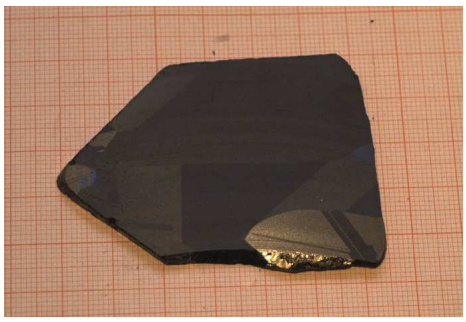

Figure 2.8: A section of CdZnTe crystal. Some large grains are distinguishable.

Etch Pit Density (EPD) Thanks to the boron oxide layer that fully encapsulates the melt, the crystal grows without a direct contact with the quartz wall. Moreover, due to the fact that the boron oxide layer solidifies at a temperature (about 500) much lower than the melting temperature of the crystal, the crystal does not suffer the mechanical stress from the crucible walls during the cooling due to the different thermal expansion of the crystal and the quartz. Thus, it is expected that the dislocation density of the crystal grown fully encapsulated in boron oxide is lower than usually reported for CdZnTe crystals. In order to verify this point we have cut large single grains parallel to the (111) plane and the etch pit density has been determined by means of the Nakagawa etching.
Fig. 2.9 shows the typical etch pit pattern. The EPD value determined was as low as 1.5 which is at least one order of magnitude lower than the state of the art values. The etch pit distribution does not present aggregates: on the contrary the pits seem to be homogeneously distributed.

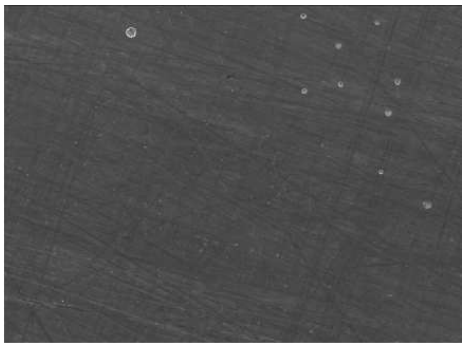

Figure 2.9: Etching pattern for CdZnTe wafer. The area of the picture is about $1mm^2$

Doping The resistivity of the samples was measured using current/voltage measurements by the four probes method. Undoped samples showed resistivity values in the range $10^4 - 10^5 \Omega cm$. In order to obtain high resistivity material, useful for detector preparation, the crystals were doped with indium in $10^{16} - 10^{17}$ $atoms/cm^3$ range. In this way, crystals with resistivity up to $10^{10}\Omega cm$ were achieved.

2.5 Transport Properties

One of the great advantages of CdTe compared to other high-Z materials is its relatively high electron mobility ($1100 \frac{cm^2}{Vs}$ at $300K$). The hole mobility, on the other hand, is about 10 times lower. The CZT case is quite similar: the electron mobility is comparable to that of CdTe, while the hole mobility is somewhat lower. but offers the advantage of an increased resistivity. Ideally carrier mobilities can be calculated from the scattering rates for phonon, impurity and alloy scattering. Suzuki et al. [23] found that for $Cd_{0.8}Zn_{0.2}Te : Cl$ the hole mobility was limited by trapping-detrapping processes involving the A-centers $(V_{Cd}^{2-}Cl^{+})^{-}$ About the dependence of the carrier mobilities on alloy composition, two factors are relevant: first, the alloy scattering rate varies as $x(1-x)$; second, all scattering rates increase with the effective mass of the carrier, which in turn increases with bandgap. Therefore we must do a compromise between two tendencies: x must be as small as possible to maximize the $\mu\tau$ product but large enough to increase the resistivity.
In principle it is always possible to define a mean life time τ for a kind of carrier. In the holes case take place some additionally difficulties because of the several bands which the holes can belong to. We should define several mean life-times, but, if we could define a mean mobility for these carrier, there is no more reason to keep this distinctions in the life-time.
As already pointed out about the band structure, it is really difficult define rigor-

ously the mobility in CZT for at least two reason. The first one is that mobility definition involves the effectiveness mass an then bands curvature according to the relation

$$\mu = \frac{e}{m^*}\langle\tau\rangle \tag{2.4}$$

where

$$\frac{1}{m^*} = \left(\frac{2\pi}{h}\right)^2 \frac{\partial^2 E}{\partial k^2}$$

and the bands are not well-defined entities in an alloy, being affected by local stoichiometric deviations. The second one is that, in the hole case, we have four several bands with two different curvatures. For these two reason we can define, with some approximations, only a mean mobility ignoring, in the hole case, inter-band scattering. The calculation result [22] for this last case is given by

$$\mu_h = \frac{\mu_{hh} + \mu_{lh}\left(\frac{m^*_{hh}}{m^*_{lh}}\right)^{\frac{3}{2}}}{1 + \left(\frac{m^*_{hh}}{m^*_{lh}}\right)^{\frac{3}{2}}} \tag{2.5}$$

μ_e (cm^2/V s)	μ_h (cm^2/V s)	$(\mu\tau)_e$ (cm^2/V)	$(\mu\tau)_h$ (cm^2/V)	x	Reference
1000–1100	50	8×10^{-4}–8×10^{-3}	3×10^{-6}–3×10^{-5}	0.1	[249]
1000	7	–	2.8×10^{-5}	–	[250]
–	–	4×10^{-4}	8×10^{-5}	0.1	[229]
1050	90	6×10^{-4}	3×10^{-5}		[78]
880	51	–	–	0.2	[183]
1000	50	4×10^{-3}	9×10^{-5}		[10]
1350	120	–	–	0.2	[188]
1000–1300	–	$(2.4–8.9) \times 10^{-3}$	–	–	[251]
700–800	30–50	$(5–11) \times 10^{-3}$	$(2–8) \times 10^{-5}$	0.1	[43]

Figure 2.10: Selected transport properties of cadmium zinc telluride

To achieve a experimental evaluation of electrons and holes transport properties the most popular method is to fit with Hecht equation [3] the response of a planar detector under α-particle irradiation, on varying the applied bias, in condition of single-photon counting rate. Because the penetration depth of α-particles is only a few microns we select a single kind of carriers (either electrons or holes), then, fitting the data, we can use the single-particle Hecht relation [24]:

$$Q(V) = \frac{eN_0\mu\tau V}{L^2}\left[1 - \exp\left\{\frac{L^2}{\mu\tau V}\right\}\right] \tag{2.6}$$

where N_0 is the initial number of carriers, e the electron charge, L the detector thickness and V the applied bias. Inverting the bias polarity we can select either electrons or holes, and, from the fit procedure, achieve the $\mu\tau$ product value. This procedure is also implemented with X and γ ray spectroscopy, but in this case, according to the radiation penetration length, we will use either the single

carrier or the complete (two carriers) Hecht relation. A similar approximation is employed also with the photocurrent analysis, but in this case we don't work in single-photon counting. Because of the superficial recombination we must use the Many's relation [4] that takes in account these effects. We'll speck about of Many's relation widely in the next chapter, now we want only add that these methods allow us to obtain only the product $\mu\tau$ value, while the individual ones of μ and τ remain unknown. If we wont know both the values we must also know one of these, for example, the mobility ones. The mobility value can be obtained measuring the fly-time of carriers in the above described experiments. Indeed the fly-time is the temporal gap employed by the carriers to move across the whole detector thickness. In the constant-field hypothesis its value became

$$T_c = \frac{L}{\mu E} = \frac{L^2}{\mu V} \tag{2.7}$$

where we have used the relation $V = E \cdot L$ with E electrical field.
Once we knows the $\mu\tau$ product and the T_c values we can easily obtain also the τ value. Typical values for μ and τ are reported in the table below

2.6 Preparative and Contacts

Contacts are a very important issue, for radiation detectors. When the intrinsic resistivity of materials are lower than $10^8\ \Omega \cdot cm$, blocking contacts are preferred, in our case, where the intrinsic material resistivity can achieve values of almost $10^{11}\ \Omega cm$ ohmic contacts are ideal for many reasons and in particular to prevent the creation of spatial charge, and to not distort the electric field inside the detector ensuring a bigger active volume. A brief overview on the possibles kind of contacts it will be given in the next chapter, now we want only describe shortly the detector preparation process [25]. This process consists of five several step

- Cut and polishing. The first one by means of a diamond-coated steel wire saw and the second one by mechanical polishing with abrasive paper and 0.05 μm particle size alumina suspension.
- Two cleaning process. The first one after the polishing process by means of two subsequent baths with boiling toluene and isopropyl alcohol for about two minutes each one. The second with three hot baths in sequence with trichloroethylene, isopropyl alcohol, and acetone before the passivation and the deposition processes.
- Etching. The chemical treatment of surfaces consist of a two step procedure with a 2% bromine in methanol etching solution for three minutes followed by a mixed solution of 2% bromine in methanol, 20% lactic acid and ethylene glycol for thee minutes. These two steps are important to remove the superficial layers damaged by the previous mechanical actions. After each etching, samples were rinsed in methanol.

- Passivation. The surface oxidation is necessary because the etching baths leaves the detector surface enriched of Tellurium, increasing the superficial conductivity. Oxidation then minimizes the leakage current and also stabilizes the detector surface. The Oxidation process was carried out with a $10\%NH_4F$, $10\%H_2O_2$ solution for six minutes at room temperature.
- Contacts deposition. This last step can take place in two different way:
  - By chemical deposition with $AuCl_3$ watery solution. The result is normally a good contact with a strong adhesion and without stress for the material, but unstable in the course of time.
  - By metal evaporation. In this case $750\mathring{A}$ thick gold contacts are evaporated under ultra-high vacuum on CZT. The contacts are time-stables, but present low adhesion. To improve this characteristic it is found very helpful an annealing process, after the deposition for 70 hours at $80°C$.

After these process the detectors are contacted and ready to use.

Chapter 3

Photocurrent

As said in the introduction in the section 1.1.1, in this chapter we speak about the experimental activities performed to study the transport properties and the spectroscopic quality of our CZT crystals. Before discussing the experimental data it is necessary to give a brief introduction to the involved experimental techniques. After this introduction, we will describe the experimental setup and finally the experimental results. About the X and γ-ray spectroscopy we have already discussed in the introduction in the sections dedicated to the radiation-matter interaction and to detector signal generation; then here we give prominence to the photocurrent (PC) technique.

3.1 Contacts and I-V characteristics

Contacts In order to perform any electric measurement on a semiconductor detector it is mostly necessary to make electrical contacts on this material. There are three kinds of contacts as we can see in figure **??**:

- Blocking contacts. This kind of contact does not allow the charge injection from the electrode to the semiconductor; on the contrary, it increases its resistance with increasing the bias voltage so that the $I-V$ characteristic is sub-linear. This happens, for a n-type semiconductor, when the metal work function ϕ_M is greater than the semiconductor work function ϕ_S.

- Ohmic contacts. This is a good approximation when $\phi_M \approx \phi_S$ and, for low biases, when $\phi_M < \phi_S$ (for an n-type semiconductor). In this case the electrode effects are negligible and the $I-V$ characteristic is linear.

- Injecting contacts. This happens, for a n-type semiconductor, when $\phi_M < \phi_S$; in this case the contact injects carriers into the bulk material. For this reason at low bias, when are dominant the bulk carriers, the $I-V$ characteristic is linear while at high bias, when the injected carriers are dominant the current is dominated by the spatial charge and the $I-V$

characteristic becomes super-linear. Fundamental contributions to explain these $I-V$ characteristics are given by Lampert et al. [26–28], Ashley [29] and Baron [30].

In the case of a p-type semiconductor we must only reverse the inequalities involving ϕ_M and ϕ_S.
Concerning the contacts on CZT material major contributions have been made by Nemirovsky et al. in [32, 33]. Nemirowsky has investigated the effects of the contacts on CZT detector by studying the charge collection efficiency and the dark noise spectra of the detectors as a function of applied bias. In general for radiation detectors two kind of contacts are used:

- blocking contacts for low resistivity material because attenuate the leakage current
- and ohmic contacts for high resistivity materials, because they do not distort the detector internal field and do not reduce the detector active volume.

The kind of contact is important for photocurrent comprehension because, modifying the detector internal field, it is modified the photocurrent response. For further information about the contacts and the electric field into the crystal we signal [31, 34].

I-V and bulk resistivity In the first two cases (blocking and ohmic contacts), from $I-V$ characteristics it is also possible to obtain the value of bulk resistivity. As we can see in figure 3.2, in the case of the ohmic contacts the sample resistance is given trivially from the reciprocal of the $I-V$ angular coefficient, and from here it is possible achieve the resistivity with geometrical considerations. In the case of blocking contacts the bulk series resistance can be obtained from the $I-V$ slope in the limit of zero bias [18]. Indeed for an ideal Schottky barrier [34] is valid the following relation

$$I = I_s \exp\left\{\frac{q(V_b - IR_s)}{KT}\right\} \tag{3.1}$$

where I_s is the inverse saturation current, V_b the bias voltage and R_s the bulk material series resistance. Developing at the first order we obtain:

$$R_s(I \to 0) = \frac{V_b}{I} - \frac{KT}{qI_s} \tag{3.2}$$

In any case the minimum value of V_b/I is an over-estimation of R_s and so gives a superior limit for R_s.

3.2 Photocurrent theory

In this section we give a brief overview on the photo-conductivity phenomenon. A very short and schematic introduction to the argument could be represented by [36], but main references for this summary are [37–39].

3.2.1 Conductivity

As reported in the section 1.2.3, the relation between the internal electric field and the current density in a semiconductor material is given by

$$\begin{aligned} \vec{J} &= \sigma\vec{E} = \\ &= q(n\mu_{\mathbf{e}} + p\mu_{\mathbf{h}})\vec{E} \end{aligned} \tag{3.3}$$

where q is the electron charge. In general σ is a tensor, but because of CZT has isotropic transport properties, it will be considered as a scalar quantity. Now, following the Bube's example [37], for the sake of simplicity let's assume the case of one-carrier transport; in this case the conductivity can be written as

$$\sigma_0 = qn_0\mu_0 \tag{3.4}$$

When the material is illuminated, the conductivity is increased, so

$$\begin{aligned} \sigma &= \sigma_0 + \Delta\sigma = \\ &= q(n_0 + \Delta n)(\mu_0 + \Delta\mu) = \sigma_0 + q\left(n\Delta\mu + (n_0\Delta n)\mu_0\right) \end{aligned} \tag{3.5}$$

Because in equilibrium condition the carrier excess can be written as

$$\Delta n = G\tau \tag{3.6}$$

where G is the generation rate and τ the carrier life-time, we get

$$\Delta\sigma = q\mu_0 G\tau + qn\Delta\mu \tag{3.7}$$

So the conductivity could be modified because of three different mechanisms:

- Variation in the generation rate G .
- Variation of the mean life-time $\tau = \tau(G)$.
- variation of the mobility value $\mu = \mu(G)$.

When we deal with semi-insulator materials at sufficiently high photo-excitation rate we can write:

$$\sigma \approx \Delta\sigma = Gq(\mu_e\tau_e + \mu_h\tau_h) \tag{3.8}$$

3.2.2 Photocurrent models

As already said in the section 1.2.2, when a photon flux crosses any thickness of some material its intensity undergoes an exponential damping so the photogeneration rate can be expressed as:

$$G(x) = G_0 \exp\left\{-\frac{x}{\lambda(E)}\right\} \tag{3.9}$$

If we want calculate the expected photocurrent, we must start from the Boltzmann equation 1.22:

$$\frac{\partial n}{\partial t} = G - U - \vec{\nabla} \cdot \vec{J} \tag{3.10}$$

where

$$\vec{J} = n\mu\vec{E} - D\vec{\nabla}n \tag{3.11}$$

with D diffusion coefficient. Once we have the $n(x,t)$ solution, exploiting the Ramo-Shockley theorem (see the section 1.2.1), we can calculate the contribution to the current coming from each depth x ($L \geq x \geq 0$, where L is the detector thickness) and then integrating over all the thickness to get the photocurrent value. The procedure could be quite complicated (in the next chapter we will expose a similar calculation), but sometimes imposing some hypotheses, it is possible to achieve a simplify solutions as we will show in the next section. For further insights about the photocurrent theory refer to [37].

Many's model The attenuation length λ is an energy function and, for a semiconductor with direct bandgap as CZT, the attenuation length collapses when the photon energy reaches the value of the energy gap. At this wavelength or just above, the value of the attenuation length is in the order of some microns, so that the whole absorption process takes place in the surface layers. Supposing a planar geometry, the internal electric field becomes $E = V/L$ (where L is the detector thickness) and the problem can be dealt as one-dimensional. Moreover if we consider negligible the detrapping contribution and the diffusion current, we can write the stationary Boltzmann equation as in [40]:

$$\begin{aligned} G(x) &= G\exp\left\{-\frac{x}{\lambda}\right\} = \frac{\partial J}{\partial x} + \frac{n}{\tau} = \\ &= \mu E\frac{\partial n}{\partial x} + \frac{n}{\tau} \end{aligned} \tag{3.12}$$

Now introducing the hypothesis of strong light absorption, we can write $G(x)$ as

$$G(x) = G_0\delta(x) \tag{3.13}$$

this hypothesis is equivalent to put $G(x) = 0$ inside the material and to impose the boundary condition $G(0) = G_0$. It is noteworthy that G_0 and $G(x)$ have not identical physical dimensions; indeed the Dirac's delta function is not dimensionless. The physical dimensions of Dirac's delta are the reciprocal of its argument ones; this because the Dirac's delta is an integral object and then its integrated value must be dimensionless.
Because of the stationary conditions it should be

$$G_0 = n(0)\mu E + R_0 \tag{3.14}$$

If we suppose a surface recombination rate R_0 proportional to the carrier concentration

$$R_0 = n(0)s \tag{3.15}$$

where s is a constant called recombination speed[1], we can re-write the problem as:

$$\begin{cases} \mu E \frac{\partial n}{\partial x} + \frac{n}{\tau} = 0 \\ n(0) = \frac{G}{\mu E + s} \end{cases}$$

and we achieve the system solution

$$n(x) = \frac{G_0}{\mu E + s} \exp\left\{-\frac{x}{\mu \tau E}\right\} \tag{3.16}$$

where s has the physical dimensions of a velocity and is called surface recombination velocity. Applying the R-S theorem and remembering that, for a planar detector, the weighting field is equal to $\frac{1}{L}$, we can write the current density as

$$\begin{aligned} J &= q\frac{\mu E}{L}\int_0^L n(x)dx = \\ &= \frac{qG_0}{1+\frac{s}{\mu E}}\frac{\mu \tau E}{L}\left[1 - \exp\left\{-\frac{L}{\mu \tau E}\right\}\right] \end{aligned} \tag{3.17}$$

achieving in this way the Many's solution [4].

Modified models As underlined by Nemirowsky in [32], the internal electric field in the detector could be affected by the presence of spatial charge that polarizes the detector. In this case, the Many's equation could be not appropriated to fit the experimental data. This phenomenon, in very high resistivity material detector, is mainly due to the non-ideal contact quality. Recent studies (in particular the measurement of internal field through the Pockels-effect and the measures of local spectroscopy performed at the ESRF institute of Grenoble) have shown the presence, in some of our detector, of a non-uniform electric

[1] Its physical dimensions are a velocity.

field that drops to zero with a linear slope that intercepts the x-axis in $x = x_n$, starting from the negative electrode ($x = 0$). Moreover the Many's model, although is widely used in literature to fit the photocurrent data with good results [40, 53], it makes large approximations and the bigger one is that, in a steady state, the rate of trapped charge must be equal to the detrapping rate, so we cannot neglect the detrapping phenomena. For these reasons lately we have began to calculate some modified model to describe the new situations and fit the new data. The calculation are still in progress and this model is not still used to fit experimental data, so, for the sake of shortness, we describe only the fundamental idea of this work. The starting point is described by Franc and Kubat et al. in [11, 12]. Franc, Kubat et al. have developed a more accurate model for photocurrent description based on the steady state Boltzmann equation and the Hall-Shockley-Read model for recombination taking into account also the diffusion effects. The general solution has not an analytical finite form and it needs numerical methods.
We are developing a simplified model as a starting from the one-dimensional Boltzmann equation and ignoring the diffusion contribution. In the steady state the rate of trapping and detrapping processes must be equal, so we get a simplified Boltzmann equation given by

$$0 = G(x) - R(x) + D\frac{\partial^2 n_c}{\partial x^2} + k_c \mu_c \frac{\partial n_c E}{\partial x} \tag{3.18}$$

where μ_c is a positive constant and k_c is the carrier sign ($+1$ for the hole-case and -1 for the electron-case). If we neglect the diffusion current (that may becomes important only with high polarized detectors), supposing strong absorbed radiation and a recombination rate $R(x)$ negligible (because we are considering a semi-insulating material), the quantity $G(x) - R(x)$ can be considered as a boundary condition; indeed it is zero anywhere except for $x = 0$. In this condition the Boltzmann equation is further simplified and begins:

$$\mu_c \frac{\partial n_c E}{\partial x} = 0 \tag{3.19}$$

This equation states the continuity of the current through the material.
Now the third Maxwell's equation, for a one-dimensional system can be write as:

$$\frac{\partial E}{\partial x} = \frac{\rho}{\epsilon} \tag{3.20}$$

Where ϵ is the dielectric constant of the material and ρ the charge density that in first approximation (if we suppose no polarization due to the contacts or initial spatial charge) is given by the sum of drifting charge and trapped charge $kq(n + n_t)$

$$\rho = kq(n + n_t) = Kqn\left(1 + \frac{\tau_d}{\tau_t}\right) \tag{3.21}$$

In this approximation it is possible to solve the system constituted by the Boltzmann and the Maxwell equations to obtain the stationary field profile and the stationary carrier density. Besides when the internal field is dominated from other factors (for example polarization due to the contacts), if we know the field profile, supposing to not perturb too much the system, we can use the field profile to calculate the photocurrent profile on varying the bias. This is mainly true in the X and γ-ray spectroscopy because of the much lower photon flux. For this reason in this case we must use the non stationary Boltzmann equation (as well as in the case of the pulsed photocurrent[43]). These results have not yet a final form, in some case we have found an approximated formula, in some other we have not yet reach the result: work are in progress.

3.3 Photocurrent, I-V characteristic & X and γ-ray spectroscopy: experimental part

In the following we report on some experimental results we have obtained from two series of samples grown in our laboratory [44, 45] and starting to these we will try to create an overall speech. To complete the frame with the X and γ-ray spectroscopy, we refer also to [35, 46] (where I am co-author).

3.3.1 Introduction

As recently shown [20], the Boron Oxide Encapsulated Vertical Bridgman technique allows to obtain CZT crystals of great interest for X-ray spectroscopic detectors operating at room temperature. Indium doped semi-insulator CZT ingots have been grown with large single grains, resistivity values of the order of $10^{10}\Omega cm$, and very low dislocation density. The clearness and the homogeneity of this compound is still far from the degrees reached for other materials (Si, Ge) and the unwanted impurities, structural defects, and precipitates can introduce deep centers affecting the transport properties. Furthermore, the optimization of surface treatments, metalization processes, amplification and filtration systems for the output signal are still in progress [47–52]. The steady-state (DC) photocurrent (PC) technique gives interesting information about transport parameters as the mobility-lifetime product $\mu\tau$ and other terms related to the surface recombination [40, 53] and it plays a complementary role with respect to the high-energy photon spectroscopy. Due to the lower penetration depth, PC provides an evaluation of the surface quality of samples. The photocurrent spectral analysis adds chance to investigate the nature of bulk trap levels, surface centers, contact layer defectiveness, and the distribution of electric field in the sample volume.

3.3.2 Experimental apparatus and procedures

Photocurrent DC photo-conductivity measurements at room temperature were carried out on planar samples illuminated with photons in the range

$200 - 1600nm$.
The experimental PC apparatus is similar to that described in figures 3.3a and 3.3b and consists of a light source system ORIEL Mod. 66882 suitably screened and focused, with a Quartz Tungsten Halogen-250 W lamp ($\sim 1\mu W cm^{-2} nm^{-1}$ on the sample without neutral filter applied), neutral filters, a monochromator CornerStone 130TM 1/8 m Mod. 74000 covering the range $200 - 1600nm$ (wavelength resolution of $3nm$), a chopper Signal Recovery Mod. 197 operating at $220Hz$, a lock-in EG&G PARK Mod. 5209.
Voltage drop between 0 and $200V$ was applied to the sample by means of a Source Meter Keithley 2400 and the hot wire of bias is applied already on the illuminated face of the sample. The chopped monochromatic light was focused on a $3 \times 3mm^2$ area centered inside the metal contact, as well as the sample operates as in the high-energy detector configuration. Besides, the pair generation involves mainly a region of material where the electric field is almost uniform. The transparencies of Gold contacts ensures, in the energy range of interest, that an enough percentage of the incident radiation reaches the CZT surface. The output signal, collected as the voltage drop V_{out} on the load resistance R ($10k\Omega$) in figure 3.3b, is analyzed by the lock-in to reduce noise and remove the dark current contribution. The spectral distribution of the beam illuminating the sample was measured using an Hamamatsu Photonic MultiChannel Analyzer PMA-11 and a correction factor was introduced for all the measured spectra, taking into account the spectral distortion of Gold contacts measured for a reference Gold layer of the same thickness deposited on quartz. The mean photon flux on the active surface of CZT sample (i.e. below the metal contact) was estimated around $10^{11} photons/s$ for an incident flux of about $1\mu W cm^2$.
PC spectra have been acquired at fixed bias in the range $200 - 1600nm$ and the "illuminated"I-V curves have been measured at fixed wavelength of incident photons by means of a Source Meter Keithley 2400 (without lock-in amplifier). From this latter kind of curves, once we have subtracted the I-V dark characteristic (i.e. taken without lighting), a careful fitting with Many's equation [4]

$$I(V) = I_0 \frac{\mu\tau V}{L^2} \frac{\left[1 - \exp\left\{-\frac{L^2}{\mu\tau V}\right\}\right]}{1 + \frac{Ls}{\mu V}} \tag{3.22}$$

allows to evaluate the product mobility-lifetime $\mu\tau$ and the carrier surface recombination parameter s/μ (s is the surface recombination velocity) for electron and holes. In the equation 3.22 the thickness of sample L is required and the saturation current at high electric field I_0 is the third term gift from the fitting. The fitting procedure has been performed by least squares method with a dedicated tool of Matlab (fminuit). The experimental error for the current values is about 1% of the full-scale.
The obtained values of $\mu\tau$ have been compared with values by X-ray spectroscopy. The $22keV$ centroid as a function of bias for irradiation at the cathode side with ^{109}Cd source has been fitted with the simplified Hecht relation [3]. It is worth noting that in the equation 3.22 do not appear the incident radi-

ation wavelength, nevertheless different wavelength could give different results because of the unlike penetration length as we discuss later.

I-V Curves The I-V characteristics measurements have been taken with the above described photocurrent apparatus, obscuring the chamber that houses the sample. Recently, at the IMEM-CNR institute of Parma, it has been create a new system to achieve polarization up to $1000V$ to perform the I-V measurements at higher bias.
As just outlined in the previous sections, the I-V (dark) curves are useful, not only to get the background that must be taken away from the illuminated I-V, but because from these curves it is possible to achieve information about the detector and contact quality.

X and γ-ray spectroscopy The detector spectroscopic performances were evaluated by comparing the ^{241}Am, ^{109}Cd, and ^{57}Co spectra. The detectors were irradiated by a collimated photon beam impinging through the cathode and signals were readout by conventional spectroscopic NIM electronic chain. The employed charge sensitive preamplifier was the $CR110$, manufactured by CREMAT, Inc. A shaping time of $1\mu s$ was chosen for the main amplifier and the CZT samples were polarized with the same applied electric field using the high voltage power supply $CA12P$, manufactured by Emco. The data, filtered and shaped, are collected by a multichannel analyzer to get the source spectra. By mean the x-spectroscopy is also possible to obtain the $\mu\tau$ product value. Irradiating the detectors with the $22keV$ line of ^{109}Cd source from the cathode side and collecting the energy spectra at different bias voltages, we can extract this value by fitting the photo-peak centroids at $22keV$, as a function of the bias applied, with the simplified Hecht relation [3]. Indeed, because of the tiny penetration length of the $22keV$ radiation, we can considerate that the transport is due to only one kind of carrier, so we can use the simplified Hecht relation to fit the data.

3.3.3 Samples

The first series of samples analyzed in **??** have thickness between 1.2 and $1.8mm$ and area of about $5 \times 5mm^2$ and they were cut from 1-inch CdZnTe crystal grown from $7N$ (type A) and from $6N$ (type B) precursors. The second series of samples studied in **??**, instead, have thickness of about $1.2mm$, section of about $6 \times 6mm^2$ and they were cut from 2-inch CdZnTe crystals grown from $7N$ precursors. Both the two groups of samples have been grown by Boron Oxide Encapsulated Vertical Bridgman [54, 55], with a growth rate of about $1mm/h$ and a thermal gradient of $10°C/cm$. The crystals were grown with a Zinc concentration of 10% and Indium doping ($10^{17} - 10^{18}cm^{-3}$) achieving high resistivity around $10^{10}\Omega cm$, as measured by current-voltage (I-V) characteristics as reported in [18, 35]. The dislocation density evaluated after Nakagawa etching [56] on the surface perpendicular to the (111) plane is typically lower

than $10^4 cm^{-2}$. Impurities have been analyzed by Glow Discharge Mass Spectroscopy: the larger concentration impurity, lower than $1ppm$, is due to the Boron from encapsulant. The samples were mechanically polished with abrasive paper and $0.05\mu m$ alumina suspension, rinsed in methanol, and chemically etched and passivated with a two-step chemical process [57] before the metal contact deposition. The two-step treatment minimizes the surface currents and it consists of a 2% bromine in methanol etching solution for three minutes followed by a mixed solution of 2% bromine in methanol, 20% lactic acid and ethylene glycol for two minutes. After each etching, the samples were rinsed in methanol. The surface oxidation was carried out with a NH_4F/H_2O_2 solution for six minutes at room temperature, ensuring the formation of a layer of about $70nm$ as shown by ellipsometric measurements. After evaporation of $750\mathring{A}$ thick semitransparent Gold contacts (of about $2.5 \times 2.5mm^2$ area for the first group and $5 \times 5mm^2$ for the second group) on the opposite surfaces of sample, a thermal treatment at $80°C$ for 70 hours in N_2 atmosphere was carried out.

3.3.4 First series of samples

We discuss some results, part of which has been presented to the *SPIE conference 26-30 August 2007 S. Diego (CA)*

3.3.4.1 Material characterization

Electrical properties Concerning the first series Ingots with different content of In-dopant and from precursors of different quality (type A and B) are electrically investigated. Current-voltage (I-V) measurements was carried out and some representative results are shown in figure 3.4. It is immediately clear as the I-V behavior is tightly related to the material quality (see table 3.1). As reported by Johnson et al. [58], three I-V curve types, with regard to low voltage behavior, can be identified in CdTe/CZT detectors:

1. Increasing resistance shape (type I).
2. Linear resistance shape (type R).
3. Decreasing resistance shape (type D).

Further, worse detector performance was found moving from I-type to D-type curves. As summarized in Table 3.1, samples of group A are I-type detector (Fig. 3.4, left), on the other hand samples from low-quality CZT show worst and uncertain electrical properties with different electrical trends (Fig. 3.4, right), although the high resistivity values indicate a good compensation level. The ohmicity factor of ingot 6, calculated at voltages higher than $25V$, varies between 0.87 and 0.93 (1.00 is the ideal value). Resistivity and dark current I_{dark} seem instead depend on the In content. As reported in Table 3.1, our preliminary analysis suggests opposite trends for resistivity ρ and I_{dark} (at 100V) decreasing and increasing, respectively, on increasing In content above about

$Ingot$	$kind$	$Indium$ (cm^{-3})	ρ (Ωcm)	$I_{dark}(nA)$ @100V	$I-V$ $type$
5	A	2.30×10^{17}	$(1.0 \pm 0.3) \times 10^{10}$	3.5	I sym.
6	A	4.50×10^{17}	$(1.7 \pm 0.4) \times 10^{10}$	2.5	I sym.
8	A	8.50×10^{17}	$(4.0 \pm 1.0) \times 10^{10}$	3.0	I sym.
11	B	2.40×10^{18}	$(6.0 \pm 1.2) \times 10^{9}$	62.8	I,R sym.
14	B	1.01×10^{18}	$(8.0 \pm 2.0) \times 10^{9}$	17.5	D asym.
15	B	6.08×10^{17}	$(1.3 \pm 0.3) \times 10^{10}$	5.0	D asym.

Table 3.1: Electrical features of samples from several CZT ingots. [44]

$6 \times 10^{17} cm^{-3}$. The resistivity values calculated from I-V slopes at high voltages and bulk conductivity limited range [18] give similar results.
Due to the non-uniformity of chemical properties for samples coming from sides at different distances from the growth axis and from crystal regions solidified in different times (due to the In enrichment of melt during the progress of growth, the material last solidified contains the greater amount of In), the values of ρ and I_{dark} were averaged out on more samples of the same ingot. The low number of samples does not allow to identify with confidence the trend of electrical properties along the growth axis, but we believe the position in the ingot giving better results is determined by the nominal In content in the melt. From data of Table 3.1, it can suppose the existence of an ideal In concentration ranging between $2 - 8 \times 10^{17} atoms/cm^3$ leading to better dark current values and I-V behaviors. To better understand the microscopic origin of the I-V curves, the photo-conductivity analysis on the same samples was performed.

Optical characterization The photo-voltage spectra for representative samples from high quality and low quality ingots are shown in Fig. 3.5 for positive and negative bias ($\pm 200V$) at the same incoming photon flux. Left plot show as for high quality material only a sharp peak related to pair generation at the band-gap was detected. This peak shifts towards higher wavelengths with monotonic behavior (not shown here) on varying bias to more negative values, due likely to the different charge collection as a function of the maximum absorption depth and bias. For this reason, in addition to the non uniformity of sample, a carefully band-gap evaluation is not possible from these measurements. The relative intensity of two spectra has to be lead to the different path length of photo-generated carriers, suggesting that the dominant collection at positive/negative voltages is ascribable to electron/hole collection. Hole signal is significantly lower due to the lower mobility of positive charge carriers. Only a weak wide shoulder at energies above the band-gap was detected.
In the right side of Fig. 3.5, the more complex spectra for low quality samples are reported. If the negative bias spectrum is substantially unchanged as regards of the previous plot, at positive bias a strong contribution at energies above the band-gap (named S-band) and also below the band-gap between $1100 - 1600 nm$

(D wide band in the plot) was found. The S-band could be attributed to surface levels near the contacts (wide background) and/or to Zn-enriched layers near the illuminating side of sample (peaks at about 500 and $600nm$). On the other hand, the wide D-band is attributed, even in the light of the following remarks, to deep traps in the bulk [59]. Similar results were obtained by illuminating the other face of each sample, with a surface contribution only for positive bias suggesting the photo-voltage signal originates likely from traps for negative charge carriers. To stress the contribution to the photo-conductivity from regions at different depths, qualitative measurements at fixed bias ($+200V$) on varying the photon flux were carried out. A detailed analysis requires a better knowledge of the composition and depth of surface layers and, if necessary, to take into account non-linear effects.
In Fig. 3.6 the semilogarithmic plot of the photo-voltage spectra for a sample showing a significant S-band are shown. The minimum photon flux is labeled as "$\times 1$"and others curves refer to n-times the minimum photon flux. It is clear that increasing the photon flux the G intensity is enhanced more than S-band, but the profile in the range $750 - 850nm$ experiences at least two contributions. Assuming a photon flux-independent absorption cross section, as reasonable for our low optical densities, we believe that at low photon flux the effects of absorption at the illuminated surface are dominant (S-band), but increasing flux more and more deep regions are involved then bulk and eventually the non-illuminated surface contribute to the photo-voltage. At high photon flux (see for example curve $\times 1$), the G-peak shifts to lower wavelength (about $790nm$) as effect of an increasing peak at about $835nm$ probably due to the presence of Zn-poor layer near the cathode surface. At about $920nm$ a weak peak was observed, ascribable to the well known A-center [60, 61]. The normalized photo-voltage ratios between the G-peak and S-band (G/S), D-band (G/D), and A-center (G/A center) are reported in Fig. 3.7. Contributions from each term was calculated as the area underneath the Gaussian deconvolving the spectra of Fig. 3.5. It is evident as the D-band and the A-center follow strictly the energy-gap, whereas the S-band relative contribution decreases on increasing photon flux according to the previous interpretation of its origin.

3.3.4.2 Spectral response and charge collection efficiency

Samples are then submitted to X-ray irradiation by several sources (^{109}Cd, ^{241}Am, ^{57}Co) to check their spectroscopic features in a wide range of energies. Results reported in Table 3.2 show as only the crystals obtained from A-type ingots present spectroscopic capabilities. A measurement of $\mu\tau$ product was carried out in order to characterize the charge transport properties of the samples. Detectors were irradiated by $22keV$ line of ^{109}Cd source from the cathode side and energy spectra were recorded at different bias voltages. The photo-peak centroids at $22keV$ as a function of bias are plotted in Fig. 3.8 and are fitted with the simplified Hecht relation [62, 63]. The obtained value of $\mu\tau_e$ is about $0.75 \times 10^{-3} cm^2/V$.
Spectra of ^{109}Cd and ^{241}Am, acquired with two different detectors from A-type

$Ingot$	$kind$	^{109}Cd	^{241}Am	^{57}Co	$\mu\tau$
5	A	X	X		
6	A	X	X	X	X
8	A	X	X		X
11, 14, 15	B				

Table 3.2: Spectroscopic features of samples from several CZT ingots. [44]

ingots biased at $300V$ and $120V$, are reported in Fig. 3.9. The unresolved set of lines around $17keV$ of ^{237}Np (Fig. 3.9b) presents a typical FWHM (Full Width at Half Maximum) value of $\sim 7.2keV$, while we find a FWHM of $\sim 9keV$ at $\sim 60keV$. The threshold value is $9.5keV$. The resolution at low energy is comparable to performance obtained with standard commercial detector [63] while the one obtained at higher energy (the average interaction is more far from the cathode) is much worst. This confirms that these samples still suffer from charge transport deficit.

3.3.4.3 Discussion and conclusions

High resistivity ($10^9 - 10^{10}\Omega cm$) and low etch pit density CZT crystals were grown by vertical Bridgman method with a fully encapsulation by a boron oxide layer.
Better I-V curves are shown by samples from high quality precursor material. On the other hand, low quality samples, although high resistivity values, are characterized by higher leakage currents even after passivation (data not shown here), their photo-voltage spectra suffer a large contribution from surface traps, and no spectroscopic features were found. Glow discharge spectroscopy on polycrystalline precursor gave a higher concentration of carbon and oxygen in the low quality material, then the different surface properties could be attributed to the action of these elements during the steps of preparation of the device. The absolute values of photo-voltage indicate a higher charge production efficiency in the A-type material due to very low surface trapping, leading to significant values of the $\mu\tau$ product ($2 \times 10^{-4} cm^2/V$) and to spectroscopic features.
Moreover, the mobility-lifetime product of $0.75 \times 10^{-3} cm^2/V$ for electron transport was determined by X-ray irradiation. As expected [53], this value differs from the value obtained from photo-conductivity because in this second case the surface effects affect significantly the measure. Even if the transport properties of the material are not yet optimal, spectroscopic characteristics are demonstrated.
By the comparison between crystals with different In content in the melt, it can suppose the existence of an ideal In concentration ranging between $2 - 8 \times 10^{17} atoms/cm^3$ leading to better dark current values and I-V behavior, even if in the solid the In profile varies along the growth axis in a not simply predictable way.

As a final remark, samples from high quality ingots of Table 3.1 subjected to standard passivation surface treatments, despite leakage currents lower of a few unit than the non-passivated samples, exhibit similar spectroscopic properties.

3.3.5 Second series of samples

Part of the results we report here has been presented at the *2008 Nuclear Science Symposium, Medical Imaging Conference and* 16^{th} *Room Temperature Semiconductor Detector Workshop 19 - 25 October 2008 Dresden, Germany* [45].

3.3.5.1 Results

Spectral features PC spectra acquired for $V = \pm 200V$ are shown in Fig. 3.10. The investigated energy interval can be divided in three regions:

I a high energy region $(200 - 700nm)$ in which it can be found the contributions from surface oxides.

II the CZT band-edge region around $800nm$.

III a low energy region $(900 - 1600nm)$ characterized by shallow and deep levels of CZT or other unwanted complexes.

The comparison between spectra at negative and positive biases for the same sample highlights different charge collection mechanisms. The low penetration depth of photons in the region II yields pairs of carriers mainly near the illuminated surface. According to the R-S theorem, holes and electrons contribute to the photocurrent with weights proportional to the length of path covered in the device. For negative bias applied to the illuminated surface, as in figure 3.3a, the photocurrent is mainly due to the electron drift towards the anode contact. On the other hand, for positive bias the contribution is mainly due to the holes. The higher mobility of electrons justifies higher photocurrent signals for negative voltage, when the spectrum is characterized by an absolute maximum at $786nm$, due to the band-edge transition as confirmed by absorbance measurements (solid line labeled ABS in Fig. 3.10); in the region III a wide and weak contribution above $1000nm$ was evidenced, ascribable to a large sort of impurities responsible for deep centers, as predicted by the theory of the compensation [42]. The region I shows, instead, an overlapping between a strong wide band and some localized transitions, whose nature has been investigated.

In figure 3.11 are reported the PC spectra for negative bias using neutral filters with optical density $OD = 0.5$ and 2.0 to reduce the photon flux from the lamp. In figure 3.10 no filters were used.

The spectra in figure 3.6 were normalized to their absolute maximum for comparison: it is evident as the signal in the region I becomes dominant on decreasing photon flux (i.e. for higher OD values).

The authors have noted that the ratio between the intensities in the region I with respect the region II is not constant. In particular increasing the incident flux intensity the band-edge peak increases the size with respect to the

peaks in the region I, otherwise it happens with respect the region III, where the ratio is almost independent on the photon flux. This result suggests that the photocurrent for both the regions II and III originates from the bulk of device. The PC in the region I (above the band-edge) instead seems to have not origin from high-energy sub-bands transitions of bulk but, on the contrary, the saturation effect with increasing the number of incident photons, suggests that the pair generation could be related to surface levels created likely as effect of the preparation processes. A further confirmation comes from measurements in the plane transversal field PTF (Planar Transverse Field) configuration (in this configuration the light hits the sample along its border, not on the surface of the electrodes) shown in figure 3.12, in which the illumination is far from the contacts and the photocurrent in the region I results significant again. This result excludes effects due to the metal contacts and indicates the passivated surface of sample as origin of this contribution to the PC.
As a final remark, the samples from different ingots and different slices of the same ingot show similar behaviors for incident energies below the energy-gap. On the other hand, in the region I the spectra are characterized by a large variety of intensity values, even if the representative structure of curves is almost unvaried, as a confirmation of the variability in the surface quality with respect to the bulk properties.
Data from photoluminescence reported in literature could ascribe the peaks in the region I to oxides of Cd and Te [65–67], formed near the surfaces during the etching and passivation processes. Finally, the spectrum at positive bias was analyzed in the light of recent works. As evidenced in figure 3.13, the spectrum for positive biases shows an intense maximum at about $810nm$ and only wide broad bands in the regions below and above the band-edge. The absolute maximum of PC experiences an abrupt shift towards higher wavelengths of about $25nm$ near the zero of the applied bias. The shift happens for a low negative voltage likely due to a crystalline internal field that screens the external electric field.
The displacement could be due to the combined action of both low hole $\mu\tau$ product and penetration length of the light. The position of the PC maximum is fixed by the convolution of transmittance curve and electron-hole pair generation rate. At positive bias and at photon wavelengths lower than the band edge ($786nm$) the transport is mainly due to the holes, generated close to the illuminated surface. Because of the lower transport properties, the holes, flying across the sample, experience a strong trapping, breed spatial charge and polarize the sample shielding the applied field chiefly near the cathode. As a consequence, only a lower carrier fraction can be collected from the cathode and the photo-induced current is then very low. A better current signal is obtained at higher photon wavelengths, when a significant fraction of holes generated deeper in the sample reaches the cathode contact, giving a lower space charge. Consequently, when the photocurrent is related to the hole motion, we have a bigger signal at greater wavelength when the penetration length increases and the polarization decreases, so the maximum shifts at higher wavelength.
It is important to note that there is another possible interpretation of this shift.

Indeed also the theory explained by Franc et al. [11, 12] can be appropriate to describe this phenomenon. This sharp displacement, according to this theory, could be justified by a shift of the gap transition on varying the bias due to the space charge accumulated on deep levels, as reported with regard the CdTe [11, 12]. Moreover we cannot exclude effects related to the presence of traps with very high capture times involved in the transport of carriers. Works are in progress to highlight this topic by studying samples in different geometric configuration with respect to the incident light.

Photocurrent at fixed wavelength Bulk transport and surface properties were investigated on varying bias at fixed wavelength and fitting the photostimulated I-V curves with Many's relation reported in equation 3.22. The hypotheses of this model are:

1. The electric field and the transport properties are constant in the detector volume. This hypothesis, due to the Gauss law, involves the absence of spatial charge in the crystal.

2. The material properties are not modified by the applied electric field.

3. Many's relation was obtained for blocking contacts. In our case this requirement is satisfied as verified by the I-V curves [35] showing an increasing resistance type behavior [58]. To not perturb too much the system and to prevent the generation of spatial charge it is very important that the measured photocurrent is of the same order of the dark current or lower.

4. The light absorption must take place very close to the illuminated electrode of the detector.

The first three hypotheses are reasonably verified in our case once the space charge creation is prevented maintaining a low photon flux. As a consequence of the fourth requirement, the wavelength of the incident photons is important. As confirmed by the fitting of a large number of curves, the optimal wavelength is near the band-edge. In this case we obtained a good signal level and a higher absorption coefficient that limit the penetration length of the light in the material. The experimental data for incident photons at $786nm$ for negative (stars) and positive (circles) applied bias are shown in figure 3.14. The curve for holes refer to the use of a neutral filter with $O.D = 1.5$, the other ones have been acquired without filters. Values for $\mu\tau$ product and surface recombination s/μ for electrons and holes are obtained as parameters of fitting for negative and positive biases, respectively, and reported in Table 3.3. As comparison values obtained on the same sample from X-ray spectroscopy by the $22keV$ line of the ^{109}Cd source are also reported. The comparison evidences a weak agreement due to the different excitation processes. In the PC measurements the surface effects can be very important and they can justify the lower value of $\mu\tau$. For incident light at $700nm$ (region I) the fitting worsens and the term of surface recombination s/μ increases with respect to the other curves as expected, as a

$Car.$	$Rad.$	$O.D.$	$Flux$ $[1/s]$	$\mu\tau$ $[cm^2/V]$	s/μ $[V/cm]$
e	786 nm	0.0	$\sim 3 \cdot 10^{12}$	$(1.3 \pm 0.2)10^{-3}$	$(3.3 \pm 0.2)10^{2}$
e	786 nm	1.5	$\sim 1 \cdot 10^{11}$	$(1.45 \pm 0.2)10^{-3}$	$(6.3 \pm 0.4)10^{2}$
e	700 nm	0.0	$\sim 3 \cdot 10^{12}$	$(1.0 \pm 0.2)10^{-3}$	$(4.9 \pm 0.6)10^{3}$
e	22 keV	-	$\sim 3 \cdot 10^{2}$	$(1.9 \pm 0.3)10^{-3}$	-
h	786 nm	1.5	$\sim 1 \cdot 10^{11}$	$(4.6 \pm 0.3)10^{-5}$	$\sim (1 \pm 1)10^{-2}$
e	786 nm	2.0	$\sim 3 \cdot 10^{10}$	$(5.0 \pm 0.1)10^{-5}$	$\sim 0.9 \pm 0.9$

Table 3.3: Transport parameters ($\mu\tau$ and s/μ) for electron e and hole h obtained from photocurrent at different wavelength and X-ray spectroscopy. [45]

consequence of the reduced radiation penetration length.
A discussion about the effects of different photon fluxes on the result of fitting is due. A good agreement until a 30 times reduction of the maximum flux (neutral filter with $O.D. = 1.5$ was found for the $\mu\tau$ product for electrons, while an increase of the ratio s/μ was observed probably due to the significant queue of the surface contribution (region I) overlapping the band edge (as it is possible to see for example in figure 3.11). On the contrary, for holes we obtained good fits only at very low fluxes (i.e. with $O.D. = 1.5$ and 2.0 filters) even if the results are characterized by lower precision. Due to the lower transport properties of holes, lower fluxes are necessary to prevent the space charge formation. The data reported in Table 3.3 for PC measurements show as the surface recombination parameter s/μ for holes collapses. This could be due to the different mobility of electrons and holes. In fact at positive bias (with respect to the illuminated electrode) due to their higher mobility the electrons are extracted quickly from the generation zone to be collected at the corresponding electrode and the recombination phenomena are infrequent. Because of the hole lower mobility at negative bias we have an higher concentration of holes in the generation zone and then a major recombination. Besides another possible phenomenon explanation could be the presence, in the region under the contacts, of traps dealing with electrons, that could arise at higher recombination rate when the charge on the electrodes is inducted by the electron motion. Indeed, in this second case, the hole moving to their collecting electrode can recombine with the electrons. It is noteworthy that the photocurrent techniques allows to evaluate the transport properties of holes, in addition to the surface features, while the X spectroscopy signal from these carriers is too low to be fitted. A latest consideration is due. When a photon flux hits on the electrode surface it can be not excluded that carrier generation modify in an appreciable manner the free carrier density in the crystal. As a consequence the free carrier photo-generation could give a different bulk carrier density and than some variation in the $\mu\tau$ product value can be justified, as reported in [68]. Indeed τ is independent of the carrier density only when the generated carrier density is significantly lower than the equilibrium free carrier density. The authors think that this is one of the reasons of the

discrepancies between the different $\mu\tau$ values obtained with different wavelength and with the X-ray. However (especially when the transport is mainly due to the electrons) the little change in the $\mu\tau$ product value on varying the photon flux intensity, supports the idea of a reduced presence of space charge and this reasonably allows to assert that carrier injection is negligible and, above all, charge generation are not dramatic. For these reasons we believe that Many's relation can be successfully used to fit the experimental curves. In relation to the different value of $\mu\tau$ obtained at $700nm$ and $786nm$ at the same flux intensity, we only note that the penetration length at $700nm$ is smaller than the $786nm$ one. For this reason the generation rate (number of carrier per second per volume unity), just below the contact, is quite different. In the first case the whole radiation flux is absorbed in the the first surface layers, so the generation rate could modify the band curvature near the contacts and then modify the illuminated I-V profile; increasing the wavelength this phenomenon should be attenuated.
Moreover the error associated with the fit parameter quantifies the uncertainty in the calculation of this parameter starting from a specific data set and should not be confused with the standard deviation of this parameters on a large number of data fitted. Normally these two values do not coincide and, also because of the correlations between the parameters, this last one is greater than the first one.

3.3.5.2 Comparison with X and γ Spectroscopy

As reported in Table 3.3 the photocurrent measurements have been compared with the X and γ-ray results published in [35, 46]. Detectors were irradiated with a ^{109}Cd source and the centroid of the photo-peak relative to the $22keV$ line was determined as a function of a positive bias voltage. The obtained values 3.15 were then fitted by the simplified Hecht equation leaving the mobility-lifetime product as a free parameter. A value of $1.9 \times 10^{-3} cm^2 V^{-1}$ was found. The procedure was also repeated for negative bias, in order to determine also the mobility-lifetime product for holes, but the measurement resulted too noisy. below in figures 3.16 (a) and (b) are reported the spectra of ^{109}Cd and ^{241}Am sources.

3.3.5.3 Conclusions

A large surface contribution to the photocurrent signal has been evidenced and attributed to oxides of Cd and Te in the surface layers created by etching and passivation processes. The metal evaporation does not seem to introduce surface defectiveness and the contact quality was verified even with different illumination geometries. In spite of the presence of a large number of surface defects related to oxides of Cd and Te formed during etching and passivation, the samples show good transport properties, and spectroscopic features of the bulk material. For these reasons they result very promising for applications for X and Gamma-ray detectors. Transport properties of suitable planar de-

tectors based on CdZnTe have been measured and the results from different experimental techniques have been compared. The steady-state photocurrent technique allowed to evidence the presence of deep levels, as predicted by the compensation theory, and surface states highly involved in the charge collection. By varying the bias, at fixed wavelength of the incident photons, the transport parameters as the mobility-lifetime product $\mu\tau$ and the surface recombination parameter s/μ for electrons and holes were obtained by fitting with Many's relation. The values of $\mu\tau$ for electrons from PC are close to the results from X-ray measurements; the discrepancies were attributed to the surface effects with a cue overlapped to the band gap region evidenced in the photocurrent signal and attributed to oxides of Cd and Te of the surface layer created by etching and passivation processes. The metal evaporation does not seem to introduce surface defectiveness and the contact quality was verified as well using different illumination geometries. The material has good transport properties, in spite of the presence of the large number of surface defects, and show good spectroscopic features. For these reasons they result promising for applications for X and Gamma-ray detectors.
Finally, in the last time, we have made photocurrent measurements on detectors produced at the Madrid University by "Laboratorio de Crecimiento de Cristales, Dpto. Fısica de Materiales, Facultad de Ciencias, University Autonoma de Madrid, Spain". At the beginning, these detectors did not show any band above the gap. Later, after we have removed the contacts, re-passivated the samples and re-evaporated the contacts, we have performed new photocurrent measurements and we have shown up the superficial band. This is a further confirm that responsible for the S-band are the surface treatments.

3.4 Final remarks and perspectives

Further studies must be performed to improve the detector quality, but some fixed point has been achieved and the work is in progress:

- The material achieves high resistivity values and shows good structural quality and transport properties (mainly for the electrons). The as-grown material quality and then the detector spectroscopic properties have been improved.
- we have demonstrated that the S-band and probably the reduced spectroscopic quality (in comparison with the transport properties) are due to the surface treatments before the contacts deposition.
- The shift in the gap-peak when we change the bias polarity is due to the lower transport properties in the hole case (with respect to the electron case) and it is related to the radiation penetration length and to the mean free path of the holes.
- The discrepancies between the $\mu\tau$ value obtained from the X spectroscopy and from the photocurrent measurements may be due to polarization ef-

fects and, to investigate this hypothesis, we are developing some modified model to better describe the steady photocurrent behavior.

- To study the transport parameters and the trapping mechanisms, we are implementing a new system to carry out pulsed photocurrent and to study the time dependence of the photocurrent impulse. The pulsed source is a He-Ne laser that allow to get wavelength emission of 266, 355, 568 and $1064nm$, and the output current pulse is digitalized by a 2GS/s digitizer.
- Further development, as the temperature controlled photocurrents, are in progress.

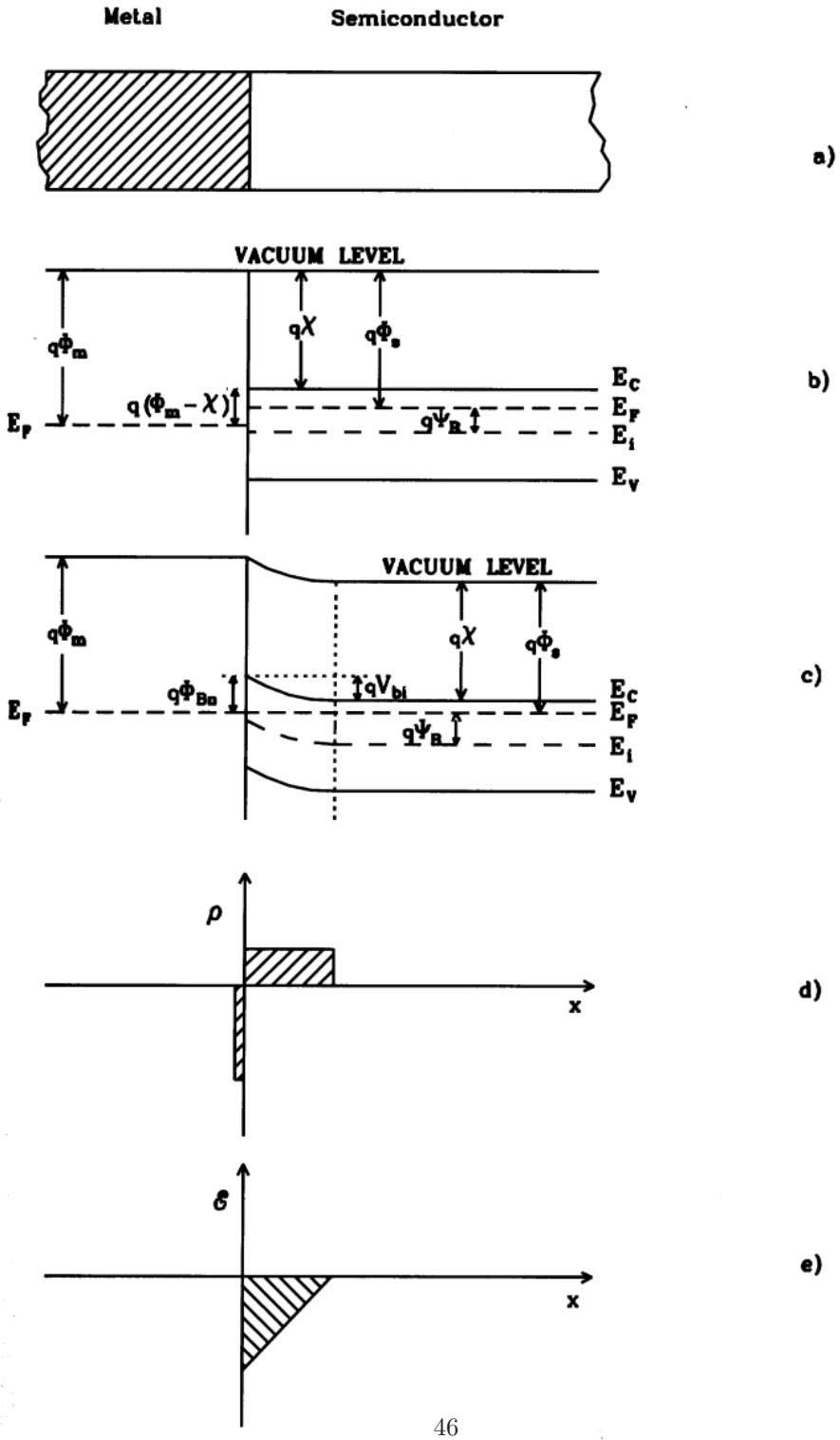

Figure 3.1: Metal Semiconductor contact (a); Description in the band model: metal and n-type semiconductor separately in thermal equilibrium (b); metal and semiconductor joined together (c); charge density (d); electric field (e).[31]

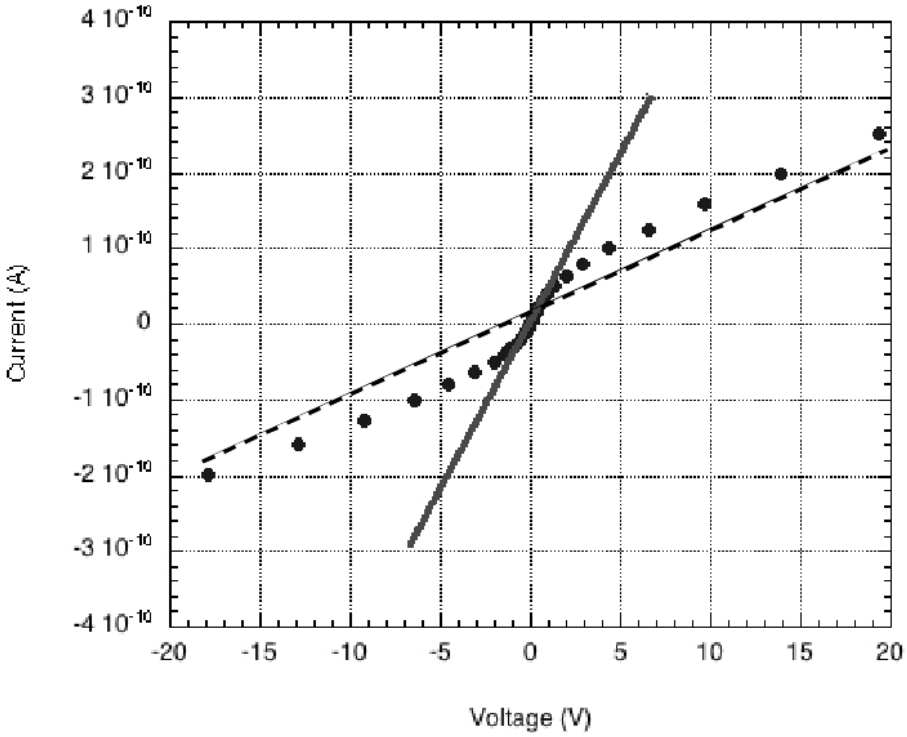

Figure 3.2: Low voltage I–V curve of a CdZnTe sample after passivation and provided with guard ring. The straight line represents the real bulk resistance, while the dashed line the erroneous resistance obtained at high bias [35]

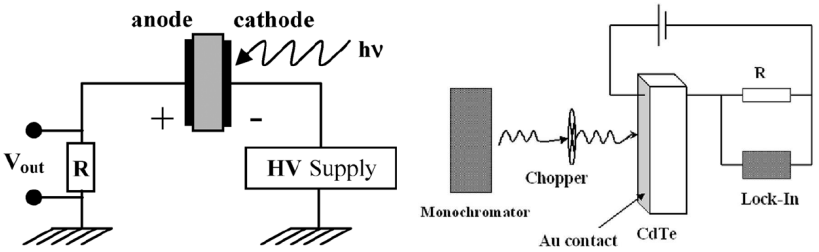

(a) Experimental setup (negative bias applied)

(b) Sample illumination geometry[41]

Figure 3.3

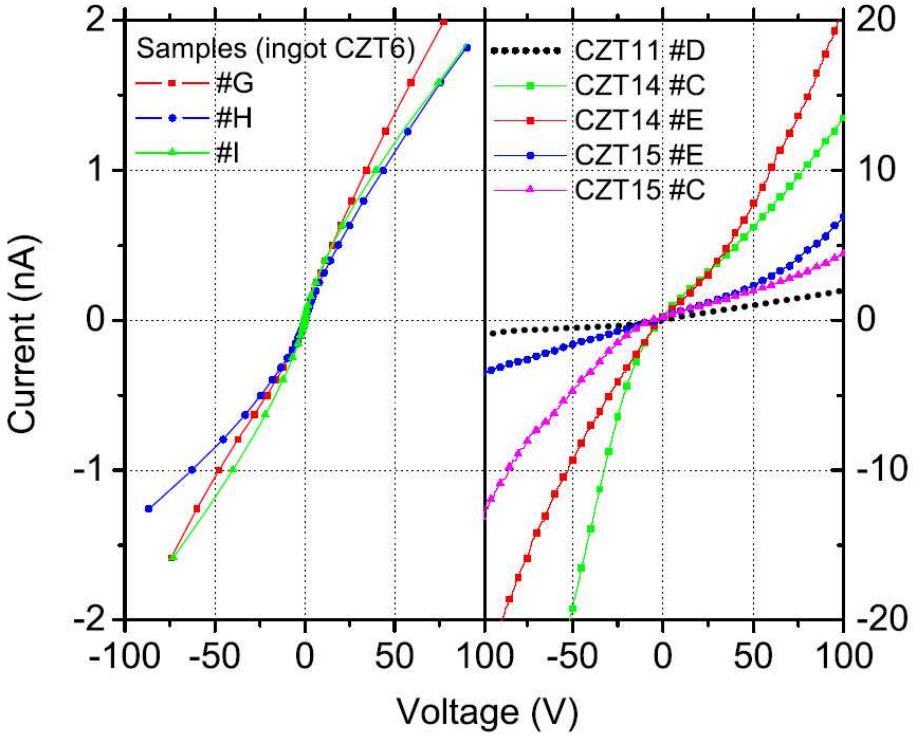

Figure 3.4: I-V curves for samples from ingot 6 (left) and ingots 11, 14, 15 (right) [44]

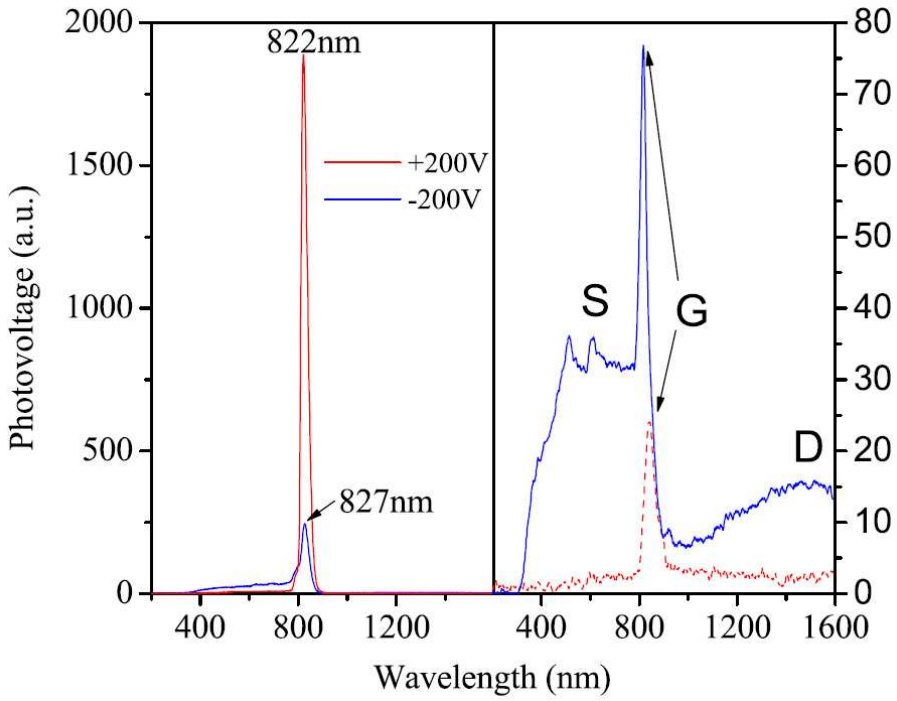

Figure 3.5: Photoconductivity spectra for high quality A (left) and low quality B (right) ingot samples. In right picture labels refer to energy-gap (G), deep traps (D), and above gap (S) contributions. [44]

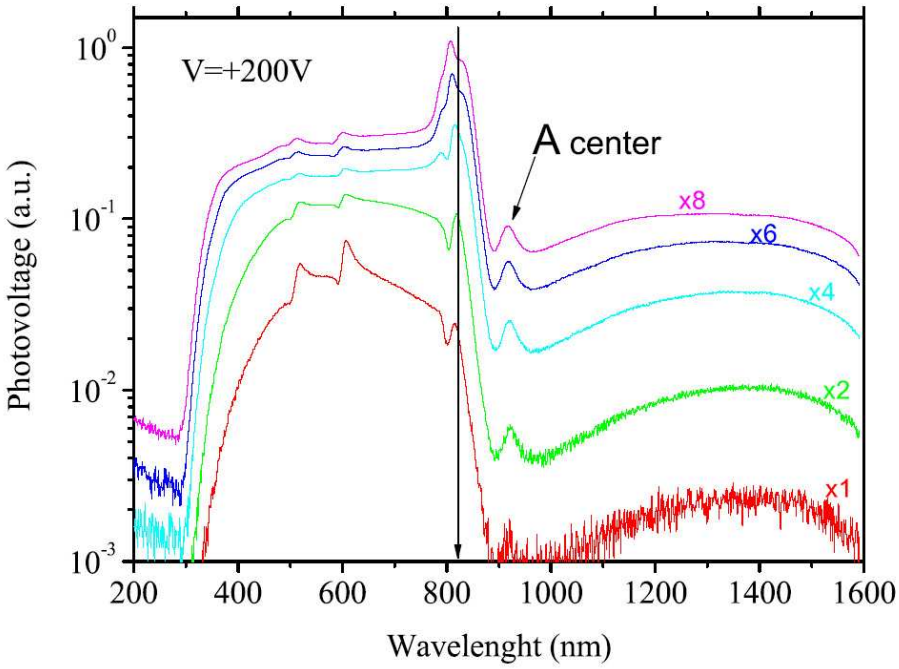

Figure 3.6: Semilogarithmic plot of the photovoltage spectra on varying the incoming photon flux. The minimum photon flux is labeled as $\times 1$. [44]

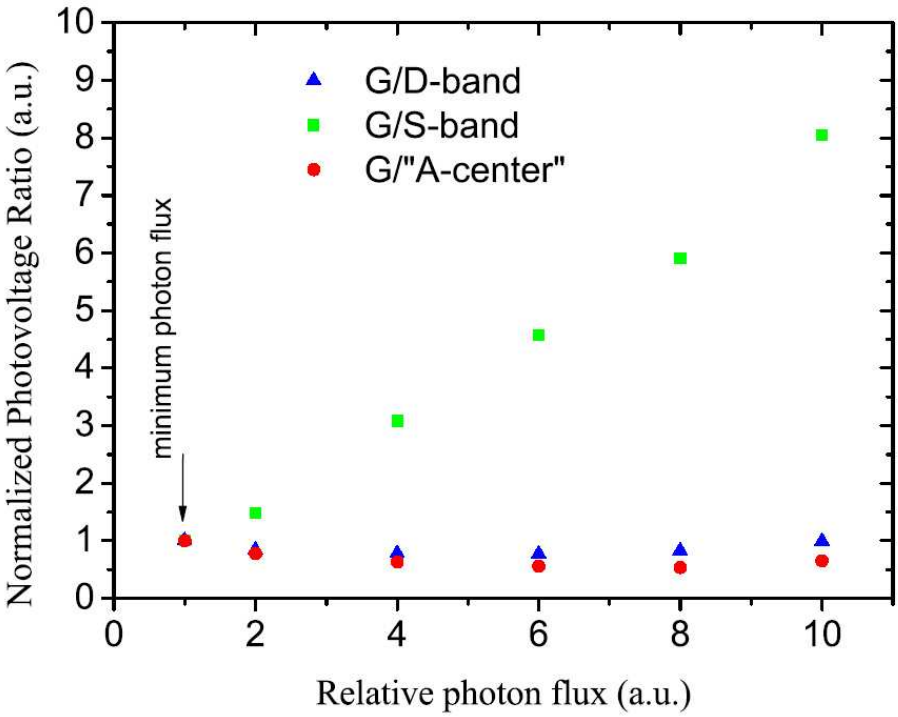

Figure 3.7: Normalized photovoltage ratio as a function of the photon flux: G/D-band (up-triangle); G/S-band (square); G/A-center (circle). [44]

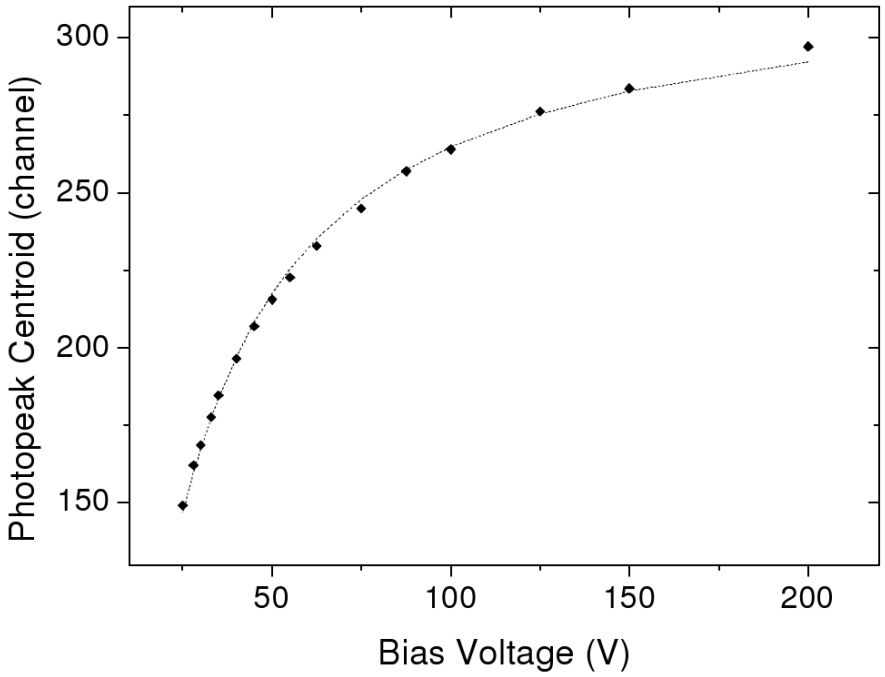

Figure 3.8: Charge collection efficiency as a function of applied voltage for the $22keV$ photopeak of ^{109}Cd. The solid line is the best fit with the Hecht equation. [44]

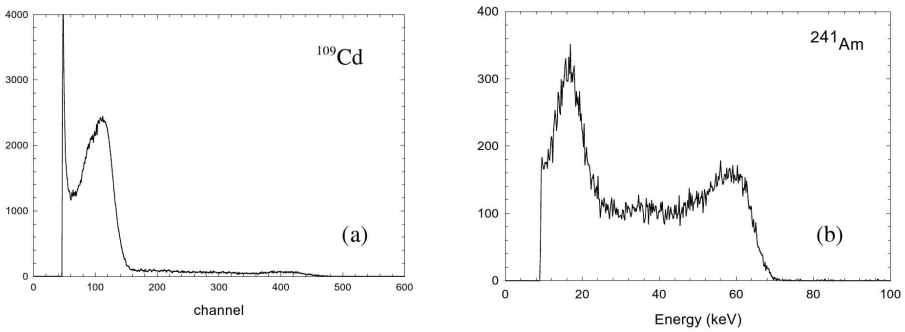

Figure 3.9: (a): Energy spectrum acquired irradiating a CZT sample transversally to the electric field direction with a radioactive source of ^{109}Cd. (b): Energy spectrum obtained irradiating the device across the cathode with a radioactive source of ^{241}Am. [44]

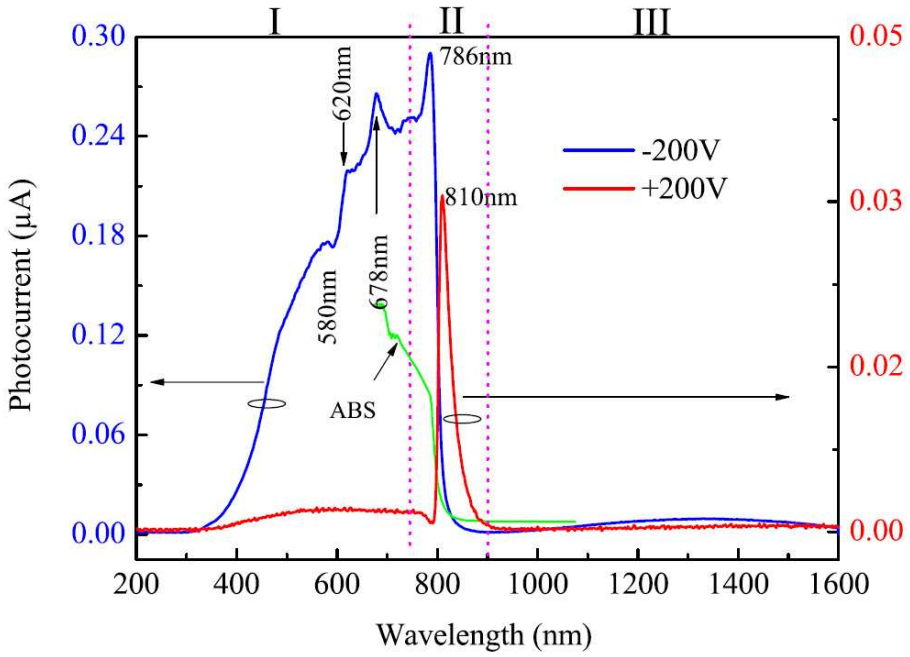

Figure 3.10: PC spectra for V = 200 V (solid line) and V = +200 V (dashed line). The curve labeled with ABS is the absorption edge of sample reported in arbitrary units for comparison. [45]

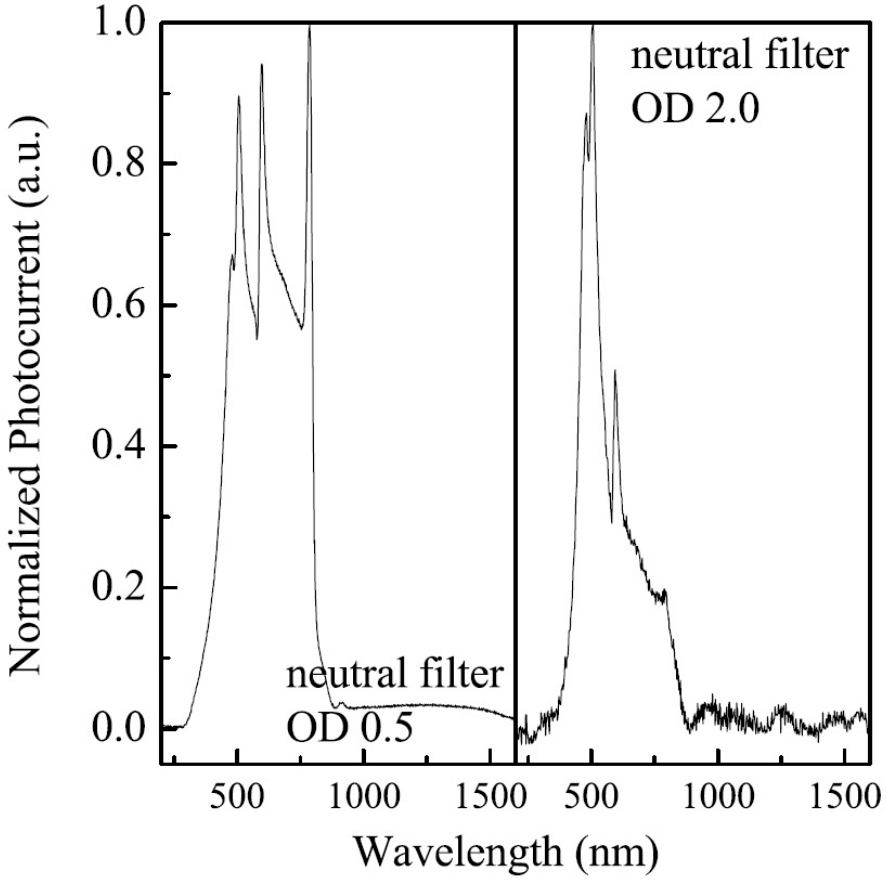

Figure 3.11: PC spectra for different photon fluxes at V = 200 V . Left side: neutral filter with $OD = 0.5$; right side: neutral filter with $OD = 2 : 0$. The curves are normalized to their absolute maxima. [45]

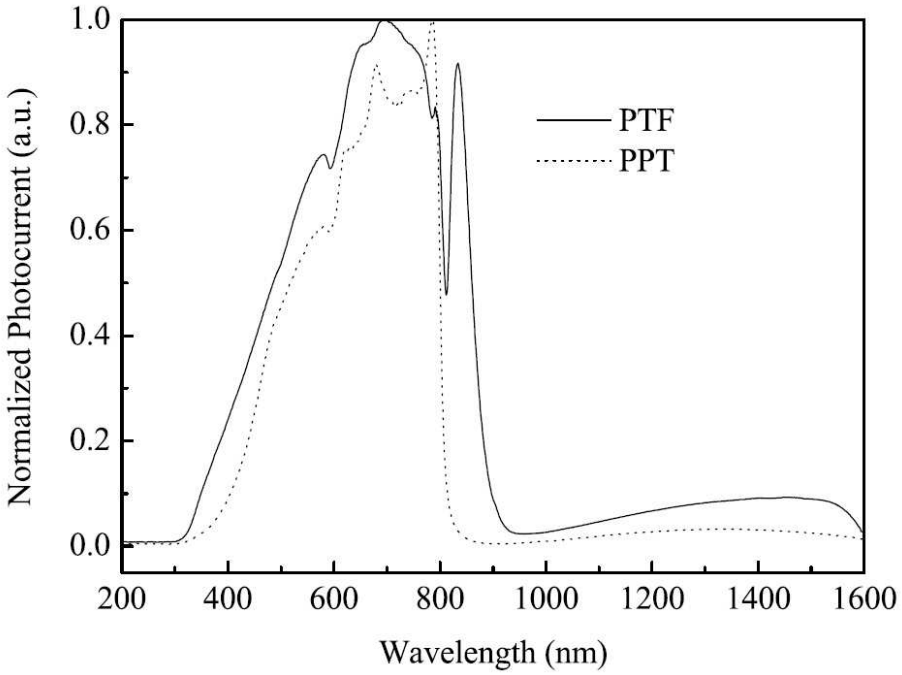

Figure 3.12: Comparison between PC spectra for illumination on the metal contact (Planar Parallel Field: PPF configuration) and along the thickness of sample (PTF configuration). The spectra were normalized to their maxima. [45]

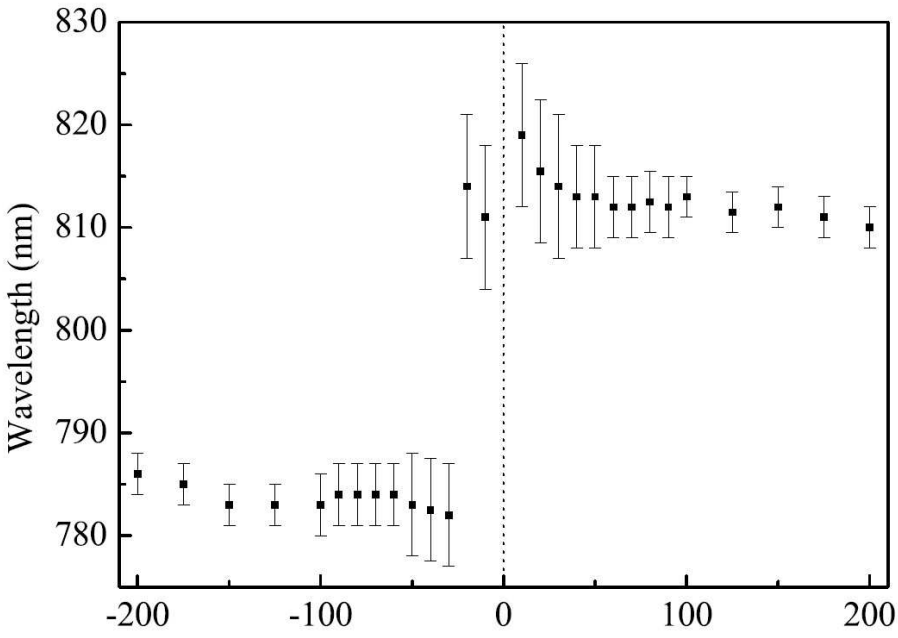

Figure 3.13: Shift of the band-edge maximum as a function of the applied voltage. [45]

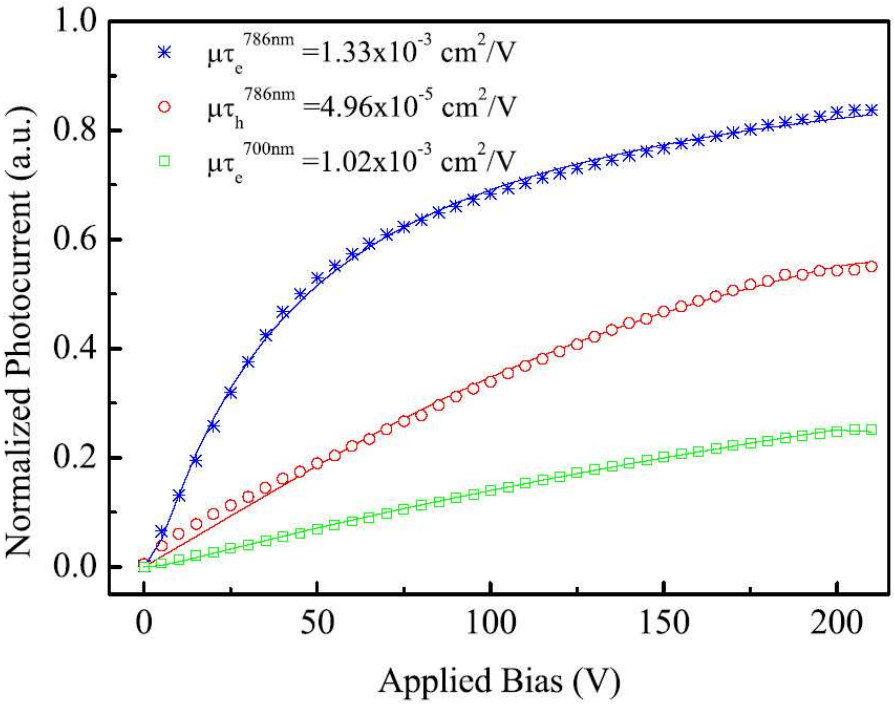

Figure 3.14: Illuminated I-V curves for 786 nm and 700 nm. The experimental curves are normalized to the saturation current I_0 occurring at at high electric field. The solid lines are the fitting results. The curve for holes refer to the use of a neutral filter with $OD = 1.5$; the other ones were acquired without filters. [45]

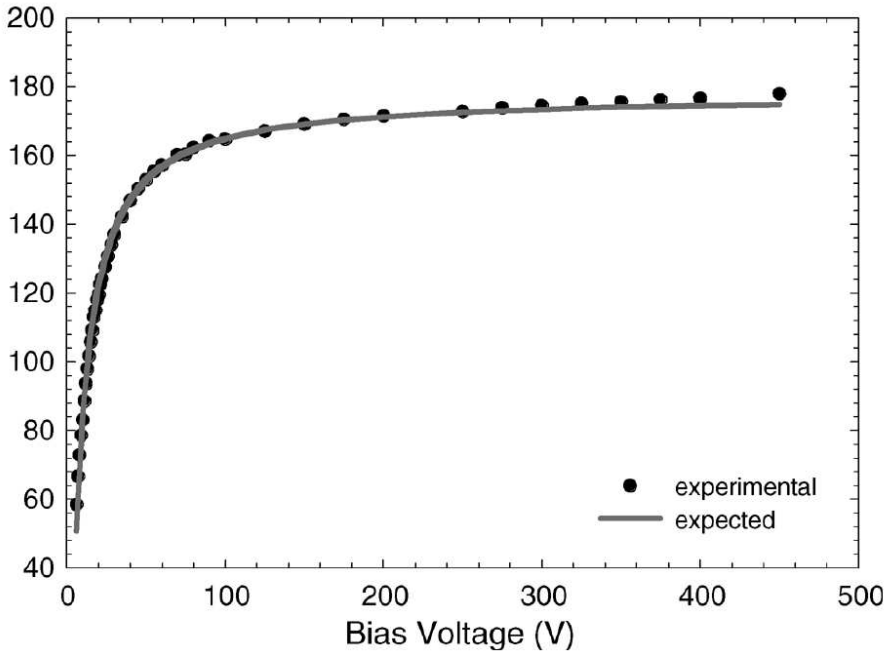

Figure 3.15: Centroid of the 22 keV photopeak of ^{109}Cd as a function of the bias voltage. The solid line is the result of the fitting by the simplified Hecht equation. [35]

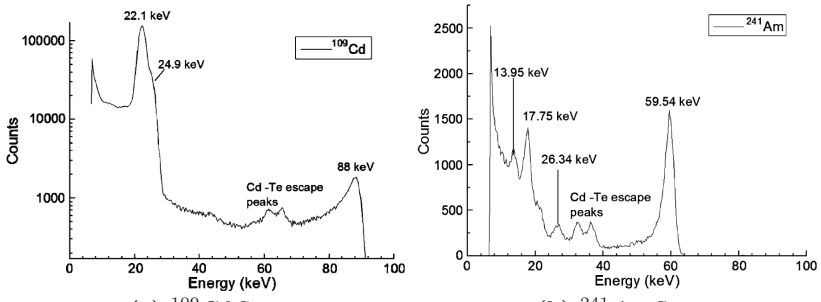

(a) ^{109}Cd Source **(b)** ^{241}Am Source

Figure 3.16: X-ray spectrum of a CdZnTe detector [35]

Chapter 4

Modelization

In this chapter we study the signal generation from the system constituted by a planar CZT detector and a Charge-Sensitive Preamplifier (CSP). A preamplifier stadium is fundamental to achieve good level of signal to noise ratio, then we will consider this component in our model. These calculations are performed starting from the solution of free-carrier dynamics, and from the R-S theorem with thee step:

1. First we calculate the analytical solution for free carrier distribution and its dynamic in the semi-insulator.
2. Then we calculate the two current components (for the electron and for the hole case) generated by the detector according to the R-S theorem.
3. Finally the output signal will be calculated convolving this analytical solution with the read-out electronic transfer function, according with the signal theory.

Several attempts to modelize the signal output for hard-radiation detectors has been made, as for exaple in [5, 69–71]. Each of these with its approximations and its generality degree. Now, in the next sections, we will show the our model for planar detector.

4.1 Read-out electronics

As we can see in figure 4.1 the CZT detector is biased with the resistor R_0 and the signal generated by the detector, in response of a photon absorption, is collected by the CSP through an isolation capacitor C_{in}. The value of this resistor (on the order of $100 - 300M\Omega$) must be such high to force the generated current through the capacitor, but low enough compared to the detector series resistance R_d (this is the detector internal resistance and normally is larger than of $1G\Omega$) to ensure the detector polarization. Concerning the capacitor, its value must be as high as possible to ensure a long time constant and the

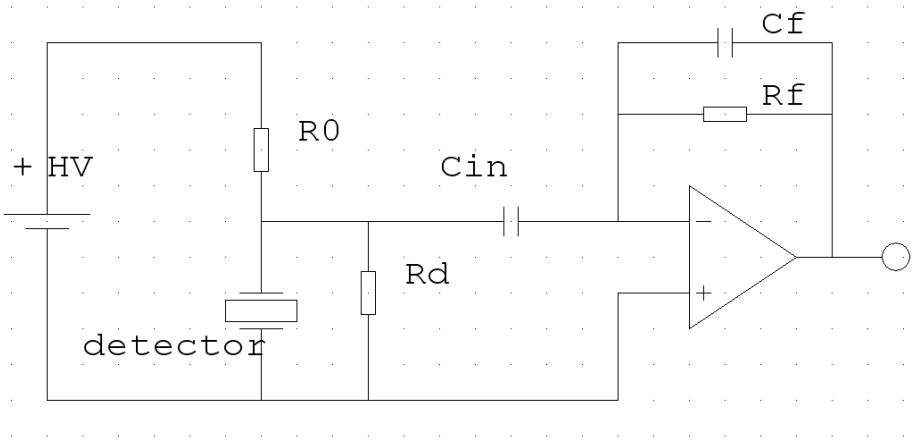

Figure 4.1: Detector and Charge Sensitive Preamplifier

integration of almost all the frequency components. Typical values are in the range $1nF - 10nF$.
The read-out transfer function can be defined as

$$F(\omega) = \frac{O(\omega)}{I(\omega)} = -Z_f(\omega) \tag{4.1}$$

where $I(\omega)$ is the input current component with pulsation ω and $O(\omega)$ the corresponding output. In our case it has physical dimensions of an impedence. Referring to the figure 4.1, we can write the read-out electronic transfer function as a function of the complex pulsation $s = \omega_1 + j\omega_2$

$$Z_f(s) = \frac{1}{C_f} \frac{s\tau_{in}}{1 + s\tau_{in}} \frac{\tau_f}{1 + s\tau_f} \tag{4.2}$$

Anti-transforming the transfer function, we obtain the impulse response of the read-out electronics in the time domain.

$$f(t) = -\frac{1}{C_f} \frac{\tau_{in}\tau_f}{\tau_f - \tau_{in}} \left(\frac{exp\left\{-\frac{t}{\tau_{in}}\right\}}{\tau_{in}} - \frac{exp\left\{-\frac{t}{\tau_f}\right\}}{\tau_f} \right) \tag{4.3}$$

where R_{in} is the parallel between the bias resistance R_0 and the detector series resistance R_d, $\tau_{in} = R_{in}C_{in}$ and $\tau_f = R_fC_f$.
When $t << max\{\tau_{in}, \tau_f\}$, exploiting the Taylor series, at the first order we can write:

$$f(t) = -\frac{exp\left\{-\frac{t}{\tau_i}\right\}}{C_f} \tag{4.4}$$

where τ_i is the integration time given in according to the relation:

$$\frac{1}{\tau_i} = \frac{1}{\tau_{in}} + \frac{1}{\tau_f} \tag{4.5}$$

In our case, t will be always at least 10 times lower than both τ_f and τ_{in} (these last two time constants are in the order of $300 - 1000\mu s$), then we will work with the approximated transfer function.
Once we have obtained the transfer function $f(t)$ and supposing to know the input signal $i(t)$ it is possible to calculate the output as:

$$o(t) = \int_{-\infty}^{t} i(t) f(t-\theta) d\theta \tag{4.6}$$

according to the signal theory.

4.2 Sensor signal

As pointed out in the introduction, the current induced on the sensor electrode is due to the drifting charge in the sensor itself, according to the R-S theorem. If a charge Q_0 drifts inside the detector from $\vec{x}(O)$ to $\vec{x}_(t)$, we can express the induced charge as

$$\Delta Q_i = Q_i(t) - Q_i(0) = Q_0 \left(W\left(\vec{x}(t)\right) - W\left(\vec{x}(0)\right)\right) \tag{4.7}$$

where $W(\vec{x})$ is the weighting potential. To achieve the induced current expression, we must differentiate the $Q_i(t)$ expression. In general we should considerate that also the amount of drifting charge could vary (i.e. $Q_0 = Q(t)$) because of trapping, detrapping and recombination phenomena: then taking the derivative we have two term at the right-hand member

$$i_i(t) = \frac{dQ_i(t)}{dt} = Q(t)\vec{\nabla} W \cdot \frac{d\vec{x}}{dt} + \frac{dQ}{dt} W\left(\vec{x}(t)\right) \tag{4.8}$$

The first term in the right-hand member takes into account all the phenomena that affects the amount of drifting charge (trapping detrapping and ricombination). The second term, instead, takes in account the distruction or the generation of charge fixed in the point $\vec{x}(t)$: Because of the charge conservation law this second term is null. In other words, once generated the electron and hole clouds are separated and, until its complete collection, the charge present in the detector is Q_0. The trapping or detrapping phenomena could vary only the amount of drifting charge, indeed the trapped charge it still present even if blocked. Concerning the ricombination, also this process do not vary the charge present in the crystal; besides this process is quite rare in a semi-insulator material because of the low concentartion of free-carrier. Indeed the thermalization processes concerning the excess of free carriers are carried out in a time-scale given by the relaxation dielectric constant $\tau_{DR} = \epsilon/\sigma = \epsilon\rho$, where σ is the

material conductivity, $\rho \approx 10^8 \Omega m$ the material resistivity and $\epsilon \approx 10^{-10} F/m$ the dielectric constant. So the time-scale for recombination processes is given by $\tau_{DR} \approx 10ms$ when there are no external applied fields, more again, when we apply an external field, the thermalization time will be greater because the carriers will be separated each other.
Only the thermal ionization could be a souce of new drifting charge, but the high energy gap makes negligible this phenomenon, anyway the thermal ionization is responsible of the leackage current.

4.2.1 The Hecht's case

Hecht [3] in 1932 built his model making some hypotheses:

- Planar detector: the detector can be thought as a planar capacitor, then the field inside the detector is uniform and perpendicular to the electrode surfaces and similar consideration can be done for the weighting field.

$$\vec{E} = -E\hat{i}$$
$$\vec{w} = \nabla\vec{W} = \frac{1}{L}\hat{i}$$

  where L is the detector thickness. The resulting carrier speeds are $\vec{v_e} = \mu_e\vec{E}$ for the electrons and $\vec{v_h} = \mu_h\vec{E}$ for the holes. The hole mobility is positive while the electron one is negative, but hereafter, without other specifications, we will consider this quantities as positive.

- A number of pairs electron-hole, proportional to the absorbed photon energy, are generated instantly when the photon hits the crystal. The carriers are separated by the internal field and drift towards its respective collecting electrodes.
- Free electrons (holes) are trapped with a characteristic time τ_{te} (τ_{th}).
- Detrapping processes are negligible.
- Recombination phenomena are not present

Under these hypotheses we can consider the drifting charge as punctiform. Due to the trapping we can express this amount as

$$Q(t) = Q_0 \exp\left\{-\frac{t}{\tau_t}\right\} \tag{4.9}$$

So the current becomes

$$Q(t) = \frac{Q(t)}{T_c} = Q_0 \frac{\mu_c E}{L} \exp\left\{-\frac{t}{\tau_t}\right\} \tag{4.10}$$

where τ_t is the carrier trapping time, μ_c carrier mobility and T_c the detector crossing time. For a planar detector we have $E = \frac{V}{L}$ so we can write T_c as:

$$T_c = \frac{L}{v_c} = \frac{L}{\mu_c E} = \frac{L^2}{\mu_c V} \tag{4.11}$$

4.2.2 Detrapping

Trapping and detrapping combined effect spread the spatial distribution of free carriers, so that the charge cannot again considered as punctiform but distributed along the path covered by the carriers. Indeed as a consequence of the detrapping process each point of this track becomes a source of new carriers that have been trapped before. For this reason we must integrate along this path (in our hypotheses a straight line parallel to the internal field).
In this case we obtain both for the electron and the hole component:

$$i(t) = \int_0^L \rho(\vec{x},t)\vec{v}(x)\cdot\vec{w}(x)dx = \tag{4.12}$$

$$= \frac{\mu_c V}{L^2}\int_0^L \rho(x,t)dx \tag{4.13}$$

where ρ is the free charge density (both for electrons and hole). This because $vecv(x)$ and $vecv\omega(x)$ are parallel and the charges drift in a stright line along the x axis. Besides because of the uniformity of the field in the planar detector the problem can be considered one-dimensional we can omit the vector symbols.

4.3 The carrier density solution

In the previous sections we have introduced the fundamental ingredients to calculate the output signal for the system constituted by the detector and by the read-out electronics. For the simplest case (Hecht) the solution could be yet calculated, but for the most general case we need to calculate the free charge density $\rho(x,t)$ both for electrons and holes, as suggested by the equation 4.13. Now it will be outlined and performed the solution of this problem even for a planar detector.

4.3.1 Starting hypotheses and framework

Framework As pointed out in the introduction, we can write the Boltzmann equation as:

$$\frac{\partial\rho}{\partial t} = G - U - \vec{\nabla}\cdot\vec{J} \tag{4.14}$$

where G and U are the generation and destruction rate. For an incompressible fluid holds $\vec{J} = \rho\vec{v}$, then

$$\vec{\nabla}\cdot\vec{J} = \vec{\nabla}\cdot(\rho\vec{v}) =$$
$$= \vec{\nabla}\rho\cdot\vec{v} + \rho\vec{\nabla}\cdot\vec{v} \tag{4.15}$$

Inside an isotropic and homogeneus semiconductor crystals the free carrier drift speed is given by $\vec{v} = \mu\vec{E}$, so we get

$$\frac{\partial\rho}{\partial t} = G - U - \mu(\vec{\nabla}\rho\cdot\vec{E} + \rho\vec{\nabla}\cdot\vec{E}) \tag{4.16}$$

The carrier densities are not incompressible fluids, then we have also a diffusive term and the equation becomes

$$\frac{\partial \rho}{\partial t} = G - U - \mu(\vec{\nabla}\rho \cdot \vec{E} + \rho\vec{\nabla} \cdot \vec{E}) - D\nabla^2\rho \tag{4.17}$$

where D is the diffusion coefficient and $U = U_t + R$, with U distruction rate U_t trapping rate and R recombination rate.

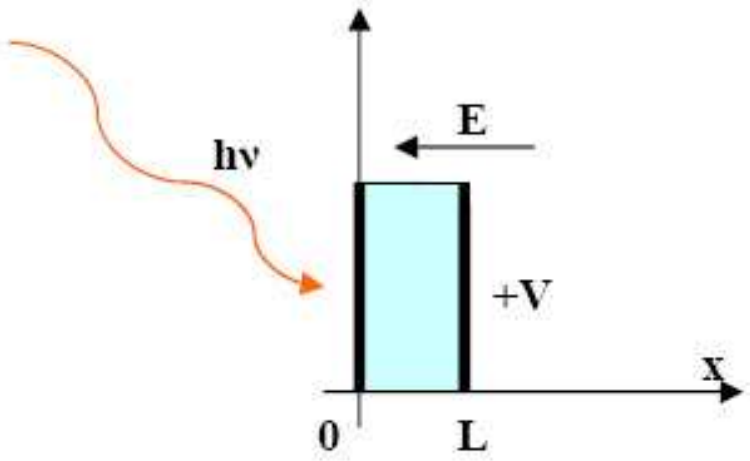

Figure 4.2: Detector

Hypotheses To perform our calculation we need to do some hypotheses to introduce them in the Boltzmann equation:

1. Uniform electric field along the x axis (but with opposite direction) as shown in figure **??**:
$$\vec{E} = -E\hat{i}$$
with $E > 0$, so that
$$\vec{\nabla} \cdot \vec{E} = 0$$

2. One-dimensional system (the charge carriers move only along the x axis):
$$\vec{\nabla} = \frac{\partial}{\partial x}\hat{i}$$

3. The trapping rate U is proportional to the excess of free charge ρ:
$$U_t = \frac{\rho(x,t)}{\tau_t}$$
This is equivalent to state that the trap density is always much greater than the free carrier density.

4. The generation rate G is proportional to the excess of trapped charge ρ_t:

$$G = \frac{\rho_t(x,t)}{\tau_d}$$

5. There are no recombination phenomena ($R = 0$), as usual in semi-insulator as CZT:

$$\tau_r \to \infty$$

with τ_r recombination time.

6. The density of free carriers in thermal equilibrium ρ_0 is negligible in comparison with the excess of free carrier photo-generated $\rho(x,t)$ (because the material is semi-insulator):

$$\rho(x,t) - \rho_0 \approx \rho(x,t)$$

then $\rho_0 \approx 0$.

7. The diffusion effects are negligible

$$D = 0$$

4.4 Problem solution

Hereafter we will work, not jet with the free charge density $\rho(x,t)$, but with the free carrier density $n(x,t) = \rho(x,t)/(kq)$ (independent of the carrier sign), where k is the sign of the charge of carrier

$$k = \begin{cases} +1 & \text{holes} \\ -1 & \text{electrons} \end{cases}$$

and q is the (absolute value of the) electron charge. With these conventions we can express the physical problem in the sequent mathematical form

$$\begin{cases} \frac{\partial n(x,t)}{\partial t} &= -\frac{n(x,t)}{\tau_t} + \frac{n_t(x,t)}{\tau_d} + k\mu E \frac{\partial n(x,t)}{\partial x} \\ \frac{\partial n_t(x,t)}{\partial t} &= \frac{n(x,t)}{\tau_t} - \frac{n_t(x,t)}{\tau_d} \end{cases} \tag{4.18}$$

with boundary conditions

$$n(x,0) = n_0\delta(x - x_0) \tag{4.19}$$

$$n_t(x,0) \equiv 0 \tag{4.20}$$

where n_t is the trapped carrier density and whereμ and E are now considered as positive.
These conditions express the instantaneous generation of n_0 electron-hole pairs at the time $t = 0$ in the position $x = x_0$. It is noteworthy that n_0 is a pure

number while $n(x,t)$ is a density of carriers with dimensions of a reciprocal length (the system is supposed one-dimensional). Indeed the Dirac's delta is an integral object, then, because of its integral value must be dimensionless, its physical dimensions are the reciprocal of its argument.
Substituting the second equation in the system into the first, we can rewrite the system 4.18 as:

$$\begin{cases} \frac{\partial n}{\partial t} + \frac{\partial n_t}{\partial t} &= k\mu E \frac{\partial n}{\partial x} \\ \frac{\partial n_t}{\partial t} &= \frac{n}{\tau_t} - \frac{n_t}{\tau_d} \end{cases} \tag{4.21}$$

4.4.1 Laplace transform

Making the Laplace transform of the system 4.21

$$F(s) = L\{f(t)\} = \int_0^\infty e^{-st} f(t) dt$$

with the relative boundary condition, we obtain:

$$\begin{cases} s[N(x,s) + N_t(x,s)] - [n(x,0) + n_t(x,0)] &= k\mu E \frac{\partial N(x,s)}{\partial x} \\ sN_t(x,s) - n_t(x,0) &= \frac{N(x,s)}{\tau_t} - \frac{N_t(x,s)}{\tau_d} \end{cases} \tag{4.22}$$

otherwise

$$\begin{cases} sN[1 + \frac{1}{\tau s + r}] - k\mu E \frac{\partial N}{\partial x} &= n_0 \delta(x - x_0) \\ N_t &= \frac{N}{\tau s + r} \end{cases} \tag{4.23}$$

with $\tau = \tau_t$ ed $r = \tau_t / \tau_d$.
Calling

$$\omega(s) = s\left[1 + \frac{1}{\tau s + r}\right] =$$
$$= (s + \frac{1}{\tau}) - \frac{r}{\tau(\tau s + r)}$$

we can rewrite the first equation as

$$N(x,s) - \frac{k\mu E}{\omega(s)} \frac{\partial N(x,s)}{\partial x} = \frac{n_0}{\omega(s)} \delta(x - x_0) \tag{4.24}$$

The homogeneous equation solution can be expressed as

$$N(x,s) = N(x_0,s) \exp\left\{ \frac{\omega(s)}{k\mu E}(x - x_0) \right\} \tag{4.25}$$

So we can search for a particular solution in the form (Method of variation of parameters):

$$N(x,s) = A(x)\exp\left\{\frac{\omega(s)}{k\mu E}(x-x_0)\right\} \tag{4.26}$$

Then, after substituting the above solution in the complete differential equation we obtain the condition:

$$N'(x) = -\frac{n_0}{k\mu E}\delta(x-x_0)\exp\left\{-\frac{\omega(s)}{k\mu E}(x-x_0)\right\} \tag{4.27}$$

Now

$$\begin{aligned} N(x) &= -\frac{n_0}{k\mu E}\int_0^{x>0}\delta(x-x_0)\exp\left\{-\frac{\omega(s)}{k\mu E}(x-x_0)\right\}dx = \\ &= -\frac{n_0}{k\mu E}H(x-x_0)+c_0(s) \end{aligned} \tag{4.28}$$

where $H(x-x_0)$ is the Heaviside's step function. Because we are looking for a particular solution, we can choice $c_0(s)=0$.

$$N(x,s) = -\frac{n_0}{k\mu E}H(x-x_0)\exp\left\{\frac{\omega(s)}{k\mu E}(x-x_0)\right\} \tag{4.29}$$

Adding a particular non-homogeneous solution to the general integral of the homogeneous differential equation, we achieve the general solution for the complete system. So the non-homogeneous general integral is given by

$$N(x,s) = n_0\left[\alpha(s) - \frac{H(x-x_0)}{k\mu E}\right]\exp\left\{\frac{\omega(s)}{k\mu E}(x-x_0)\right\} \tag{4.30}$$

Now we can do some dimensional considerations:

- The argument in the square brackets has physical dimensions of a reciprocal speed. Indeed the Heaviside's function and k are dimensionless and μE is a speed.
- From the previous point we deduce that also α must be a reciprocal velocity and this fits good with the expected physical dimensions of $N(x,s) = L\{n(x,t)\}$.

To determine $\alpha(s)$ we have to impose the initial condition

$$n(x,0) = n_0\delta(x-x_0)$$

Then we must take the Laplace anti-transform.

4.4.2 Laplace anti-transform

Substituting the value of $\omega(s)$ into the Laplace transformed function $N(x,s)$ we obtain:

$$N(x,s) = n_0 \left[\alpha(s) - \frac{H(x-x_0)}{k\mu E} \right] \exp \left\{ \frac{x-x_0}{k\mu E} \left[\left(s + \frac{1}{\tau} \right) - \frac{r}{\tau(\tau s + r)} \right] \right\} \tag{4.31}$$

Now we choose the $\alpha(s)$ value. There are two cases:

1. When the carriers are electrons $k = -1$ and on the left of x_0 the free carrier density must becomes 0

   $$n(x,t) = 0 \qquad \forall t \quad \forall x < x_0$$

   as a consequence we have

   $$\alpha(s) = 0 \tag{4.32}$$

   then

   $$\begin{aligned} N(x,s) &= N_e(x,s) = \qquad (4.33) \\ &= n_0 \left[\frac{H(x-x_0)}{-k\mu E} \right] \exp \left\{ \frac{x-x_0}{k\mu E} \left[\left(s + \frac{1}{\tau} \right) - \frac{r}{\tau(\tau s + r)} \right] \right\} \end{aligned}$$

   where the subscript e indicates the electron case.

2. when the holes are the free carriers, we have $k = +1$ and, because the carriers move to the left, we impose that the free carrier density must vanish on the right of x_0 at all times t, so:

   $$n(x,t) = 0 \qquad \forall t \quad \forall x > x_0$$

   from which we have

   $$\alpha(s) = \frac{1}{k\mu E} \tag{4.34}$$

   and finally:

   $$\begin{aligned} N(x,s) &= N_h(x,s) = \qquad (4.35) \\ &= n_0 \left[\frac{1 - H(x-x_0)}{k\mu E} \right] \exp \left\{ \frac{x-x_0}{k\mu E} \left[\left(s + \frac{1}{\tau} \right) - \frac{r}{\tau(\tau s + r)} \right] \right\} \end{aligned}$$

   where the subscript h indicates the hole-case.

The quantity before the exponential is a constant in s and it is not changed by the Laplace anti-transform. The exponential can be seen as the product of two exponentials and then as the convolution of the two anti-transformed functions $f_1(t) = L^{-1}\{F_1(s)\}$ and $f_2(t) = L^{-1}\{F_2(s)\}$. Since, both for the electron and the hole case, we have $-k\mu E = v$ (where v is the carrier drift speed) and the quantities $(x - x_0)$ and v are always agree in sign, we can write:

$$\begin{aligned} \frac{x - x_0}{k\mu E} &= -\frac{x - x_0}{v} \leq 0 \\ F_1(s) &= \exp\left\{ -\frac{x - x_0}{v\tau}(\tau s + 1)\right\} \\ F_2(s) &= \exp\left\{ \frac{x - x_0}{v\tau}\frac{r}{(\tau s + r)}\right\} \end{aligned}$$

Now under this hypothesis (i.e. the real part of the exponential argument in the first function $F_1(s)$ is negative) it is possible to make both the two anti-transformations, obtaining

$$f_1(t) = \exp\left\{ -\frac{x - x_0}{v\tau}\right\}\left[\delta\Big(t - \frac{x - x_0}{v}\Big)H\Big(t - \frac{x - x_0}{v}\Big)\right] \quad (4.36)$$

$$f_2(t) = \frac{\exp\left\{-\frac{rt}{\tau}\right\}}{\tau}\left[\frac{\sqrt{r\frac{x-x_0}{v\tau}}\, I_1\Big(2\sqrt{r\frac{t}{\tau}\frac{x-x_0}{v\tau}}\Big)}{\sqrt{\frac{t}{\tau}}} + \delta\Big(\frac{t}{\tau}\Big)\right] \quad (4.37)$$

In particular the last two equations remain valid as long as the root arguments are positive or at least zero. Then until we have $t > 0$ e $T(x) = \frac{x-x_0}{v} \geq 0$. Remembering the meaning of symbols r e τ and also of the relation

$$\int_{-\infty}^{+\infty} \delta(\theta - t_0) f(t - \theta) d\theta = f(t - t_0)$$

and convolving together the two anti-transformed functions 4.36 and 4.37 (with the multiplicative constant) with some mathematical arrangement we obtain the solution valid for both the electron and the hole-case:

$$\begin{aligned} n_c(x,t) = n_0\left[\alpha + \frac{H(x - x_0)}{v}\right] e^{-\frac{T(x)}{\tau_D}} H(0) \frac{e^{-\frac{t-T(x)}{\tau_D}}}{\tau_T} \\ \left[\frac{2\sqrt{\frac{T(x)}{\tau_D}\frac{t-T(x)}{\tau_T}}\, I_1\Big(2\sqrt{\frac{T(x)}{\tau_D}\frac{t-T(x)}{\tau_T}}\Big)}{2\frac{t-T(x)}{\tau_T}} + \delta\Big(\frac{t - T(x)}{\tau_T}\Big)\right] \end{aligned} \quad (4.38)$$

that is valid until $t > T(x) > 0$ and that becomes zero elsewhere. A similar solution can be found in [5] where the authors have supposed a single carrier

transport phenomena (the photon is supposed to be absorbed at $x = 0$). We must deal separately the case $T(x) = 0$ where the solution behaves like a Dirac's delta function in time. Although normally $H(x - x_0)$ is defined so that $H(0) = 1/2$, in our case, since the charge is generated in x_0, we define $H(0) = 1$. The $I_\nu(z)$ function, instead, can be written by the series expansion:

$$I_\nu(z) = \left(\frac{1}{2}z\right)^\nu \sum_{k=0}^{\infty} \frac{\left(\frac{1}{4}z^2\right)^k}{k!\,\Gamma(k+\nu+1)} \tag{4.39}$$

With such preliminary remarks, if we calculate the limit of $n(x,t)$ for $t \to 0$ (and therefore also for $T(x) \to 0$, because $t \geq T(x)$), exploiting the relation

$$\delta\Big(\frac{t}{\tau}\Big) = |\tau|\delta(t) \tag{4.40}$$

we achieve:

$$\lim_{t\to 0} n(x,t) = n_0 v \left\{\alpha + \frac{H(x-x_0)}{v}\right\} \delta(x - x_0) \tag{4.41}$$

that appears to be a spatial Dirac's delta as required by the initial conditions. As just said above, the solutions 4.39 (one for elctrons and one for holes) are valid within the interval $t \geq T(x) \geq 0$ and becomes zero elsewhere, so, both for the electron and the hole-case, they can be expressed, for all times t, as:

$$\begin{aligned} n(x,t) &= n_0 \left[\frac{H(x-x_0)}{v\tau_T}\right] \exp\left\{-\left[\frac{T(x)}{\tau_T} + \frac{t-T(x)}{\tau_D}\right]\right\} H\big(t-T(x)\big) \\ &\quad H\big(T(x)\big)\left[\frac{2\sqrt{\frac{T(x)}{\tau_D}\frac{t-T(x)}{\tau_T}}\; I_1\Big(2\sqrt{\frac{T(x)}{\tau_D}\frac{t-T(x)}{\tau_T}}\Big)}{2\frac{t-T(x)}{\tau_T}} + \delta(\frac{t-T(x)}{\tau_T})\right] \end{aligned} \tag{4.42}$$

$$\begin{aligned} p(x,t) &= n_0 \left[\frac{1-H(x-x_0)}{|v|\tau_T}\right] \exp\left\{-\left[\frac{T(x)}{\tau_T} + \frac{t-T(x)}{\tau_D}\right]\right\} H\big(t-T(x)\big) \\ &\quad H\big(T(x)\big)\left[\frac{2\sqrt{\frac{T(x)}{\tau_D}\frac{t-T(x)}{\tau_T}}\; I_1\Big(2\sqrt{\frac{T(x)}{\tau_D}\frac{t-T(x)}{\tau_T}}\Big)}{2\frac{t-T(x)}{\tau_T}} + \delta(\frac{t-T(x)}{\tau_T})\right] \end{aligned} \tag{4.43}$$

and for $t = T(x) = 0$ they behave like two Dirac's delta functions.

4.5 Output signal calculation steps

In the previous sections we have laid the foundation for the output signal calculation. Let's us recall the fundamental steps:

- According to the R-S theorem, the induced current on the detector electrodes generated by a drifting charge $Q(t)$ moving along a trajectory $\vec{x}(t)$ with a velocity $\vec{v}(x)$ is given by

$$i(t) = Q(t)\vec{v}(x) \cdot \vec{w}(x) \tag{4.44}$$

  where $\vec{w}$ is the "weighting field ", namely the coupling field between the electrode and the charge displacement. The field measures the coupling between the drift current and the electrode and has physical dimensions of a reciprocal length.

- The drifting charge has a spatial distribution $\rho(x,t)$. Once we have drawn out them, it is possible to generalize the above formula as

$$i(t) = \frac{\mu V}{L^2} \int_0^L \rho(x,t)\vec{v}(x) \cdot \vec{w}(x) dx \tag{4.45}$$

  In our case $\vec{v}(x) = \mu E\hat{i}$ and $\vec{w}(x) = 1/L\hat{i}$ are parallel and constant in x, so that, remembering $E = V/L$, we can write

$$i(t) = \frac{\mu V}{L^2} \int_0^L \rho(x,t) dx = \frac{\mu V}{L^2} Q(t) \tag{4.46}$$

  where V is the applied bias.

- Finally the output signal is given by the convolution between the current signal and the read-out electronic transfer function.

4.5.1 The drifting charge

Let's define the quantities

$$T_c(x_0) = \begin{cases} T_e(x_0) = \frac{L-x_0}{v} & \text{in the electronic-case} \\ T_h(x_0) = \frac{x_0}{v} & \text{in the hole case} \end{cases} \tag{4.47}$$

There are two cases:

1. If $t > T_c(x_0)$ we have to calculate the value of

$$Q(t) = \int_0^L \rho(x,t) dx \tag{4.48}$$

   and in general the analytical solution does not exists.

2. If $t < T_c(x_0)$, no carrier has reached the collecting electrode. So the integration between 0 and L is equivalent to the integration between 0 and ∞, then:

$$Q(t) = \int_0^L \rho(x,t) dx = \int_0^\infty \rho(x,t) dx = Q_0 \frac{\tau_t \tau_d}{\tau_t + \tau_d} \left(\frac{e^{-\left(\frac{1}{\tau_t} + \frac{1}{\tau_d}\right)t}}{\tau_t} + \frac{1}{\tau_d} \right) \tag{4.49}$$

The last integral 4.49 in the equality chain could be calculated by means of residues calculation, but we can be convinced of the correctness of this result (equation 4.49), solving the following system of coupled differential equation

$$\begin{cases} \frac{dn}{dt} &= -\frac{dn_t}{dt} \\ \frac{dn_t}{dt} &= \frac{n}{\tau_t} - \frac{n_t}{\tau_d} \end{cases} \tag{4.50}$$

with initial condition 4.19 $n(0) = n_0$.
This system is fully equivalent to the one previously solved, except for the transport term that does not change the number of carrier crossing the crystal at least until $t < T_c(x_0)$. Until is verified this last condition, it is possible neglect the free carrier distribution inside the detector because the weighting field is constant and no carrier has reached its collecting electrodes; then the systems 4.21 and 4.50 are equivalent for our considerations.
This solution is still valid, for continuity, also when $t = T_c(x_0)$.

There are several cases in which it is possible to do some approximations:

- The first case is the Hecht's case (see section 1.2.1), where we make the additional assumption that there is no detrapping effect in the crystal. this hypothesis can be expressed assuming $\tau_d \to \infty$.
- In the second case we assume that the carrier lifetime τ_t is much larger than the sensor crossing time T_c. Then we can consider the detrapping current as a correction of the Hecht solution.
- In the third case we assume that the carrier lifetime τ_t is much smaller than the sensor crossing time T_c. So after an initial transient where we have a similar-Hecht solution, the system achieves a stationary condition, where the current is damped by the effective carrier mobility.

4.5.2 The Hecht's case

The simplest case that we encounter is the Hecht case. In this case the drifting charge can be considered as constituted of two punctiform charges

$$Q(t) = Q_0 \exp\left\{-\frac{t}{\tau_t}\right\}$$

one for each kind of the carrier, moving with speed $\mu_c E$ toward the collecting electrodes without detrapping effect spreading the charge distribution.
Let's suppose that an high energy photon is absorbed by the crystal at the time $t = 0$ in $x = x_0$ generating an initial charge Q_0. We have two carrier clouds drifting towards the collecting electrodes located respectively at $x = 0$, in the hole-case, and at $x = L$ in the electron-case (L is the crystal thickness). Calling

$\xi_0 = x_0/L$ the impact relative depth, the crossing times employed by electrons and hole to reach their collecting electrodes are given by

$$T_e(\xi_0) = T_e(x_0) = \frac{L - x_0}{|\mu_e|E} = (1 - \xi_0)T_e \tag{4.51}$$

$$T_h(\xi_0) = T_h(x_0) = \frac{x_0}{\mu_h E} = \xi_0 T_h \tag{4.52}$$

We should consider the detector current positive when moves towards the CSP input and or this reason the detector current should be considered as negative. Nevertheless we have always considered the current as positive, because this is only a mathematical convenction and also because the read-out transfer function is negative. So we will continuate to consider both the quantities as positive.

$$\begin{aligned} i(t) &= i_e(t) + i_h(t) = \\ &= Q_0 \left[\frac{\mu_e V}{L^2} \exp\left\{ -\frac{t}{\tau_{te}} \right\} + \frac{\mu_h V}{L^2} \exp\left\{ -\frac{t}{\tau_{th}} \right\} \right] \end{aligned} \tag{4.53}$$

where the two contributes are turned on until $t < T_e(\xi_0)$ for the electron-contribution and $t < T_h(\xi_0)$ for the hole-contribution.

4.5.3 Fast carriers

In the second case, we suppose a carrier lifetime τ_t much greater than the collecting time T_c. Under this hypothesis the situation is similar to the Hecht's one: there is only an additional term due to the (detrapping) re-emission of trapped charge. Because of $\tau_t >> T_c$, as a first approximation we can considerate the charge carriers trapped at most once. The total amount of trapped charge Q_t is given with good approximation by

$$Q_t = Q_0 \frac{T_c(\xi)}{\tau_t} \tag{4.54}$$

evenly distributed along the carrier path. For $t \geq T_c(x_0)$, the charge $dQ_t(t)$ trapped in a spatial interval dx, between x_0 and the collecting electrode can be written as:

$$dQ_t(x,t) = Q_0 \exp\left\{ -\frac{x - x_0}{v\tau_t} \right\} \frac{dx}{v\tau_t} \exp\left\{ \frac{t - \frac{x-x_0}{v}}{\tau_d} \right\} \tag{4.55}$$

Indeed the drifting charge located in x at the time $t = \frac{x-x_0}{v}$ is given by $Q_0 \exp\left\{ -\frac{x-x_0}{v\tau_t} \right\}$ and the probability that a carrier is trapped crossing the interval dx can be written as $\frac{dt}{\tau_t} = \frac{dx}{v\tau_t}$. The trapped charge is then re-emitted with a time constant τ_d, starting from the time $t = \frac{x-x_0}{v}$, when it has been trapped.

Dividing for dx and taking the derivative with the opposite sign we get the (detrapped) emerging charge density

$$\rho^d_{xt}(x,t) = -\frac{\partial^2 Q_t}{\partial x \partial t} = \tag{4.56}$$

$$= Q_0 \frac{\exp\left\{-\frac{x-x_0}{v\tau_t}\right\}}{v\tau_t\tau_d} \exp\left\{-\frac{t-\frac{x-x_0}{v}}{\tau_d}\right\} \tag{4.57}$$

The subscripts are to indicate that $\rho^d_{x,t}$ is a derivative of a charge in x and t.
To get the current $i_d(t)$, due to detrapping, we have to calculate the total free charge drifting in the material and apply the R-S theorem. If we neglect further absorptions, the time employed, by a carrier emerging in x, to reach the collecting electrode is given by $T_c(x) = \frac{x_f - x}{v}$, so, if we are interested to the drifting charge at the time $t \geq T_c(x_0)$, we should integrate the charge density in x and in t according to the relation

$$Q_d = \int_{x_0}^{x_f} \int_{t-T_c(x)}^{t} \rho_{xt}(x,t) dt dx \tag{4.58}$$

In general at the time $t \geq 0$ a carrier could be moved from x_0 to $x_m(t)$, where

$$x_m(t) = \begin{cases} \min\{x_0 + vt, L\} & \text{electronic-case} \\ \\ \max\{x_0 + vt, 0\} & \text{hole-case} \end{cases}$$

v in the hole-case is negative. Then in general for both electrons and holes we have

$$Q_d = \left| \int_{x_0}^{x_m(t)} \int_{t-T_m(x)}^{t} \rho_{xt}(x,t) dt dx \right| \tag{4.59}$$

where $T_m(x) = \frac{x_m - x}{v}$.
Once it has got the drifting charge, dividing for $T_c = \frac{L^2}{|\mu_c| V}$ we obtain the $i_d(t)$ solution. This procedure is correct but the calculation are complicated and we can obtain a similar result in an easier way. Indeed, given a drifting charge Q_0 the density of trapped charge along the path between x_0 and x_f can be obtained dividing Q_t for the length of the path

$$\rho^t_x = \frac{Q_0 T_c}{L\tau_t} \tag{4.60}$$

If we suppose an exponential detrapping rate with time constant τ_d, the density of (detrapped) emerging charge can be obtained multiplying the previous equation for $\exp\left\{-\frac{t}{\tau_d}\right\}$ and taking the time derivative with the opposite sign

$$\rho^d_{xt} = \frac{Q_0 T_c}{L\tau_t\tau_d} \exp\left\{-\frac{t}{\tau_d}\right\} \tag{4.61}$$

The lifetime of a carrier emerging in x is given by the collecting time $T_c(x)$, then to draw out the total drifting charge we need to multiply $\rho_d(x,t)$ by $T_c(x) = \frac{x_f - x}{v}$ and integrate along the carrier path, from x_0 to the collecting electrode x_f

$$\begin{aligned} Q_d(t) &= \frac{Q_0 T_c}{\tau_t \tau_d} \exp\left\{-\frac{t}{\tau_d}\right\} \int_{x_0}^{x_f} T_c(x) dx = \\ &= \frac{Q_0 T_c^2(x_0)}{2\tau_t \tau_d} \exp\left\{-\frac{t}{\tau_d}\right\} \end{aligned} \tag{4.62}$$

Rewriting all with the reduced variables (where $\xi = x/L$) and dividing by T_c we finally get the detrapping current expression

$$i_d(t) = \frac{Q_0 T_c^2(\xi_0)}{2T_c \tau_t \tau_d} \exp\left\{-\frac{t}{\tau_d}\right\} \tag{4.63}$$

This last equation coincides with the second order expansion of the exact solution for $t \geq T_c(\xi_0)$. In general, for $t \geq 0$, we have a similar equation where $T_c(\xi_0)$ is substituted by $T_m(\xi_0)$

$$i_d(t) = \frac{Q_0 T_m^2(\xi_0)}{2T_c \tau_t \tau_d} \exp\left\{-\frac{t}{\tau_d}\right\} \tag{4.64}$$

4.5.4 Slow carrier

The third case is when $T_c(x) \gg max\{\tau_t\}$; in this case, after an initial transient, we can think Q_0 as a drifting charge with reduced velocity v_r

$$v_r = \frac{v \cdot \tau_t}{\tau_t + \tau_d} \tag{4.65}$$

So, asymptotically we have

$$i_d(t) = Q_0 \frac{v_r}{L} = \frac{Q_0}{T_c} \frac{\tau_t}{\tau_t + \tau_d} \tag{4.66}$$

4.6 Signal calculation

To achieve the final result it is necessary to convolve the detector current with the read-out transfer function 4.3 according to the relation

$$o(t) = \int_{-\infty}^{t} i(\theta) f(t-\theta) d\theta \tag{4.67}$$

When $t \ll max\{\tau_{in}, \tau_f\}$ (that is the our case) we can use the approximated transfer function

$$f(t) \approx \frac{e^{-(\frac{1}{\tau_f} + \frac{1}{\tau_{in}})t}}{C_f} \tag{4.68}$$

taken with opposite sign, because of we have considered positive also the detector current. Where $\tau_{in} = R_{in}C_{in}$ with R_{in} parallel between R_0 and R_d and $\tau_f = R_f C_f$. Otherwise

$$f(t) \approx \frac{e^{-\frac{1}{\tau_i}t}}{C_f} \tag{4.69}$$

where

$$\frac{1}{\tau_i} = \frac{1}{\tau_f} + \frac{1}{\tau_{in}}$$

As we have seen in the previous chapter the distribution of free charge consists of two terms

- The Hecht's term describing the fraction of free charge that has never been trapped
- A correction term describing the detrapping-generated current

In this chapter we calculate these two terms. We always have at least the first one, (regardless the approximations made). The second one instead is dependent on the approximations.

4.6.1 Hecht's solution

Convolving the detector current $i(t)$ 4.53 with the CPS approximated transfer function 4.6 we achieve the solution in the Hecht's case

$$\begin{aligned} V(t,\xi_0) &= \frac{Q_0}{C}\left[\frac{\tau_{te}^i}{T_e}\left(\exp\left\{\frac{min\{t,T_e(\xi_0)\}}{\tau_{te}^i}\right\} - 1\right) + \right. \\ &\left. + \frac{\tau_{th}^i}{T_h}\left(\exp\left\{\frac{min\{t,T_h(\xi_0)\}}{\tau_{th}^i}\right\} - 1\right)\right]\exp\left\{-\frac{t}{\tau_i}\right\} \end{aligned} \tag{4.70}$$

where

$$\begin{aligned} \frac{1}{\tau_i} &= \frac{1}{\tau_f} + \frac{1}{\tau_{in}} \\ \frac{1}{\tau_{te}^i} &= \frac{1}{\tau_{te}} - \frac{1}{\tau_i} \\ \frac{1}{\tau_{th}^i} &= \frac{1}{\tau_{th}} - \frac{1}{\tau_i} \end{aligned}$$

4.6.2 Fast carriers

Convolving the approximation of i_d current for the fast carrier-case with the read-out electronic transfer function, for any $t \geq 0$ we get:

$$\begin{aligned} V(t) &= \frac{Q_0 \exp\{-\frac{t}{\tau_i}\}}{2C_f\tau_t\tau_d}\left\{T_c\int_0^{min\{t,T_c(\xi_0)\}}\left(\frac{\theta}{T_c}\right)^2\exp\left\{-\frac{\theta}{\tau_{di}}\right\}d\theta + \right. \quad (4.71) \\ &+ \left. H(t,T_c(\xi_0))\frac{\tau_{di}T_c^2(\xi_0)}{T_c}\left[\exp\left\{-\frac{T_c(\xi_0)}{\tau_{di}}\right\} - \exp\left\{-\frac{t}{\tau_{di}}\right\}\right]\right\} \end{aligned}$$

where

$$\begin{aligned} &\int_0^t\left(\frac{\theta}{T}\right)^2\exp\left\{-\frac{\theta}{\tau}\right\}d\theta = \\ &= \frac{2\tau^3 - \left(2\tau^3 + 2\tau^2 t(\xi_0) + \tau t^2(\xi_0)\right)\exp\left\{-\frac{t}{\tau}\right\}}{T^2} \end{aligned}$$

4.6.3 Slow carriers

Similarly for the slow carrier approximation asymptotically we obtain

$$V(t) = \frac{Q_0\tau_{di}}{C_fT_c}\frac{\tau_t}{\tau_t+\tau_d}\left[1 - \exp\left\{-\frac{t}{\tau_{di}}\right\}\right] \quad (4.72)$$

4.6.4 General solution

As already said above, the general solution for the output is given by

$$\begin{aligned} o(t) &= \int_{-\infty}^t i(\theta)f(t-\theta) = \\ &= \int_{-\infty}^t\left(\int_0^L \rho(x,\theta)\vec{v}(x)\cdot\vec{w}(x)dx\right)f(t-\theta)d\theta \quad (4.73) \end{aligned}$$

Imposing the usual condition (i.e. planar geometry and constant field) $\vec{v}(x)\cdot\vec{w}(x) = 1/T_c$ the solution becomes

$$o(t) = \frac{q}{T_c}\int_{-\infty}^t\left(\int_0^L n_c(x,\theta)dx\right)f(t-\theta)d\theta \quad (4.74)$$

Where $\rho_c(x,t)$ is the free charge density, $n(x,t)$ the free carrier density and q the module of the electron charge. Using the relation

$$\int_{-\infty}^t f(\theta)d\theta = \int_{-\infty}^{+\infty} f(\theta)H(t-\theta)d\theta$$

we can write

$$o(t) = \frac{q}{T_c}\int_{-\infty}^{+\infty}\left(\int_0^L n_c(x,\theta)dx\right)f(t-\theta)H(t-\theta)d\theta \quad (4.75)$$

Now, substituting $n_c(x,t)$ with the equations 4.43 and 4.44, respectively in the electron-case and in the hole-case, and $f(t)$ with 4.69, after some step, we get:

$$\begin{aligned} V_e(t) &= \frac{n_0 q}{T_e C_f}\int_0^L\int_{-\infty}^{+\infty}\left[\frac{H(x-x_0)}{v\tau_t}\right]\exp\left\{-\left[\frac{T(x)}{\tau_t}+\frac{\theta-T(x)}{\tau_d}\right]\right\} \\ &\quad \left[\frac{2\sqrt{\frac{T(x)}{\tau_d}\frac{\theta-T(x)}{\tau_t}}\,I_1\Big(2\sqrt{\frac{T(x)}{\tau_d}\frac{\theta-T(x)}{\tau_t}}\Big)}{2\frac{\theta-T(x)}{\tau_t}}+\delta(\frac{\theta-T(x)}{\tau_t})\right] \\ &\quad \exp\left\{-\frac{t-\theta}{\tau_i}\right\}H\big(\theta-T(x)\big)H\big(t-\theta\big)d\theta dx \qquad (4.76) \end{aligned}$$

$$\begin{aligned} &= \frac{n_0 q}{L\tau_t C_f}\int_{x_0}^L H\big(t-T(x)\big)\int_{T(x)}^t\exp\left\{-\left[\frac{T(x)}{\tau_t}+\frac{\theta-T(x)}{\tau_d}\right]\right\} \\ &\quad \left[\frac{2\sqrt{\frac{T(x)}{\tau_d}\frac{\theta-T(x)}{\tau_t}}\,I_1\Big(2\sqrt{\frac{T(x)}{\tau_d}\frac{\theta-T(x)}{\tau_t}}\Big)}{2\frac{\theta-T(x)}{\tau_t}}\right]\exp\left\{-\frac{t-\theta}{\tau_i}\right\}d\theta dx \\ &\quad +\frac{n_0 q}{LC_f}\exp\left\{-\frac{t}{\tau_i}\right\}\int_{x_0}^L\exp\left\{-\frac{T(x)}{\tau_{ti}}\right\}H\big(t-T(x)\big)dx \qquad (4.77) \end{aligned}$$

for the electrons and similarly for the holes:

$$\begin{aligned} V_h(t) &= \frac{n_0 q}{T_h C_f}\int_0^L\int_{-\infty}^{+\infty}\left[\frac{1-H(x-x_0)}{|v|\tau_t}\right]\exp\left\{-\left[\frac{T(x)}{\tau_t}+\frac{\theta-T(x)}{\tau_d}\right]\right\} \\ &\quad \left[\frac{2\sqrt{\frac{T(x)}{\tau_d}\frac{\theta-T(x)}{\tau_t}}\,I_1\Big(2\sqrt{\frac{T(x)}{\tau_d}\frac{\theta-T(x)}{\tau_t}}\Big)}{2\frac{\theta-T(x)}{\tau_t}}+\delta(\frac{\theta-T(x)}{\tau_t})\right] \\ &\quad \exp\left\{\frac{t-\theta}{\tau_i}\right\}H\big(\theta-T(x)\big)H\big(t-\theta\big)d\theta dx \qquad (4.78) \end{aligned}$$

$$\begin{aligned} &= \frac{n_0 q}{L\tau_t C_f}\int_0^{x_0} H\big(t-T(x)\big)\int_{T(x)}^t\exp\left\{-\left[\frac{T(x)}{\tau_t}+\frac{\theta-T(x)}{\tau_d}\right]\right\} \\ &\quad \left[\frac{2\sqrt{\frac{T(x)}{\tau_d}\frac{\theta-T(x)}{\tau_t}}\,I_1\Big(2\sqrt{\frac{T(x)}{\tau_d}\frac{\theta-T(x)}{\tau_t}}\Big)}{2\frac{\theta-T(x)}{\tau_t}}\right]\exp\left\{-\frac{t-\theta}{\tau_i}\right\}d\theta dx \\ &\quad +\frac{n_0 q}{LC_f}\exp\left\{-\frac{t}{\tau_i}\right\}\int_0^{x_0}\exp\left\{-\frac{T(x)}{\tau_{ti}}\right\}H\big(t-T(x)\big)dx \qquad (4.79) \end{aligned}$$

with

$$\tau_{ti} = \left(\frac{1}{\tau_t} - \frac{1}{\tau_i}\right)^{-1}$$

and

$$T(x) = \frac{x - x_0}{v} = |\xi - \xi_0| T_c \geq 0$$

As it is possible to notice, these integrals are both a sum of two terms: the former is a double integral and has not a finite form and the latter is the Hecht's term. Handling these expressions, we can rewrite them as

$$\begin{aligned} V_e(t) &= \frac{n_0 q}{C_f} \exp\left\{-\frac{t}{\tau_i}\right\} \left[H(\Theta) \int_0^{1-\xi_0} \exp\left\{-\zeta \frac{T_e}{\tau_{ti}}\right\} \right. \\ &\quad P(\zeta) \left(\int_0^{\Theta(\zeta)} \exp\left\{-\frac{\vartheta^2}{4}\right\} I_1\big(P(\zeta)\vartheta\big) d\vartheta \right) d\zeta + \\ &\quad \left. + \frac{\tau_{ti}}{T_e} \left[1 - \exp\left\{ -\frac{min\left\{t, T_e(\zeta)\right\}}{\tau_{ti}} \right\} \right] \right] \end{aligned} \tag{4.80}$$

$$\begin{aligned} V_h(t) &= \frac{n_0 q}{C_f} \exp\left\{-\frac{t}{\tau_i}\right\} \left[H(\Theta) \int_0^{\xi_0} \exp\left\{-\zeta \frac{T_h}{\tau_{ti}}\right\} \right. \\ &\quad P(\zeta) \left(\int_0^{\Theta(\zeta)} \exp\left\{-\frac{\vartheta^2}{4}\right\} I_1\big(P(\zeta)\vartheta\big) d\vartheta \right) d\zeta + \\ &\quad \left. + \frac{\tau_{ti}}{T_h} \left[1 - \exp\left\{ -\frac{min\left\{t, T_h(\zeta)\right\}}{\tau_{ti}} \right\} \right] \right] \end{aligned} \tag{4.81}$$

where

$$\xi = x/L$$

and

$$\begin{aligned} \zeta &= |\xi - \xi_0| \\ \tau_{di} &= \left(\frac{1}{\tau_d} - \frac{1}{\tau_i}\right)^{-1} \\ \Theta(\zeta) &= 2\sqrt{\frac{t - \zeta T_c}{\tau_t}\left(1 - \frac{\tau_d}{\tau_i}\right)} = 2\sqrt{\zeta \frac{T_c \tau_d \tau_{di}}{\tau_t}} \\ P(\zeta) &= \sqrt{\zeta \frac{T_c}{\tau_d}\left(1 - \frac{\tau_d}{\tau_i}\right)^{-1}} = \sqrt{\zeta \frac{T_c}{\tau_{di}}} \end{aligned}$$

The time constants τ_{ti} e τ_{di} are referred to the electrons in the equation 4.53 and to the holes in the equation 4.80. The output signal is the sum of the two contributes

$$V(t) = V_e(t) + V_h(t) \tag{4.82}$$

4.6.5 The double integral

As we have already said in the previous section, either electron and hole contributes are constituted of two term. The first one has not an analytical solution, so we must give a numerical approximation of its value. To do this it is important to express this double integral cleverly, to facilitate the numerical calculations. Then we can re-write the quantity

$$\int_0^{\xi} \exp\left\{-\zeta \frac{T_c}{\tau_{ti}}\right\} H\left(t-\zeta T_c\right) \\ P(\zeta)\left(\int_0^{\Theta(\zeta,t)} \exp\left\{-\vartheta^2\right\} I_1\big(P(\zeta)\vartheta\big) d\vartheta\right) d\zeta \tag{4.83}$$

as

$$\int_0^{\xi} \exp\left\{\frac{P^2(\zeta)}{4} - \zeta \frac{T_e}{\tau_{ti}}\right\} H\left(t-\zeta T_c\right) \\ \left(P(\zeta)\exp\left\{-\frac{P^2(\zeta)}{4}\right\}\int_0^{\Theta(\zeta,t)} \exp\left\{-\vartheta^2\right\} I_1\big(P(\zeta)\vartheta\big) d\vartheta\right) d\zeta \tag{4.84}$$

Indeed when $\Theta(\zeta,t) >> P(\zeta)$ the integral in the round brackets in the equation **??** converge to

$$\int_0^{\infty} \exp\left\{-\vartheta^2\right\} I_1\big(P\vartheta\big) d\vartheta = \frac{P}{4} M(1,2,\frac{P^2}{4} = \frac{\exp\left\{\frac{P^2}{4}\right\}-1}{P}$$

This result is achievable from the tabulated integral[1]

$$\int_0^{\infty} \exp\left\{-a^2t^2\right\} t^{\mu-1} J_\nu\big(bt\big) dt = \\ = \frac{\Gamma\left(\frac{\mu+\nu}{2}\right)\left(\frac{1}{2}\frac{b}{a}\right)^\nu}{2a^\mu \Gamma\left(\nu+1\right)} M\left(\frac{\mu+\nu}{2}, \nu+1, -\frac{b^2}{4a^2}\right) \\ Re(\mu+\nu) > 0 \qquad Re(a^2) > 0$$

imposing the conditions

$$a = \mu = \nu = 1 \\ b = iP$$

and exploiting the existing relation between $I_\nu(z)$ and $J_\nu(z)$

$$I_\nu(z) = i^{-\nu} J_\nu(iz)$$

[1] See *Abramowitz, Handbook of mathematical function*, relation 11.4.28 p. 486

where $J_\nu(z)$ is a Bessel function and $M(\alpha, \beta, z)$ the hypergeometric (or Kummer's) function. Thereby, on the one hand, we moderate the growth of the in bracket integral with increasing P (the in bracket quantity into the eqation 4.85 converges to 1 as we can see in figure 4.3), on the other we brake the exponential fall to zero of the first term in the external integral. In this way we facilitate the numerical integration. Unfortunately it is impossible to do better using the

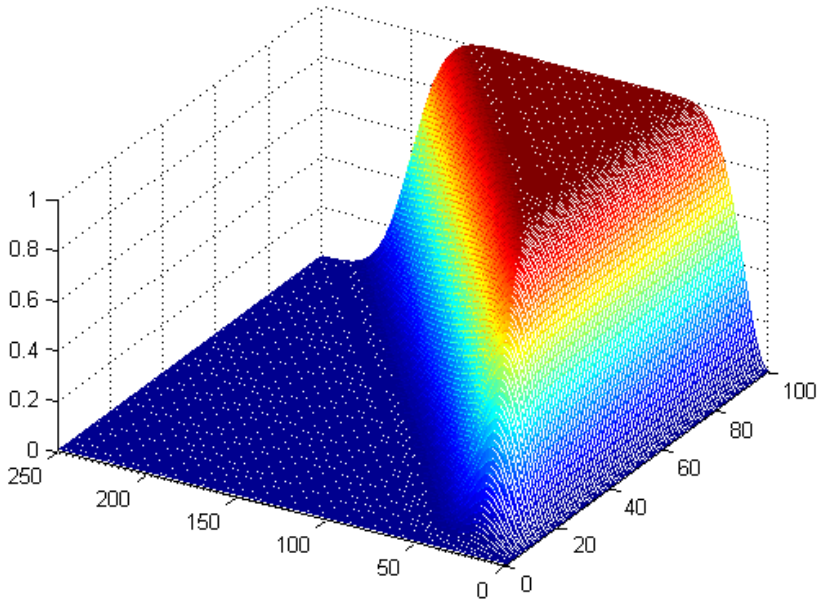

Figure 4.3: Numerical evalueation for the quantity between the round brackets in the equation 4.85

Kummer's transform

$$M(\alpha, \beta, z) = e^z M(\beta - \alpha, \beta, -z)$$

because, when applied to a Bessel function $I_\nu(z)$, Kummer's transform returns the same Bessel function with opposite argument $I_\nu(-z)$. Indeed for a Bessel function $\beta = 2\alpha$ and in particular we get[2]

$$M(\nu + \frac{1}{2}, 2\nu + 1, 2z) = \Gamma(1 + \nu)e^z(\frac{1}{2}z)^{-}\nu I_v(z) \tag{4.85}$$

[2]See*Abramowitz, Handbook of mathematical function*, relation 13.6.3 p. 509

Conclusions In this chapter we have briefly shown the fundamental results of detector and read-out electronics modelization making some hypotheses (see section 1.3.1) and under several approximation (i.e. fast carriers, slow carriers, no detrapping). We have also obtained the exact solution even in the frame of the initial Hypotheses. Works are in progress to generalize this model to the cases where different geometries or spatial charge modify the system response. Similar efforts are being made to achieve similar result for the photocurrent models.
These models could result important both to fit and understand the experimental data, obtaining also the transport parameters both for electron and hole, and to achieve a correction method for charge losses, exploiting the information about the impact depth.
In the next chapter we show the attempt to achieve a experimental test for these models.

Chapter 5

Experimental Test

In the previous chapter we have briefly exposed the mathematical model for the detector and the read-out electronic. In this chapter we show the experimental activity implemented to verify this model. This activity, that has taken a large part of the fourteen months, is not still completed and it might be worth to know some of its evolution.

5.1 Double shaping time

The first idea of correcting the signal has been taken from the "twin shaping filter"method as published in [52, 72, 73]. The twin shaping filter method is a variation of the rise time method, that employs the rise time of the electrical signal to obtain information about the z-position (depth) where the photon has been absorbed in the detector and then to correct the signal amplitude [74–76]. The fundamental idea, underlying the twin shaping filter method, is to shape the detector signal with two shaper with different time-constant, as shown in figure 5.1. The "fast"shaper should be more sensitive to the fast contribute (electrons) while the "slow"shaper should give us a larger amount of charge and then it should be less affected by the position x where the photon has been absorbed in the sensor. The ratio $R(x)$, between the fast shaper output V_f and the slow shaper output V_s, should be a function only of the position x, then we could hope to correct the slow output with a simple function (for example a linear function) of the $R(x)$ argument.
Trying to obtain this simple function (a simple function has never been found) we have developed the first model (without trapping) to correct the signal supplied by the CSP output.

5.2 Read-out electronic

The experimental activity is performed in the INAF-IASF laboratories in Bologna in collaboration with Dr. Ezio Caroli.

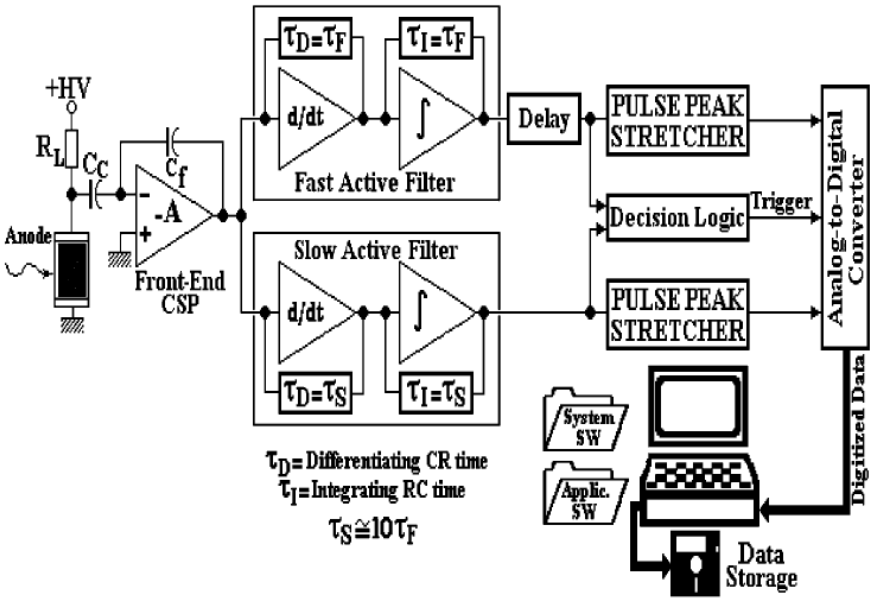

Figure 5.1: Twin shaping time method [52]

The signals are obtained irradiating the detector with X and γ-ray sources (^{57}Co, ^{109}Cd, ^{133}Ba, ^{137}Cs, ^{241}Am). The detector is housed, with the read-out electronics, in a metal box (see the figure 5.2) to shield the detector from the light sources and the electronic circuitry from the electrical disturb. The box has a window transparent to X and γ-ray to irradiate the detector. The fundamental read-out electronics can be schematically shown as in the figure 5.3. The polarization bias is supplied by an Emco DC-DC converter through the resistance R_b and the current signal, crossing the insulating capacitor C_{in}, is collected by the charge preamplifier CSP (in our case an $eV5093$ model) with a very long time constant $\tau_f = R_f C_f$ of about $1040\mu s$ to reduce the noise effects. To achieve better spectroscopic properties normally the "illuminated"electrode is grounded while a positive potential is applied to the other one. The overall circuital time constant $\tau_i = (\frac{1}{\tau_f} + \frac{1}{\tau_{in}})^-1$ takes into account also the time constant $R_{in}C_{in}$, due to the insulating capacitor C_{in} and the input resistance R_{in} (given by the parallel between the bias resistance R_b and the detector resistance), and normally it is in the order of $100 - 1000\mu s$.

5.3 Shaping electronics

To test the model regardless the read-out electronics time constant, it was necessary an electronic to re-shape the signal. Then we needed a PZC (Pole Zero

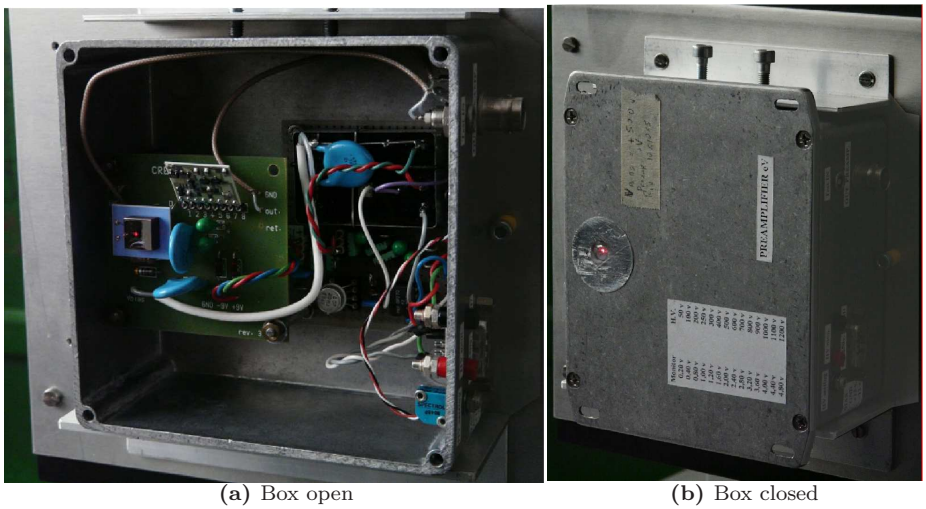

(a) Box open **(b)** Box closed

Figure 5.2: The read-out electronic in its metal box

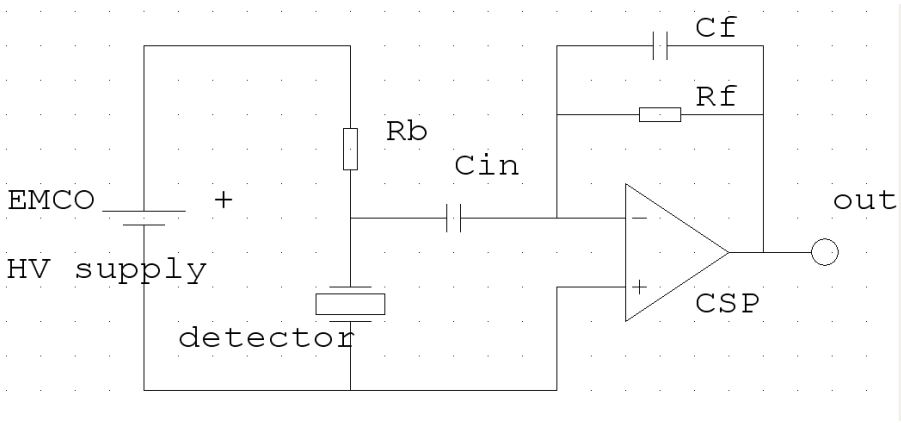

Figure 5.3: Simplified schematic for the read-out electronic

Cancellation) circuit to cancel the CSP pole, an integrator with settable time-constant, and an amplifier. All these circuits had to get a large bandwidth to achieve a good time resolution and a low noise-level because of the large bandwidth. Good time resolution (at least $10ns$) is fundamental to get an accurate information about the depth of the photon-crystal impact and then to correct the signal. For this reason the project of these circuits and the choice of each component was very accurate and we chose, between several product, low-noisy

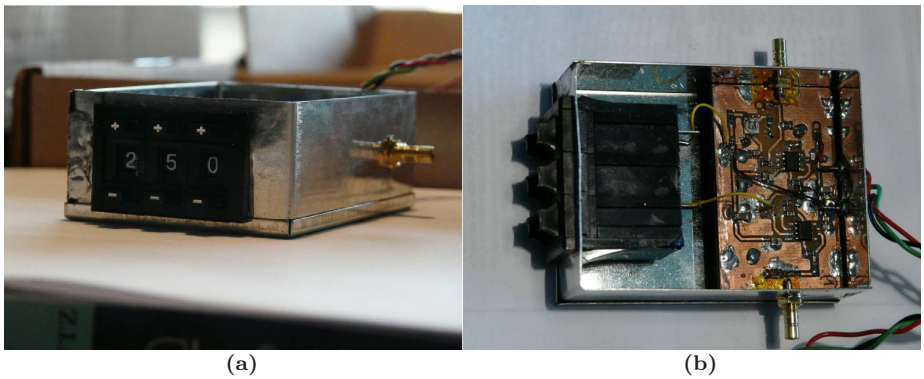

(a) (b)

Figure 5.4: Fast Integrator.

very high speed operational amplifiers as $MAX4107$, $THS3201$ and $OPA847$. In particular the $THS3201$ was chosen because of the very high stability and the very high slew rate. These two characteristics are fundamental to obtain fast integrators or PZCs.

PZC and integrator The ultra high band operational amplifier are compensated, so that they work correctly with a closed loop gain above a fixed value to reduce the bandwidth. When we project an high frequency integrator (see figure **??** in appendix B) we must consider that a capacitor in the feedback network reduce the closed loop gain at high frequency and then destabilizes the operational amplifier (OPAMP). So we need to use a different architecture (as the Deboo one) to keep constant the gain level at high frequency. Nevertheless each capacitor, connected to the input or to the output, induces some phase displacement between these pins and, then, disturbs the OPAMP correct working. For this reason at high frequency it is more difficult the creation of a good integrator and we need a very stable OPAMP as the $THS3201$, purpose-made for driver function, with high current output and very high slew rate, important features in presence of capacitive components. In the amplifier stage before the integration one we have preferred $MAX4107$ its lower noise level. In the first stage, where the signals are smaller and the slew rate constraints are more relaxed we can use this OPAMP that is less noisy.
The high slew rate and the high gain-bandwidth product are important also to ensure the PZC frequency response (see figure 5.8). In this case, at high frequency, the close loop gain increase, then high gain-bandwidth product and slew rate ensure low signal distortion and small delay, reducing the instability.

Amplifier In the amplifier stage (see figure **??** in appendix B) we have chosen the $OPA847$ because its low noise level. Moreover when the signal increases the good slew rate and gain-bandwidth product of this OPAMP ensure a good time

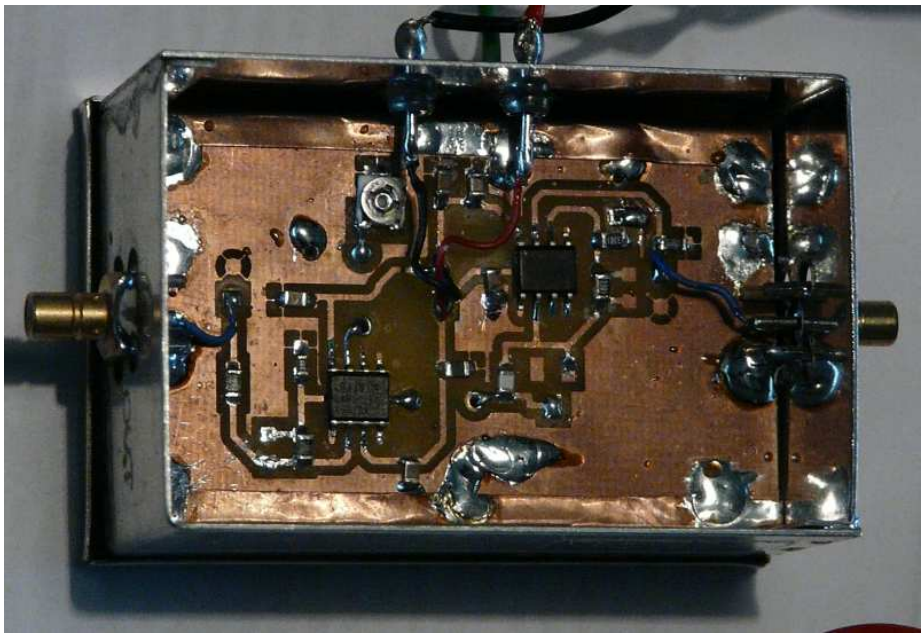

Figure 5.5: Pole Zero Cancellation circuit (PZC).

and frequency response allowing a low distorsion level.
When the DC coupling is not necessary (or is not desired) we can use monolithic AC amplifier, as $MAR8$, that increases the signal-noise ratio and simplifies the electronics. All the schematics for these circuits can be found in appendix B.

Simulation All these circuits has been simulated with $ORCAD$ and $TINA$ (two SPICE simulators) and tested showing good frequency response until $50MHz$ for the integrator, $80MHz$ for the PZC, $120MHz$ for the $20dB$ DC-coupled amplifier and $270MHz$ for the $30dB$ AC-coupled amplifier. The achievable time resolution is then of about $3ns$ (equivalent to the $50MHz$ bandwidth of the integrator). Below we report the simulations for the integrator and the PZC respectively in figure 5.7 and 5.8. Unfortunately, these electronic circuits have not still been used, because the high noise level at the CSP output causes the PZC saturation. We will discuss later the noise problem and its solution.

5.4 Data Acquisition

To test our model we must collect a large number of event to get a big enough statistic set. So we collect the signal generated by the system, constituted by the detector and the read-out electronic, in response to a photon absorbed by the detector. Each signal is digitized with a temporal resolution in the

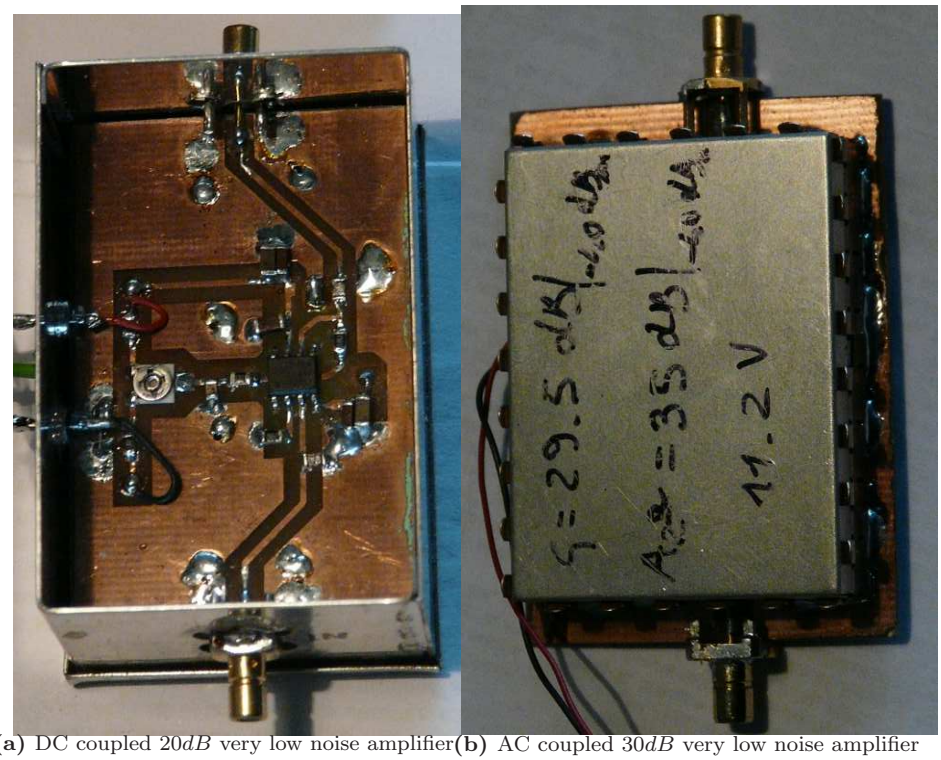

(a) DC coupled $20dB$ very low noise amplifier **(b)** AC coupled $30dB$ very low noise amplifier

Figure 5.6: Amplifiers.

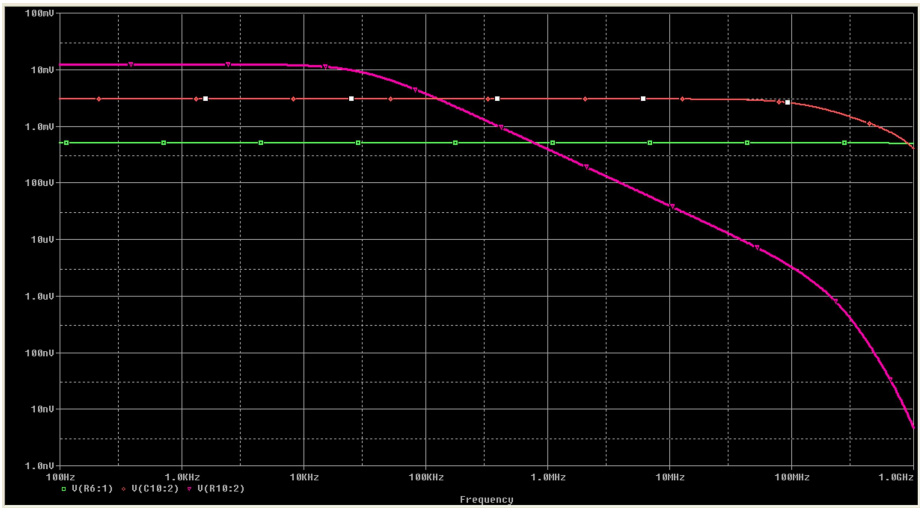

Figure 5.7: Simulation in frequency domain of the fast integrator performed with ORCAD simulator (the magenta bold curve).

range of $1 - 10ns$ for a time duration between $30\mu s$ and $80\mu s$ by means of two National-manufactured digitizer. The first is a $PXI - 5152$ $8bit$ digitizer with digitalization rate of $2GS/s$ shared among two channels, while the second is a $PXI - 5122$ $14bit$ digitizer with digitalization rate of $200MS/s$ (even shared among the two channels).

Digitalization and high frequency noise reduction The digitalization is managed by an acquisition program, developed with the Labview programming language (Labview is a graphical programming environment and the acquisition program is visible in the appendix C). In this program we can set a threshold for the trigger, the digitalization rate, the temporal duration of each digitalization, the number of event fetched and several other parameters. In this program we have also inserted a settable digital filter to reduce the noise. The noise has been also reduced improving the mass connection and the shielding, and using battery power supply (filtered by means of ferrite-rings). In the figure **??** we can see noise reduction after these technical solutions. It is possible to reduce the noise also with an over-sampling. If we sample the system at $1GS/s$ and we save on the mean taken on 10 digitized data, we can reduce the high frequency noise reducing the temporal resolution to $10ns$.

Collimator An other important improvement in the last measures is the beam focusing. In the first measures the radioactive sources were not focused. Because of the transport properties could vary in the detector volume, we have focused the photon beam to reduce the irradiated detector area.

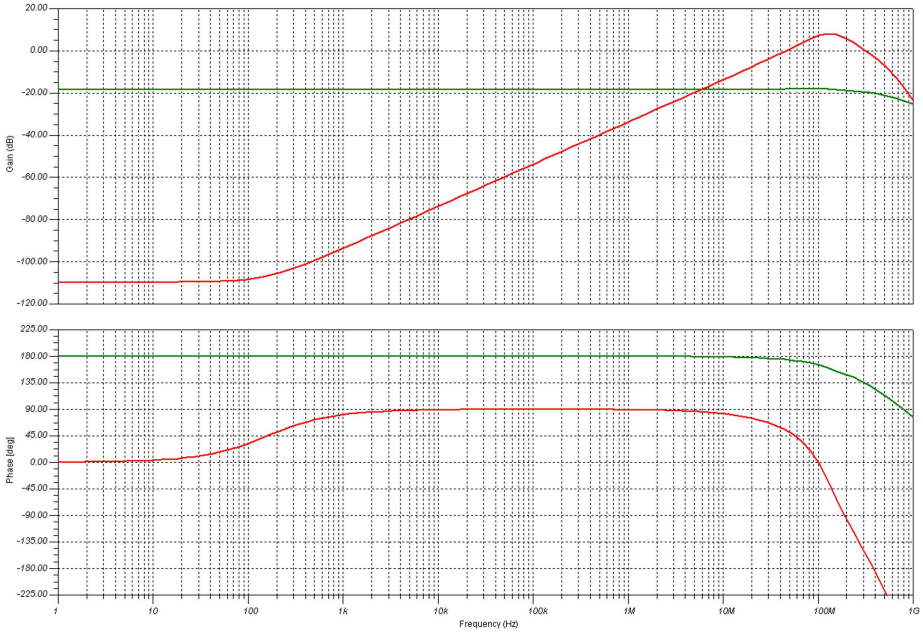

Figure 5.8: Simulation in frequency domain of the Pole Zero Cancellation circuit (PZC) performed with TINA simulatore (the red curves). Above we have the frequency response, below the phase (with respect the input) diagram.

In figure 5.10 it is possible to see the collimation system constituted by a tungsten shield with a $0.5 \times 1mm$ slit to irradiate the detector. To center the detector we use a solid state laser placed instead of the source and we move the detector by means of micro-metric movements. In figure 5.11 we can see the laser spot on the detector. Measurements with very thin beam (in the order of $10\mu m$) have been taken at the ESRF institute (Grenoble). Unfortunately because of the length of the BNC cable (the digitizer was outside the room where is located the sample) the data are affected by low frequency noise, as we can see in figure**??**.

5.5 Data analysis and fitting

5.5.1 Signal correction

Once we have acquired the signals, we have to analyze these data. The fundamental idea was to analyze the data, extract the transport parameters, and

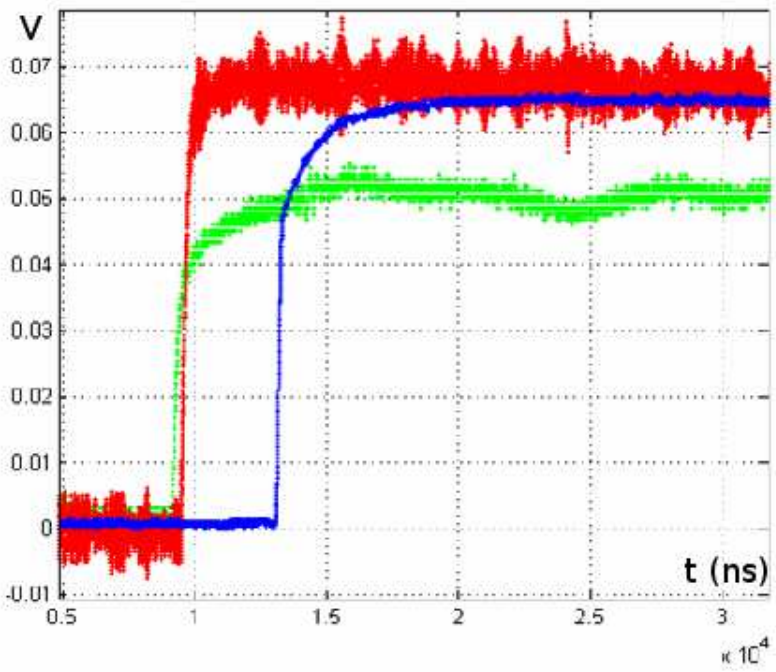

Figure 5.9: The fist data acquired in red, in green the data acquired at the ESRF institute, and in blue the last data taken after the noise reduction.

calculate the collection efficiency defined as:

$$\begin{aligned} \eta(\xi) &= \frac{Q_M(\xi)}{Q_0} = \frac{Q_0 F(\xi, t_M(\xi))}{Q_0} \\ &= F(\xi, t_M(\xi)) = F_M(\xi) \end{aligned} \tag{5.1}$$

where $\xi = x/L$ is the relative impact depth and $Q_M(\xi)$ the maximum of the collected charge, $t_M(\xi)$ the time when the maximum occurs, and $F(\xi, t_M(\xi)) = F_M(\xi)$ the maximum of the collection efficiency function $F(\xi, t)$ calculated in the modelization. Finally, after these steps, we colud correct the charge collected.
At the beginning, in the "Hecht case"(no detrapping), as we can see in the appendix A, we have calculated when the maximum of collected charge occurs in relation to the transport properties. With these values for the transport properties, we have calculated the maximum of the collection efficiency $F_M(\xi)$.
When the model is become more complex, with the detrapping mathematical discussion, the idea has always remained the same, with some more complications.

Figure 5.10: Collimator. In figure we can see the laser spot coming out from the slit

5.5.2 Fitting

The fundamental problem in the fitting procedure is that we must fit concurrently all the collected data. The model indeed depends on two kind of parameters:

- The first kind of parameters concerns the singular events. This parameters are, for example, the amplitude A and the impact depth x_0. Moreover other individual parameters are needed to fit the data as the CSP offset of and the time when the photon is absorbed t_0. Because these parameters (A, x_0, of, t_0) are related to the singular event, we have four parameters for each singular collected event, so the number of parameters should be multiplied by the number of events.

- the second kind of parameters is general and concerns the material transport properties (i.e. the crossing time T related to mobility μ, the lifetime τ_t, and the detrapping time τ_d both for electrons and holes) or the electronic characteristics (the integration time τ_i).

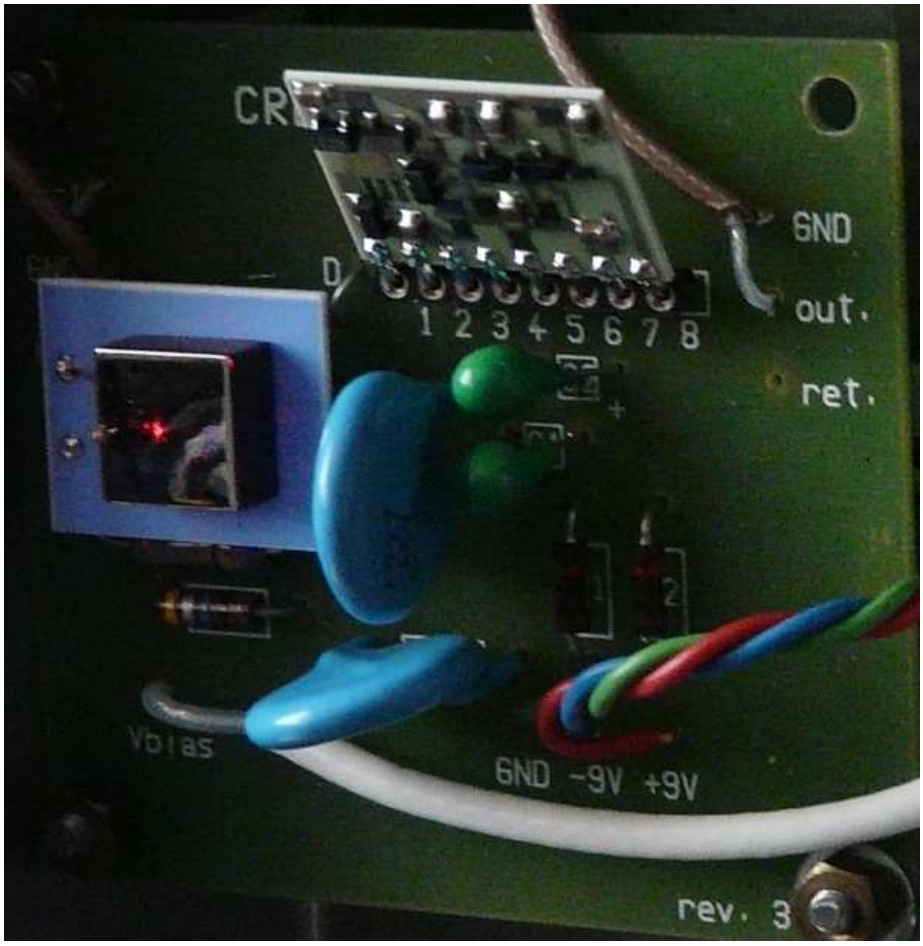

Figure 5.11: Centering with laser beam.

The first set of parameters should be determined by means of singular fits, one for each event; the second set should be determined with an overall fitting procedure (global fit). The problems are two:

- the two set of parameters are mutual dependent.
- A large computational power (and time) is required.

Now we face this two problems.

Fitting procedure To choose the starting values for the fitting parameters we initially do a singular fit for each of the N event. In this way we get $N\times(A,\ x_0,\ of,\ t_0)$ singular parameters and $N \times (T_e, T_h, \tau_{te}, \tau_{th}, \tau_{de}, \tau_{dh})$ global parameters

while τ_i is fixed because its value is yet known. The first group is the starting parameter set used for each singular fit. To choose the starting parameters for the global fitting procedure, instead, we take the mean-value of each group.
Once given the initial parameters, the fitting procedure follows an iterative method in two step:

- In the first step we fix all the individual parameters for each event and we search the global parameters that minimize the global "chi-square" χ^2_G.
- In the second step we fix the global parameters and we search, event by event, the new individual parameter set that minimizes each singular chi-square χ^2_S.

This procedure is iterated until the global chi-square convergence. Indeed, because the singular and the global parameter sets depend on each other, the procedure normally converges to the minimum value for the global chi-square.
To fit the data we exploit the *fminuit* matlab function[1] Using this function we can fix or release parameters and this is very useful because some parameters, as of or t_0, are weakly dependent on the other ones, so, once found them in the first step, they can be fixed forever to simplify the further minimization. We can also set the range where a parameter can be varied (when we know this range), to speed up the convergence and avoid false minima

Computational expedients Because of the number of events fitted N is in the order of 1000, the calculation efficiency is very important. Initially, the most of the computational resources was used to calculate numerically the double integral expressed in the equation 4.85. This double integral must be recalculated every time a parameter have been varied, and, more again, it must be calculated for each value of the discrete time t (about 5000). At the beginning the time employed to calculate this 5000 values was about 62.5 seconds. Now the same calculation is completed in 0.025 second.
The inner integral in the equation 4.85, that we will call $BGI(P, \Theta)$ (i.e. Bessel-Gauss Integral), depends on the two parameters $P(\xi)$ and $\Theta(\xi, t)$, so that we can avoid to recalculate always the same integral. Indeed, if we calculate this integral on a grid of 250×100 (P_i, Θ_j) points, every time we need the $BGI(x, y)$ value we can interpolate the values in the grid without recalculate every time the same integral. Only with this ploy we have reduced the calculation time of a factor 2500.
Other solutions, employed to increase the calculation efficiency, is to use vectorial integration routines (as $QUADV$ matlab function), to avoid useless or redundant operation, to reduce the required numerical precision (from $1E^{-6}$ to in $1E^{-4}$), to reduce the number of calls at the same routine (for example the integration for the electron and the hole contribution are carried out in the same call), and to use smooth functions in the integration process. Concerning

[1] fminuit is the matlab call for the *minuit* DLL, a function to search the function minima developed at the CERN institute. Fminuit has been created by Dr. Giuseppe Allodi.

this last point, the tabulated values, used to calculate the double integral in eq. 4.85, are not the $BGI(P,\Theta)$ values, but the $BGEP(P,\Theta)$ values, where $BGEP$ is the quantity in the round brackets in eq. 4.85. This last function is a smooth function (as we can see in figure 4.3) so it makes easier the integral convergence. In this way, with all these stratagems, the overall time reduction is estimated greater than 10000 times. Nevertheless for a set of 1000 events the calculation time on my double processor PC is in the order of one month.

5.6 Experimental activity and perspectives

Figure 5.12: System for collimation and centering and the read-out electronic box.

The first measures were taken over one year ago (after we had developed the shaping electronics and the acquisition program). Having developed the first version of the fitting program, it was clear, despite the noise, that the model without detrapping was inadequate. So I developed a new model (see the previous chapter) to include the detrapping phenomena. Afterward, we have

taken other data at the INAF-IASF institute and in September we went to ESRF institute to take the first collimated measures. Next we have developed the final version for the fitting program.
All this measures, taken up to september, were noisy, as we can see in figure **??**; so in the following period we have worked to reduce the noise level until the end of December, when we achieved relatively good measures. This last measures are taken with the collimator (figure **??**). Still remains low frequency noise due

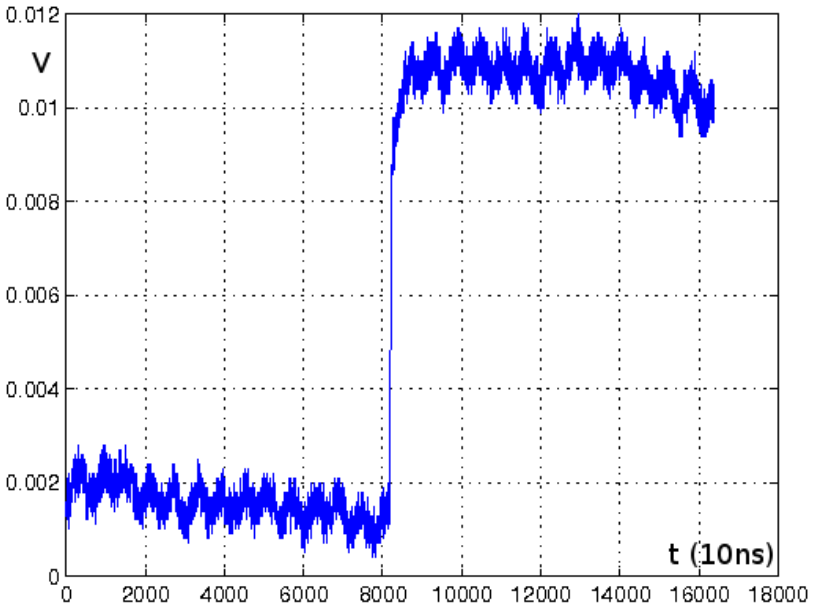

Figure 5.13: Low frequency noise overlapped on a signal taken with a ^{57}Co source. The signal is due to a $122keV$ photon absorption.

to the high voltage DC-DC converter that, as we can see in figure 5.13, disturb especially with low energy X-ray.
The measures with low energy X-ray are very important; indeed, because of the tiny penetration length of this radiation, we can select only a kind of carrier, either electrons or holes, and then separate the fitting and fix to zero the depth parameter ξ. In this way we halve the free parameters in the global fit as well as in the singular fits: so the fitting procedure is really simplified.

New Read-out electronics To do these measures it is needed to provide for a settable generator to supply both positive and negative HV-power, and also dump down the noise, shielding and filtering the HV-generator. Our present

system provides only positive bias (with respect the mass pin) so that, with low energy X-ray, we can only detect the electron component (the illuminated pin is the grounded one). Moreover the low frequency noise affect this measures as we can see in the figure 5.13 above. We are working to achieve a new system, with lower noise and also settable power polarity (now we can set only the tension value, not the polarity).

Experimental analysis For these reasons, up till now, we have fitted only some old measures. To achieve a good enough signal to noise ratio this data have been taken with ^{57}Co and ^{137}Cs sources and digitized at $1GS/s$ rate. Then these data have been filtered with a decimation process, taking, as experimental data, the mean value of 10 contiguous data. The experimental analyses show a

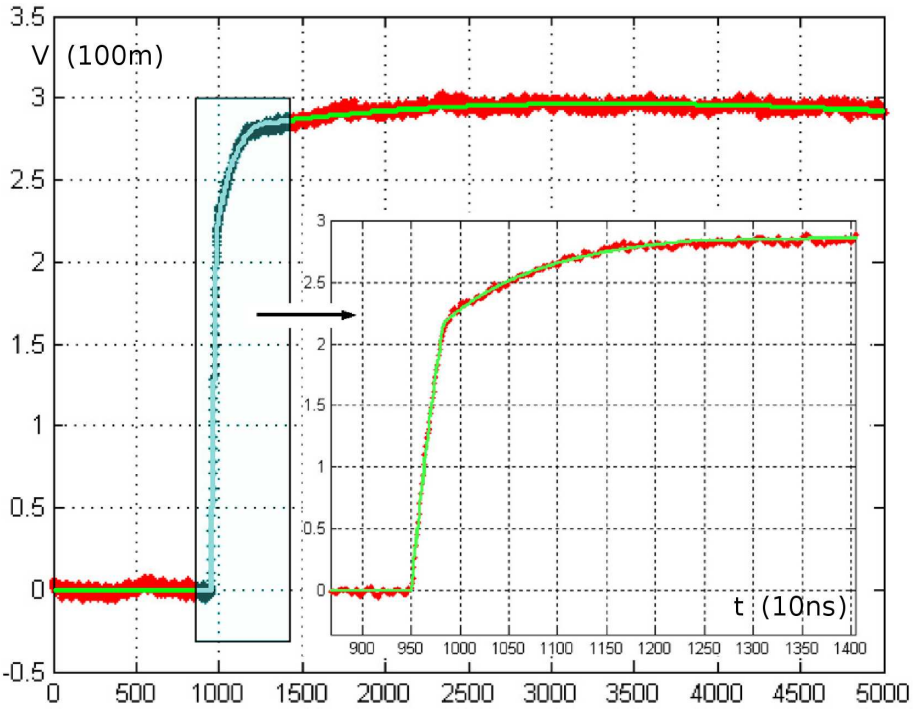

Figure 5.14: Fitting of an high energy absorption event (good signal to noise ratio). In the x-axis we have the time (one step for $10ns$), in the y-axis we have the signal (the unity step corresponds to $100mV$).

good agreement between the data and the model, when we fit the data, event by event, with all the parameters free as we can see in figure 5.14 above (we obtain singular chi-squares near one[2]). In this case the spread of the amplitude

[2]As error value used to calculate the chi-square is taken the standard deviation of the signal before the photon absorption and then the signal generation

parameter A is the same of the one obtained with a traditional multichannel.
When we have applied the global fit to achieve the global parameters concerning the material transport properties, we have got a worse fit quality. But, if we shrink the range of variability for the T_e value[3] in the fitting procedure, against a chi-square worsening, we achieve an improvement in the spectroscopy results with a line shrinkage from 6% to 4% for the ^{57}Co source.
The worsening of the chi-square could be due to the non collimated photon beam, because the transport properties and also the field could vary moving across the detector volume. Another reason could be that this preliminary fit has been made with an approximated model, where the trapping (and the detrapping) has been considered concerning the fast carriers as in the sections 3.5.3 and 3.6.2.

Definitive test To achieve a definitive experimental test we need the new system, to measure separately the electron behavior and hole one with low energy X-ray and extract the relative transport parameters. Indeed, when we fit an high energy X or γ-ray, the functional model depend on, at least 8 physical parameters: the amplitude A and the photon-crystal impact depth x_0, and the material transport properties described by other six parameters $T_e, T_h, \tau_{te}, \tau_{th}, \tau_{de}, \tau_{dh}$. In this way, each singular fit depends on two parameter and the global fit on six parameter. If we use low energy X-ray, because of the tiny penetration length, we can fix the parameter X_0 to 0 and then only a single kind of carrier is involved in the transport phenomena (electrons or holes depending on the bias polarity). In this way, we can study separately the electron and the hole transport and, as already said above, we halve the number of free parameters required for each fitting procedure. This is very important because makes more significant the fitting result (the fitting are performed with half the number of parameters) and, moreover, we think it could diminish the computational time of at least one order of magnitude (some day against one month). Once we give this parameter we will try to correct peaks at higher energy (with singular fits depending only on two parameters). Meanwhile, we are working on the new read-out electronic.

Conclusions and perspectives In this last years great effort has been spent to achieve good material with excellent transport properties. The ternary alloys, as CZT, while have shown interesting properties as radiation detector, on the other hand show transport properties still far from their theoretical limit. For this reason it could be interesting to find a correction method for the charge losses.
After the experimental tests, it is our intention to generalize this model for detector with different geometries (as pixellated or strip detector) and with different profiles of internal electric field, and finally create a real time electronic,

[3] T_e is connected to the μ_e value by means the relation 5.6b

FPGA[4] based, to correct the signal. This model could also represent a good starting point to interpret the data of the pulsed photocurrent.

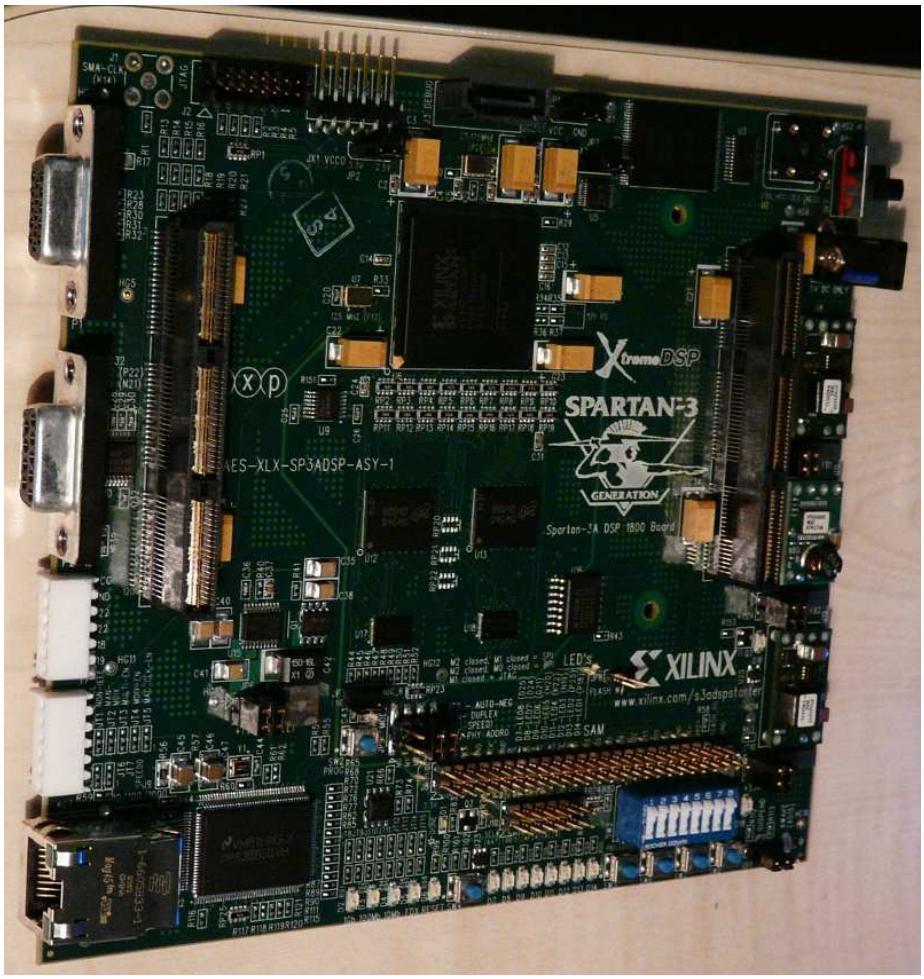

Figure 5.15: FPGA board SPARTAN 3A-DSP.

[4]Field Programmable Gate Array (in figure 5.15) are very versatile logic programmable cips. They are most used also for Digital Signal Processing (DSP) and as trigger logic.

Appendix A

Mathematical complements

Let's handle the problem from another point of view. We can consider system, constituted by the sensor and the preamplifier as two parallel current generators that inject current in a parallel RC (as shown in the figure A.1). Starting from $t_i = 0$ each of the two generators creates a signal in current that decays exponentially until the time $t_f = (1 - \xi)T_e$ in the electronic case and $t_f = \xi T_h$ in the hole case and then it turn off.

In this way we face the problem not from a general point of view but considering it as a separate problem, modelizable in the above mentioned way. Obviously the same solution that we will obtain for the currents is also directly derivable from the model described in the chapter 3 (the Hecht case), taking the derivative of the expression of the $Q(t)$, nonetheless this particular approach is interesting too, closing the loop by showing the problem from a different and more intuitive angle of view.

The problem can be solved appealing the superposition principle, since the circuit is linear. For this reason we will develop the calculation not expliciting, as far as possible, the kind of carrier involved. Let us assume we have a simple current generator supplying the signal

$$\begin{cases} I(t) = I_0 \cdot e^{-\frac{t}{\tau_c}} & t \in (0, t_f) \\ I(t) = 0 & t \notin (0, t_f) \end{cases} \tag{A.1}$$

The differential equation that describes the system can be obtained by imposing the same drop across both the two impedances and that the algebraic sum of the currents flowing in the two circuit branches is equal to the current supplied by the generator. In this way we obtain the system

$$\begin{cases} R \cdot I_r(t) = V_r = \frac{Q_c(t)}{C} = \frac{\int_0^t I_c(\theta) d\theta}{C} \\ I_c + I_r = I(t) = I_0 \cdot e^{-\frac{t}{\tau_c}} \end{cases} \tag{A.2}$$

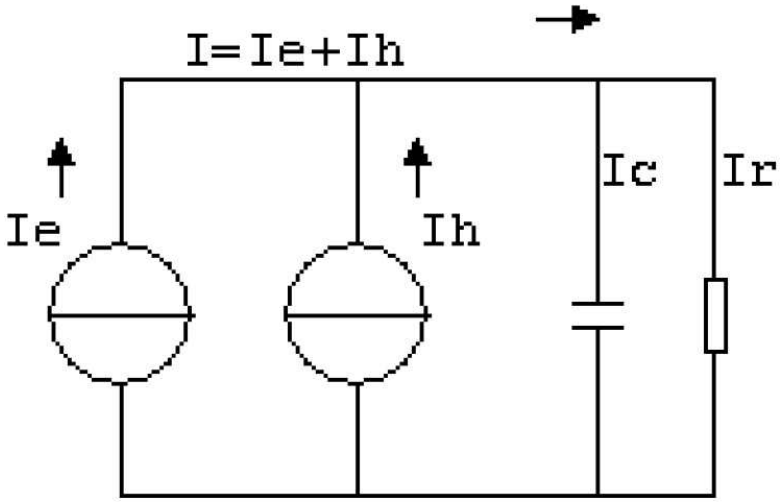

Figure A.1: Equivalent schematic for the system constituted by sensor and preamplifier with the two current contributions (for both electron and hole cases)

or also

$$\begin{cases} I_c = \frac{dQ_c(t)}{dt} = RC\frac{dI_r}{dt} \\ I_c + I_r = I(t) = I_0 \cdot e^{-\frac{t}{\tau_c}} \end{cases} \tag{A.3}$$

from which

$$RC\frac{dI_r}{dt} + I_r = I(t) = I_0 e^{-\frac{t}{\tau}} \tag{A.4}$$

The solution for this type of equation can be obtained applying the "*variation of parameters*"method. First, the solution of the equation of the associated homogeneous is given by

$$\widetilde{I}_r e^{-\frac{t}{RC}} \tag{A.5}$$

If we now consider $\widetilde{I}_r = \widetilde{I}_r(t)$ and we replace in the complete differential equation, we find a solution in the form

$$I_r(t) = I_r e^{-\frac{t}{\tau_c}} = \frac{I_0\tau_c}{\tau_c - \tau_f} e^{-\frac{t}{\tau_c}} + I_1 e^{-\frac{t}{\tau_f}} \tag{A.6}$$

with $\tau_f = RC$.
By imposing the condition $I_r(0) = 0$ we obtain

$$I_1 = -\frac{I_0\tau_c}{\tau_c - \tau_f} \tag{A.7}$$

from which

$$\begin{cases} I_r = \frac{I_0\tau_c}{\tau_c-\tau_f}\left[e^{-\frac{t}{\tau_c}} - e^{-\frac{t}{\tau_f}}\right] \\ I_c = \tau_f \frac{dI_r}{dt} = \frac{I_0\tau_c\tau_f}{\tau_c-\tau_f}\left[\frac{e^{-\frac{t}{\tau_f}}}{\tau_f} - \frac{e^{-\frac{t}{\tau_c}}}{\tau_c}\right] \\ Q_c(t) = \tau_f I_r(t) = \frac{I_0\tau_c\tau_f}{\tau_c-\tau_f}\left[e^{-\frac{t}{\tau_c}} - e^{-\frac{t}{\tau_f}}\right] \end{cases} \tag{A.8}$$

All this is true in the range $(0, t_f)$.

If now we are interested in the maximum value of the charge integrated on the capacitor, it's clear that we have to calculate the value of the $Q_c(t_M)$ where t_M represents the time at which this charge reaches the maximum: Then t_M can be obtained by imposing $I_c(t) = 0$. By imposing this condition we obtain:

$$\tau_c e^{-\frac{t}{\tau_f}} - \tau_f e^{-\frac{t}{\tau_c}} = 0 \tag{A.9}$$

Solving this equation we gain the solution

$$\begin{cases} t_M = \frac{\tau_c\tau_f}{\tau_c-\tau_f} ln(\frac{\tau_c}{\tau_f}) = \tau_{ef}^c ln(\frac{\tau_c}{\tau_f}) \\ Q_M = Q(t_M) = I_0\tau_c e^{-\frac{\tau_c}{\tau_c-\tau_f} ln(\frac{\tau_c}{\tau_f})} \end{cases} \tag{A.10}$$

with evident meaning for τ_{ef}^c. Otherwise, defining $1 + x = \tau_f/\tau_c$, also

$$\begin{cases} t_M = \tau_f \frac{ln(1+x)}{x} \\ Q_M = Q(t_M) = I_0\tau_c e^{-\frac{1+x}{x} ln(1+x)} \end{cases} \tag{A.11}$$

which clearly is valid only if

$$t_f > t_M > 0 \tag{A.12}$$

The solution for the current I_c for $t \geq t_f$ can be obtained too by taking the derivative of the capacitor charge.

$$I_c = I_{0c}\tau_{ef}^c\left[e^{\frac{t_f}{\tau_{ef}^c}} - 1\right] \cdot \frac{\partial}{\partial t} e^{-\frac{t}{\tau_f}} = I_{0c}\frac{\tau_{ef}^c}{\tau_f}\left[1 - e^{\frac{t_f}{\tau_{ef}^c}}\right] e^{-\frac{t}{\tau_f}} \tag{A.13}$$

Now in this region since there is no further contribution coming from the generator, we have that

$$I_c = -I_r < 0 \tag{A.14}$$

So, if there is a maximum in this region, it must coincide with t_f that is $t_M = t_f$, because

$$t_M = \tau_f \frac{ln(1+x)}{x} \geq t_f \tag{A.15}$$

A.1 The two components

So far we have addressed the problem according to the roman philosophy "*divide et imperat*", considering just a single contribution. What happens if we now consider that the current is composed of two contributions, the electronic and the hole one?

First of all, declining what has already been obtained for two contributions, here are the key results:

- in the electronic case

$$\begin{cases} I_{ce} = \tau_f \frac{dI_{re}}{dt} = I_{0e}\tau^e_{ef}\left[\frac{e^{-\frac{t}{\tau_f}}}{\tau_f} - \frac{e^{-\frac{t}{\tau_e}}}{\tau_e}\right] \\ \\ t_{Me} = \tau^e_{ef} ln(\frac{\tau_e}{\tau_f}) \\ \\ Q_{Me} = Q(t_{Me}) = I_0\tau_e e^{-\frac{\tau_e}{\tau_e-\tau_f}ln(\frac{\tau_e}{\tau_f})} \end{cases} \tag{A.16}$$

  in the range:

$$t_{fe}(\xi) = (1-\xi)T_e > t_{Me} > 0 \tag{A.17}$$

  while outside (but always with $t > 0$)

$$I_{ce} = I_{0e}\frac{\tau^e_{ef}}{\tau_f}\left[1 - e^{\frac{(1-\xi)T_e}{\tau^e_{ef}}}\right]e^{-\frac{t}{\tau_f}} \tag{A.18}$$

  where

$$\tau^e_{ef} = \frac{\tau_e\tau_f}{\tau_e - \tau_f} \tag{A.19}$$

- and similarly for the hole case

$$\begin{cases} I_{ch} = \tau_f \frac{dI_{rh}}{dt} = I_{0h}\tau^h_{ef}\left[\frac{e^{-\frac{t}{\tau_f}}}{\tau_f} - \frac{e^{-\frac{t}{\tau_h}}}{\tau_h}\right] \\ \\ t_{Mh} = \tau^h_{ef} ln(\frac{\tau_h}{\tau_f}) \\ \\ Q_{Mh} = Q(t_{Mh}) = I_0\tau_h e^{-\frac{\tau_h}{\tau_h-\tau_f}ln(\frac{\tau_h}{\tau_f})} \end{cases} \tag{A.20}$$

  in the range:

$$t_{fh}(\xi) = \xi T_h > t_{Mh} > 0 \tag{A.21}$$

  while outside this range (but always for positive t)

$$I_{ch} = I_{0h}\frac{\tau^h_{ef}}{\tau_f}\left[1 - e^{\frac{\xi T_h}{\tau^h_{ef}}}\right]e^{-\frac{t}{\tau_f}} \tag{A.22}$$

where

$$\tau_{ef}^{h} = \frac{\tau_h \tau_f}{\tau_h - \tau_f} \tag{A.23}$$

The fundamental matter concerning the two contribution overlap is the timing of the maximum respect to the system characteristic times. Indeed it is possible to define four temporal regions (see figure A.2):

1. $t \in [0, min\{(1-\xi)T_e, \xi T_h\})$ region 1
2. $t \in [min\{(1-\xi)T_e, \xi T_h\}, max\{(1-\xi)T_e, \xi T_h\}]$ regions 2 and 3 depending on whether the relations are respectively:

$$(1-\xi)T_e > \xi T_h$$

$$\xi T_h \geq (1-\xi)T_e$$

   respectively.
3. $t \in (max\{(1-\xi)T_e, \xi T_h\}, \infty)$ region 4

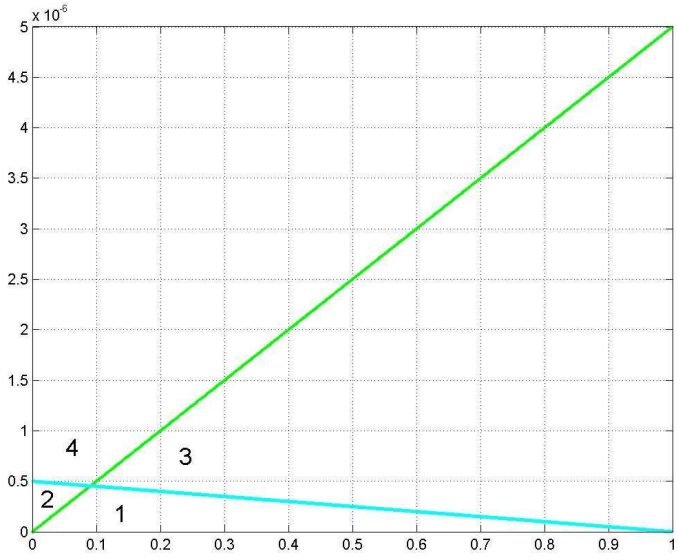

Figure A.2: The different regions are bounded by the intersections of the lines. The green line represents the time required by the holes to reach the negative electrode, the cyan line is related to electrons. The x-axis indicate the relative depth, while the y-axis indicates the time in seconds

It's important to make some fundamental considerations:

- In the first region, if the maximum exists, its time value (where it occurs) can not be calculated analytically but only numerically, and it is also independent of the relative depth ξ because, as we shall see, this does not enter as a variable in the calculation.
- In the regions two and three, the temporal point of maximum can be obtained analytically and is dependent of ξ
- In the last region, the current I_c is always negative, then the maximum cannot exist into this region, but only on the boundaries of the same (i.e. in coincidence with the beginning of the range).

Now we will calculate this maximum in different regions we have highlighted

A.1.1 Region 1

The region 1 is characterized by the fact that:

$$t \in [0, min\{(1-\xi)T_e, \xi T_h\}) \tag{A.24}$$

So the total current expression (sum of two contributions, electronic and hole) is given by the expression

$$I_c = I_{ce}(t) + I_{ch}(t) =$$

$$= Q_0 \left\{ \frac{\tau_{ef}^e}{Te} \left[\frac{e^{-\frac{t}{\tau_f}}}{\tau_f} - \frac{e^{-\frac{t}{\tau_e}}}{\tau_e} \right] + \frac{\tau_{ef}^h}{T_h} \left[\frac{e^{-\frac{t}{\tau_f}}}{\tau_f} - \frac{e^{-\frac{t}{\tau_h}}}{\tau_h} \right] \right\} = \tag{A.25}$$

$$= \frac{Q_0}{\tau_f} \left\{ \frac{\tau_{ef}^e}{Te} \left[1 - \frac{\tau_f}{\tau_e} e^{-\frac{t}{\tau_{ef}^e}} \right] + \frac{\tau_{ef}^h}{T_h} \left[1 - \frac{\tau_f}{\tau_h} e^{-\frac{t}{\tau_{ef}^h}} \right] \right\} \cdot e^{\frac{-t}{\tau_f}}$$

In order to obtain t_M we have to impose $I_c = 0$ (and the result, to be valid, must satisfy the condition A.24). In this situation, the t_M value cannot be calculated analytically and it is independent of ξ, since this latter variable does not appear in the equation.

A.1.2 Region 2

In the region 2 we get

$$(1-\xi)T_e > t \geq \xi T_h \tag{A.26}$$

otherwise

$$\xi < \frac{T_e}{T_e + T_h} = \xi_0 \tag{A.27}$$

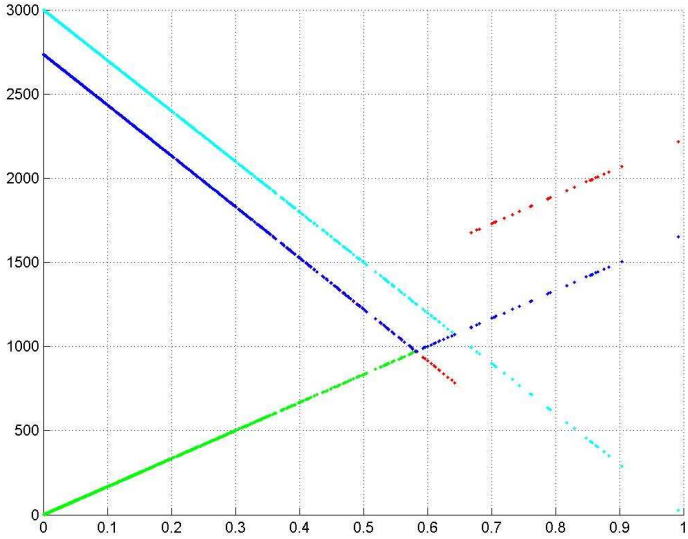

Figure A.3: In this figure, in addition to the lines of the previous figure, it appears the red broken curve that it represents the T_M calculated for the region 2 and 3. However the mathematical solution for the region 3 is is not still valid because it falls outside of this region. As shown, the T_m measured (in blue) is perfectly overlapped to the red curve in the region 2, until it crosses the green one. Hereafter t_M follow, the green line.

so the total current follows the expression

$$I_c = I_{ce}(t) + I_{ch}(t,\xi) =$$

$$= \frac{Q_0}{\tau_f}\left\{\frac{\tau^e_{ef}}{Te}\left[1-\frac{\tau_f}{\tau_e}e^{\frac{t}{\tau^e_{ef}}}\right]+\frac{\tau^h_{ef}}{T_h}\left[1-e^{\frac{\xi T_h}{\tau^h_{ef}}}\right]\right\}\cdot e^{\frac{-t}{\tau_f}} \tag{A.28}$$

Imposing $I_c = 0$ t_M becomes:

$$t_M = \theta_{C2} = \tau^e_{ef} ln\left\{\frac{\tau_e}{\tau_f}\left[1+\frac{T_e\tau^h_{ef}}{T_h\tau^e_{ef}}\left(1-e^{\frac{\xi T_h}{\tau^h_{ef}}}\right)\right]\right\} \tag{A.29}$$

And inverting the relation we get

$$\xi = \frac{\tau^h_{ef}}{T_h} ln\left\{1+\frac{T_h\tau^e_{ef}}{T_e\tau^h_{ef}}\left[1-\frac{\tau_f}{\tau_e}e^{\frac{t_M}{\tau^h_{ef}}}\right]\right\} \tag{A.30}$$

Clearly, in order that both the last solutions will be valid, it is necessary that the T_m satisfies the equation A.26. Otherwise, what physically happens (in

this second region) is that the current presents a discontinuity for $t = \xi T_h$. In correspondence to this discontinuity, the current changes sign, from positive to negative, so that $t_M = \xi T_h$ (and then $\xi = \frac{t_M}{T_h}$).

A.1.3 Region 3

the region 3 is characterized by the condition:

$$\xi T_h > t \geq (1-\xi)T_e \tag{A.31}$$

from which

$$\xi > \frac{T_e}{T_e + T_h} = \xi_0 \tag{A.32}$$

The expression of the current in this case is obtain by:

$$I_c = I_{ce}(t,\xi) + I_{ch}(t) =$$

$$= \frac{Q_0}{\tau_f}\left\{\frac{\tau^e_{ef}}{Te}\left[1 - e^{\frac{(1-\xi)T_e}{\tau^e_{ef}}}\right] + \frac{\tau^h_{ef}}{T_h}\left[1 - \frac{\tau_f}{\tau_h}e^{\frac{t}{\tau^e_{ef}}}\right]\right\} \cdot e^{\frac{-t}{\tau_f}} \tag{A.33}$$

Imposing once again $Ic = 0$ we get T_M that, as long as it remain in the validity domain (expressed by the relation [ref]), assumes the value

$$t_M = \theta_{C3} = \tau^h_{ef} ln\left\{\frac{\tau_h}{\tau_f}\left[1 + \frac{T_h\tau^e_{ef}}{T_e\tau^h_{ef}}\left(1 - e^{\frac{(1-\xi)T_e}{\tau^h_{ef}}}\right)\right]\right\} \tag{A.34}$$

Once inverted the relation, it is possible to obtain the expression

$$\xi = 1 - \frac{\tau^e_{ef}}{T_e} ln\left\{1 + \frac{T_e\tau^h_{ef}}{T_h\tau^e_{ef}}\left[1 - \frac{\tau_f}{\tau_h}e^{\frac{t_M}{\tau^h_{ef}}}\right]\right\} \tag{A.35}$$

So that both the last equations would have a physical meaning, T_m must belong to the interval expressed by the relation A.31. Where else, the current will present a discontinuity for $t = (1-\xi)T_e$ and here the maximum of collected charge is reached, so that $T_m = (1-\xi)T_e$ and $\xi = 1 - \frac{T_m}{T_e}$.

A.1.4 Region 4

Concerning the region 4, if the maximum exists, it occurs to

$$t = (1-\xi)T_e \tag{A.36}$$

or

$$t = \xi T_h \tag{A.37}$$

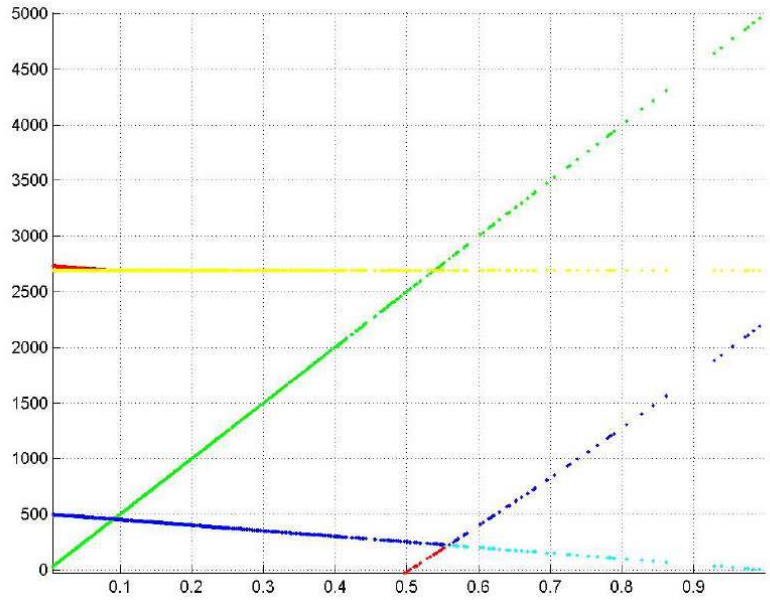

Figure A.4: This figure is similar to the previous one, where, in this case, the red curve represents a valid solution, just in region 3, where actually, the theoretical value calculated and the one detected (in blue) coincide. The yellow curve represents the solution in region 1, solution that it is not acceptable (in fact it does not intersect the region)

depending on it occurs respectively

$$\xi > \frac{T_e}{T_e + T_h} = \xi_0 \tag{A.38}$$

or

$$\xi \leq \frac{T_e}{T_e + T_h} = \xi_0 \tag{A.39}$$

So that in these cases the maximum will be located on the region boundary.

A.2 A special case

To express the collected charge, both for the electron component and the hole one, are decisive, respectively, the coefficients τ^e_{ef}/T_e and τ^h_{ef}/T_h. These coefficients determine the order of magnitude for the collected charge (and so the efficiency, defined as the ratio between the collected and the generated charge). It is interesting to observe a particular case, when it happens

$$\tau^e_{ef}/T_e = \tau^h_{ef}/T_h \tag{A.40}$$

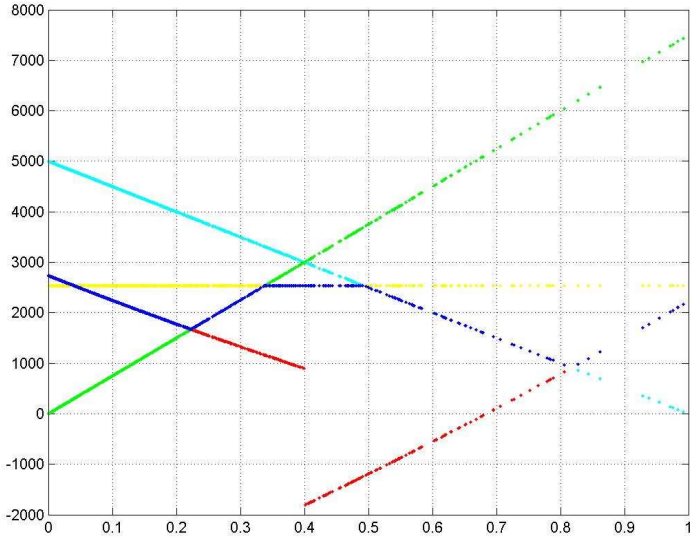

Figure A.5: In this figure it is shown how the solution for t_M behaves in the various interested regions, included region 1 (yellow curve)

Now the generic τ_{ef}^c is defined by the relation

$$\frac{1}{\tau_{ef}^c} = \frac{1}{\tau_f} - \frac{1}{\tau_c} \tag{A.41}$$

so that

$$\tau_{ef}^c = \frac{\tau_c \tau_f}{\tau_c - \tau_f} \tag{A.42}$$

Now rewriting

$$\tau_f = \frac{\tau_h}{1+x} \tag{A.43}$$

$$1 + \alpha = \frac{\tau_h}{\tau_e} \tag{A.44}$$

the obtained result is given by

$$x = \frac{T_e \alpha}{T_e - T_h} = \frac{\mu_h}{\mu_e - \mu_h} \frac{\tau_e - \tau_h}{\tau_e} \tag{A.45}$$

from which we achieve

$$\tau_{opt} = \tau_h \frac{(\mu_e - \mu_h)\tau_e}{\mu_e \tau_e - \mu_h \tau_h} =$$

$$= \tau_h \left[1 - \frac{\mu_h(\tau_e - \tau_h)}{\mu_e \tau_e - \mu_h \tau_h} \right] \tag{A.46}$$

$$\tau_{opt} \approx \left[1 - \frac{\mu_h(\tau_e - \tau_h)}{\mu_e \tau_e} \right] \tag{A.47}$$

A.2.1 A strange coincidence

Observing the blue curve in figure **??**, that describes the behavior of the maximum on varying the depth coordinate, it is possible to note how the second branch of this broken curve in the region 3 moves parallel to the green line that describes the integration time for the hole signal. This behavior can be seen even in the figure **??** where, in this case, the curve is parallel to the cyan line, related to the electron integration time.
It is clear that this behavior cannot be accidental. Indeed it can be obtained from the first order term of the Taylor series, developing the functional form that t_M assumes in the interested regions.
In fact considering, at the beginning, region 2

$$t_M = \tau^e_{ef} ln \left\{ \frac{\tau_e}{\tau_f} \left[1 + \frac{T_e \tau^h_{ef}}{T_h \tau^e_{ef}} \left(1 - e^{\frac{\xi T_h}{\tau^h_{ef}}} \right) \right] \right\} =$$

$$= \tau^e_{ef} ln \left(\frac{\tau_e}{\tau_f} \right) + \tau^e_{ef} ln \left[1 + \frac{T_e \tau^h_{ef}}{T_h \tau^e_{ef}} \left(1 - e^{\frac{\xi T_h}{\tau^h_{ef}}} \right) \right] \tag{A.48}$$

So developing at the first order, it becomes

$$t_M \approx \tau^e_{ef} ln \left(\frac{\tau_e}{\tau_f} \right) + T_e(\xi - 1) \tag{A.49}$$

Clearly this result is valid when both the arguments, for the exponential and for the logarithm functions, allow these approximation ($e^x \approx 1 + x$ and $ln(1 + x) \approx x$). In the same way, in region 3 (with the same approximations) we obtain:

$$t_M \approx \tau^h_{ef} ln \left(\frac{\tau_h}{\tau_f} \right) - T_h \xi \tag{A.50}$$

This result is important because, fitting the $t_M(\xi)$ curve with these equation, it is possible to obtain directly the parameters μ_e, τ_e, μ_h, and τ_h because of the relations among these equations and these parameters.

A.2.2 Twin shaping filter

The method of the "*twin shaping filter*", as explained in the fourth chapter [ref] consists essentially on filtering the signal through two different filter with different shaping times: a filter is "*fast*" (with shaping timeτ_{fs}) and one is "*slow*" (with

shaping timeτ_{sl}). Later on, it is calculated the ratio

$$R(\xi) = \frac{Q_M^{fs}}{Q_M^{sl}} \tag{A.51}$$

This ratio should depend only from ξ and not from the energy. So trough this ratio we can correct the signal with a series develop, in the $R(\xi)$ variable, that normally it is stopped at the first or the second order.
If we are interested in obtaining the relative depth ξ from the information provided through this method, we must invert the relation [ref] (if it is possible), or (that is the same) solving in ξ the second equality in the sequence below

$$Q_0 = \frac{Q_M^{fs}(\xi)}{F_M^{fs}(\xi)} = \frac{Q_M^{sl}(\xi)}{F_M^{sl}(\xi)} \tag{A.52}$$

Where the generic $F_M(\xi)$ function (both slow and fast) at the denominator can be expressed as $F_M(\xi, \tau_f) = F(t_M(\xi), \xi, \tau_f)$ (with $\tau_f = \tau_{fs}$ or $\tau_f = \tau_{sl}$) and where t_M is the time where the maximum is reached. This time depends on ξ and on the other parameters and, on varying this parameters, also the algebraical expression of F could vary, The calculations become more difficult and it is worthless to explain them here, even if, in some particular cases, it is possible to simplify them using the Taylor's series, truncated at the first order.
From all above decrypted, it is clear how difficult it is to find out an "easy"expression, even just approximated, that it allow us to correct the signal through the method of the twin shaping filter.

A.2.3 Correction of the signal

The correction for the charge losses are more easily calculable utilizing the information on the impact depth ξ by means the relation:

$$Q_0 = \frac{Q_M(\xi)}{F_M(\xi)} \tag{A.53}$$

where $Q_M(\xi)$ is the maximum of the collected charge and

About t_M there are three cases:

$$t_M(\xi) = \begin{cases} t_{M1}(\xi) & \text{in the region 1} \\ t_{M2}(\xi) & \text{in the region 2} \\ t_{M3}(\xi) & \text{in the region 3} \end{cases} \tag{A.54}$$

- In region 1 $t_{M1} = \theta_{C1}$ is the solution of the equation:

$$\frac{\tau_{ef}^e}{Te}\left[1 - \frac{\tau_f}{\tau_e} e^{-\frac{t}{\tau_{ef}^e}}\right] + \frac{\tau_{ef}^h}{T_h}\left[1 - \frac{\tau_f}{\tau_h} e^{-\frac{t}{\tau_{ef}^h}}\right] = 0 \tag{A.55}$$

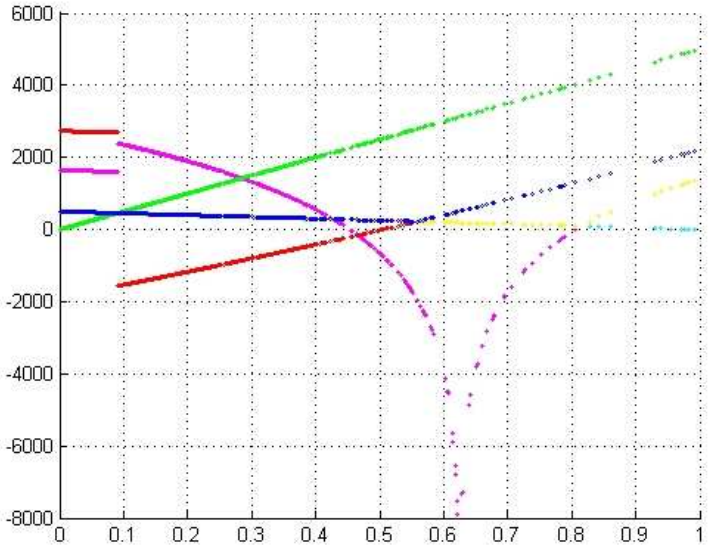

Figure A.6: In addition to the cyan and the green lines of the previous figures they appear the red broken curve, that it represents the t_M calculated for the region 2 and 3 with a $\tau_f = 2.5\mu s$, and the magenta curve similar to the red one, but calculated for $\tau_f = 1.0\mu s$. It is important to notice that the magenta curve has a branch (the left one) with no physical meaning. Finally the blue and yellow curves are the time when the maximum occurs (the "measured" t_M), respectively in the first and in the second case.

- Instead for the region 2 we have

$$t_{M2}(\xi) = \begin{cases} T_e(\xi) & \text{per } \theta_c(\xi) \geq T_e(\xi) \\ \theta_{C2}(\xi) & \text{per } T_e(\xi) > \theta_c(\xi) > T_h(\xi) \\ T_h(\xi) & \text{per } \theta_c(\xi) \leq T_h(\xi) \end{cases} \tag{A.56}$$

where

$$\begin{aligned} T_e(\xi) &= (1-\xi)T_e \\ \theta_{C2}(\xi) &= \tau_{ef}^h ln\left\{\frac{\tau_h}{\tau_f}\left[1 + \frac{T_h\tau_{ef}^e}{T_e\tau_{ef}^h}\left(1 - e^{\frac{(1-\xi)T_e}{\tau_{ef}^e}}\right)\right]\right\} \\ T_h(\xi) &= \xi T_h \end{aligned} \tag{A.57}$$

- Similarly for the region 3

$$t_{M3}(\xi) = \begin{cases} T_h(\xi) & \text{per } \theta_c(\xi) \geq T_h(\xi) \\ \theta_{C3}(\xi) & \text{per } T_h(\xi) > \theta_c(\xi) > T_e(\xi) \\ T_e(\xi) & \text{per } \theta_c(\xi) \leq T_e(\xi) \end{cases} \tag{A.58}$$

where

$$\begin{aligned} T_h(\xi) &= \xi T_h \\ \theta_{C3}(\xi) &= \tau_{ef}^h ln\left\{\frac{\tau_h}{\tau_f}\left[1 + \frac{T_h \tau_{ef}^e}{T_e \tau_{ef}^h}\left(1 - e^{\frac{(1-\xi)T_e}{\tau_{ef}^e}}\right)\right]\right\} \\ T_e(\xi) &= (1-\xi)T_e \end{aligned} \tag{A.59}$$

Finally we have done a simulation using the information concerning t_M and ξ to correct the charge collected. The simulation result are shown in the figure below. As input we have simulated a source with gaussian energy distribution centered on $122keV$ and with standard deviation of $0.1keV$ (the line with magenta spots on the cyan line on the figure). Then we have calculated the sensor response (the red spots curve) and also the signal corrected with the information concerning the depth ξ and the time when the maximum occurs t_M[1], discretizing the measure of the time with steps of $10ns$ for the green spots line on the yellow line and of $1ns$ for the blue spots line on the cyan line: As it is shown, in the second case, the input line (concerning the $122keV$ source) and the output line almost coincide and it is clear that, even with a discretization rate ten time lower, we gain a good correction the same.

[1]This information is redundant because it is achievable from ξ.

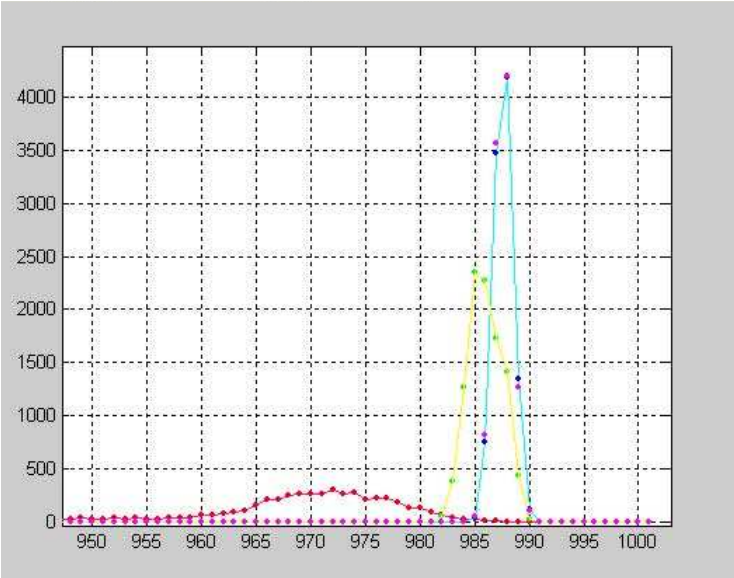

Figure A.7: magenta spots curve=input, red spots curve=output not correct, green spots curve=correction with discretization time of $10ns$ and finally of $1ns$ for the blue spots line.

Appendix B

Electronics: schematics

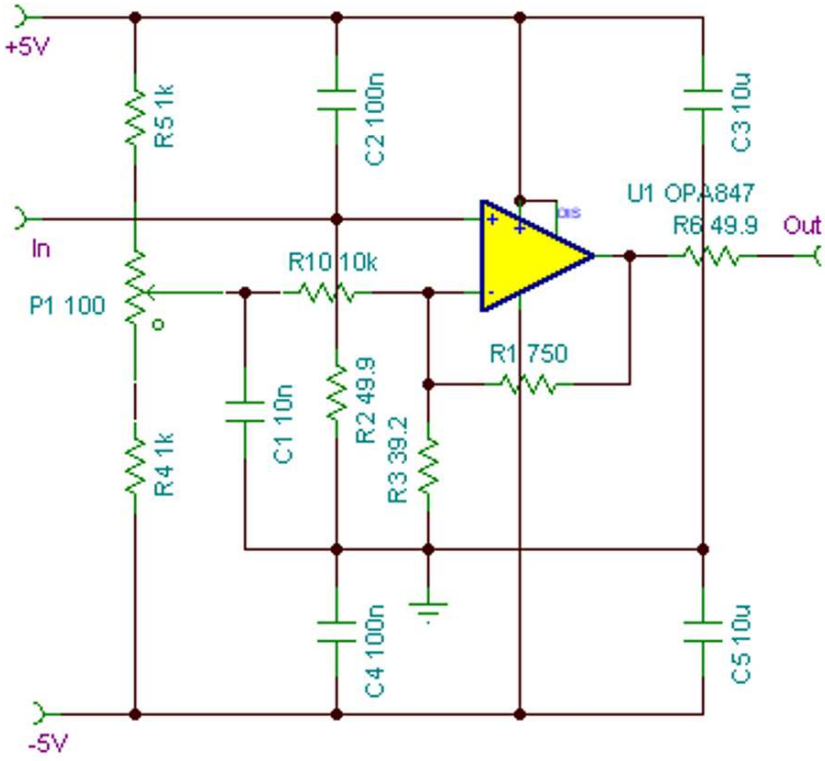
+5V
R5 1k
C2 100n
C3 10u
U1 OPA847
R6 49.9
Out
In
P1 100
R10 10k
R1 750
C1 10n
R2 49.9
R3 39.2
R4 1k
C4 100n
C5 10u
-5V

Figure B.1

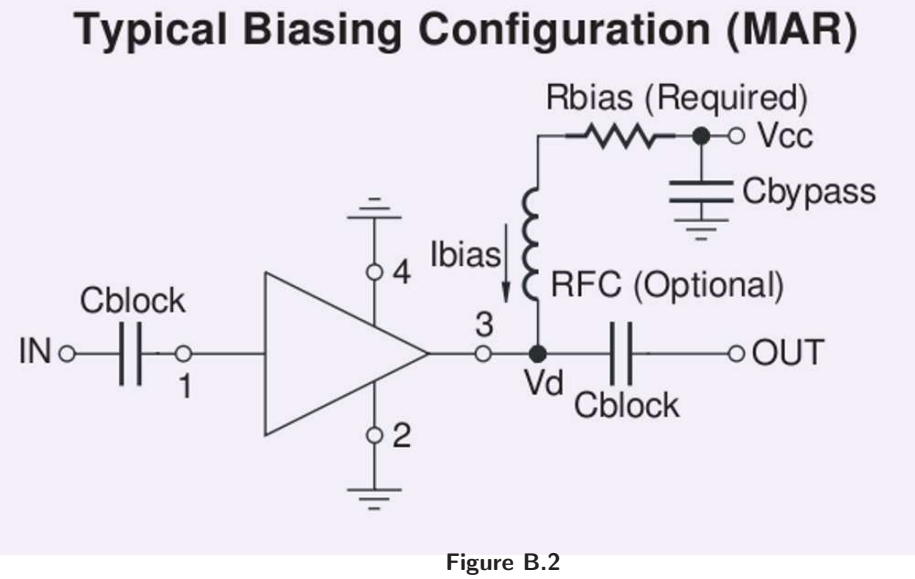
Typical Biasing Configuration (MAR)
Rbias (Required)
Vcc
Cbypass
Ibias
RFC (Optional)
4
3
Cblock
IN
1
Vd
OUT
Cblock
2

Figure B.2

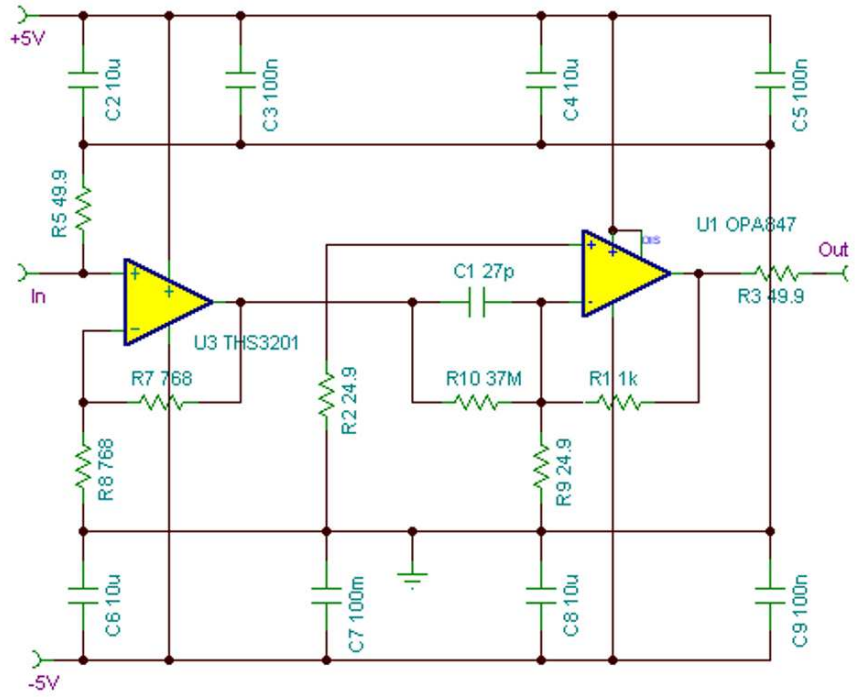

Figure B.3

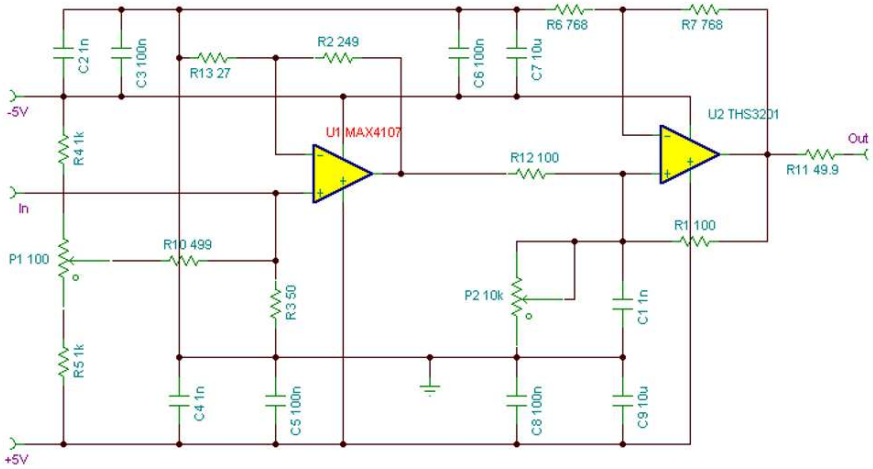

Figure B.4

Appendix C

Fitting and Acquisition programs

In this appendix we report the codes for the acquisition and the fitting programs. The acquisition program is developed in Labview programming language while the other programs are written in matlab code.

C.1 FitGlob

```
function [res1,res2,res3,res4,res5,res6,res7,res8,res9] = FitGlob
(data) % FitGlob(pid,spd,bpd)


% Funzione di filtraggio complessivo degli eventi di assorbimento
% gamma da parte del sensore letti attraverso un CSP.

[pid,spd,bpd]   =FitSing(data);
% filtraggio dati e parametri iniziali
ipd     =bpd;

func    ='mod_4';

[s1,s2] =size(spd);
ind     =pid(:,13);

m=5;                              % numero di iterazioni
meanchi  =zeros(m,1);
CHI_G    =zeros(m,1);
h1=waitbar(0);

for k=1:m
```

```
    p       =zeros(1,7);
    p(1)    =mean(bpd(:,5));    % TstTem
    p(2)    =mean(bpd(:,6));    % TstThm
    p(3)    =mean(bpd(:,7));    % tauf
    p(4)    =mean(bpd(:,8));    % TauTe
    p(5)    =mean(bpd(:,9));    % TauTh
    p(6)    =mean(bpd(:,10));   % TauDe
    p(7)    =mean(bpd(:,11));   % TauDh

    pars        =zeros(s1,6);
    pars(:,1)   =bpd(:,1);      % Ampl
    pars(:,2)   =bpd(:,2);      % offest
    pars(:,3)   =bpd(:,3);      % Tst
    pars(:,4)   =bpd(:,4);      % xi
    pars(:,5)   =pid(:,12);     % noise
    pars(:,6)   =ipd(:,6);      % Th

    choice  =[p(1),p(2),p(3),p(4),p(5),p(6),p(7)];
      % Parametri iniziali.

%     cm1     =['set lim 1 ',num2str(0.67*p(1)),' ',
%               num2str(1.5*p(1))];
%                       % configuro i limiti per p(1)=TstTem
%     cm2     =['; set lim 2 ',num2str(15*p(1)),' ',
%               num2str(50*p(1))];
%                       % configuro i limiti per p(2)=TstThm
%     cm3     =['; fix 3'];
%     cm3     =['; set lim 3 ',num2str(0.7*p(3)),' ',
%               num2str(1.5*p(3))];
%                       % configuro i limiti per p(3)=tauf
%     cm4     =['; set lim 4 ',num2str(0.30*p(4)),' ',
%               num2str(3.0*p(4))];
%                       % configuro i limiti per p(4)=taue
%     cm5     =['; set lim 5 ',num2str(0.25*p(5)),' ',
%               num2str(4.0*p(5))];
%                       % configuro i limiti per p(5)=tauh
%     cm6     =['; set lim 6 ',num2str(0.20*p(6)),' ',
%               num2str(5.0*p(6))];
%                       % configuro i limiti per p(6)=taud
%     cm6     =['; fix 6'];
%     cm7     =['; set lim 7 ',num2str(0.20*p(7)),' ',
%               num2str(5.0*p(7))];
%                       % configuro i limiti per p(6)=taud
%     cm7     =['; fix 7'];

%     cm1     ='fix 1';
```

```
    cm1     ='set lim 1 21.5 86';
    cm2     ='; set lim 2 1 40';
    cm3     ='; fix 3';
    cm4     ='; set lim 4 50 1250';
    cm5     ='; set lim 5 30 1500';
    cm6     ='; set lim 6 33 7500';
    cm7     ='; set lim 7 33 7500';

    commands=strcat(cm1,cm2,cm3,cm4,cm5,cm6,cm7,'; minimize;
                    improve');  %; set print out 0');
    [bps1,eps1,chi1]  =MEFit(spd,pars,'mod_4',choice,commands);
% fit globale
    CHI_G(k,1)      =chi1;

    p       =zeros(s1,4);
    p(:,1)  =bpd(:,1);      % Ampl
    p(:,2)  =bpd(:,2);      % Offset
    p(:,3)  =bpd(:,3);      % Tst
    p(:,4)  =bpd(:,4);      % xi

    x           =[1:s2];
    erry        =(pid(:,12)*ones(1,s2));

    BPS         =zeros(s1,11);
    EPS         =zeros(s1,11);
    CHI_S       =zeros(s1,1);

    for i=1:s1  % FIT DATO PER DATO
        i %#ok<NOPRT>
        inp     =[x',spd(i,:)',erry(i,:)'];
        choice  =[p(i,1),p(i,2),p(i,3),p(i,4),bps1(1),bps1(2),
                  bps1(3),bps1(4),bps1(5),bps1(6),bps1(7)];
                        % Parametri iniziali.

%         cm1     =['set lim 1 ',num2str(0.8*p(i,1)),' ',
%                   num2str(1.25*p(i,1))];
%                                 % configuro i limiti per p(1)=Ampl
%         cm2     =['fix 2'];     % Fisso l'offset (a zero)
%         cm3     =['; fix 3'];   % Fisso il Tst
%         cm7     =['; set lim 7 ',num2str(0.7*p(i,7)),' ',
%                   num2str(1.5*p(i,7))];
%                           % configuro i limiti per p(7)=tauf

        cm2     =['; set lim 2 ',num2str(p(i,2)-pid(i,12)/20),' ',
                  num2str(p(i,2)+pid(i,12)/20)];
                        % configuro i limiti per p(2)=offset.
```

```
        cm3     =[’; set lim 3 ’,num2str(0.9*p(i,3)-500),’ ’,
                  num2str(1.1*p(i,3)+500)];
                        % configuro i limiti per p(3)=Tst.
        cm4     =[’; set lim 4 0 1’];
                        % configuro i limiti per p(4)=xim
        cm5     =[’; fix 5’];
        cm6     =[’; fix 6’];
        cm7     =[’; fix 7’];
        cm8     =[’; fix 8’];
        cm9     =[’; fix 9’];
        cm10    =[’; fix 10’];
        cm11    =[’; fix 11’];

        commands   =strcat(cm2,cm3,cm4,cm5,cm6,cm7,cm8,cm9,cm10,
                           cm11,’; minimize; improve’);
                          %; set print out 0’);
        [bps2,eps2,chi2]=SEFit(inp,’mod_6’,choice,commands);
                          % fit dato per dato

        BPS(i,:) =bps2;
        EPS(i,:) =eps2;
        CHI_S(i) =chi2;
    end
    bpd=BPS;
    meanchi(k)=mean(CHI_S);
    waitbar(k/m,h1)
end
close(h1)

%%%%%%%%%%%%%%%%%%%%%%%%%%%%%%%%%%%%%%%%%%%%%%%%
% BLOCCO DI PLOT: RICORDARSI DI DECOMMENTARE FUNC PER USARLO

for i=1:s1
    data =[x’,spd(i,:)’,erry(i,:)’];
    str  =struct(’func’, func,’data’, data);
    res0 =funcplotta(BPS(i,:),str); %#ok<NASGU>
end
%%%%%%%%%%%%%%%%%%%%%%%%%%%%%%%%%%%%%%%%%%%%%%%%

% OUTPUT
res1=BPS;
res2=[EPS(:,1:4),ones(s1,1)*eps1];
res3=CHI_S;
res4=meanchi;
res5=CHI_G;
res6=ind;
```

```
res7=pid;
res8=spd;
res9=ipd;

% SALVATAGGIO DATI SU DISCO
save BPS.txt BPS -ASCII;
save EPS.txt EPS -ASCII;
save CHIS.txt CHI_S -ASCII;
save MCHI.txt meanchi -ASCII;
save CHIG.txt CHI_G -ASCII;
save IND.txt ind -ASCII;
save PID.txt pid -ASCII;
save SPD.txt spd -ASCII;
save IPD.txt ipd -ASCII;
```

C.1.1 FitSing

```
 function [res0,res1,res2,res3,res4]=FitSing(inp)

% Funzione che trova i parametri iniziali per la funzione
% GLOBALFIT.M e  seleziona gli eventi buoni con una analisi su
% rumore, massimi e minimi dei singoli eventi e una successiva
% analisi sul chi^2.

%%%%%%%%%%%%%%%%%%%%%%%%%%%%%%%%%%%%%%%%%%%%%%%%%%%%%%%%%%%%%%%%%%%%%%%%%%%
% % DEFINIZIONE DELLA MATRICE BG PER IL FITTING
% global BG;
% BG=zeros(100,250);
% p=0:0.1:24.9;
% t=eps+0:0.1:9.9;
% for j=1:250
%     for k=1:100;
%         BG(k,j)=quadgk(@(x)besselgauss(x,p(j)),0,t(k));
%     end
% end
%%%%%%%%%%%%%%%%%%%%%%%%%%%%%%%%%%%%%%%%%%%%%%%%%%%%%%%%%%%%%%%%%%%%%%%%%%%

[s1,s2] =size(inp);
L1      =50;                % Lunghezza minima prima del segnale
n       =20;                % lunghezza dell'array di filtraggio
m       =50;                % costante per il calcolo di Ampl
x       =[1:s2];
x1      =[-n:n];
gauss   =exp(-(2*x1/n).^2); % funzione di filtro
norm    =sum(gauss);        % calcolo della normalizzazione
gauss   =gauss/norm;        % funzione normalizzata
```

```
%%%%%%%%%%%%%%%%%%%%%%%%%%%%%%%%%%%%%%%%%%%%%%%%%%%%
% GD    =zeros(s1,s2+2*n);
% GI    =zeros(s1,s2+2*n);

% for i=1:s1
%     GI(i,:)     =conv(inp(i,:),gauss)/norm;
% end
%%%%%%%%%%%%%%%%%%%%%%%%%%%%%%%%%%%%%%%%%%%%%%%%%%%%

GI      =conv2(inp,gauss);      % segnale filtrato
MGI     =max(GI,[],2);          % massimo del segnale filtrato
mGI     =min(GI,[],2);          % minimo del segnale filtrato
Mm      =MGI-mGI;               % massimo meno minimo
thres   =(MGI+mGI)/2;           % definizione del threshold

Ithres  =zeros(s1,1);
error   =zeros(s1,1);
offset  =zeros(s1,1);
mask    =zeros(s1,1);
for i=1:s1
%     Ithres(i)   =min(max(find(GI(i,:)>=thres(i),1)-2*n,L1),s2);
                    % Indice (tempo) di attraversamento del threshold
    Ithres(i) =min(max(min((find(GI(i,:)>=thres(i))))-2*n,L1),s2);
                    %#ok<MXFND> % codice per matlab precedenti
    error(i)    =std(inp(i,1:Ithres(i)-5*n));
                    % noise
    offset(i)   =mean(inp(i,1:Ithres(i)-5*n),2);
                    % offset
    mask(i)     =(Mm(i)>5*error(i) & MGI(i)<1.50 & mGI(i)>-0.50);
                    % maschera di controllo
end

ind     =find(Ithres>L1 & mask>0);      % prima selezione eventi
% ind     =[1:s1]';                     % annulla selezione eventi
% Ampl    =mean(Mm(ind)-2*error(ind));  % calcola l'ampiezza media
% (senza prodedura di fit)
off     =offset(ind);
Tst     =Ithres(ind);
err     =error(ind);
out     =inp(ind,:);
s       =size(ind,1);
Ampl    =ones(s,1)*0.76;

%%%%%%%%%%%%%%%%%%%%%%%%%%%%%%%%%%%%%%%%%%%%%%%%%%%%%%%%%%%%%%%%%
% %Ampl    =zeros(s,1);
```

```
% TM      =zeros(s,1);
% for i=1:s   % FITTING PER OTTENERE AMPIEZZA E TEMPO DI MASSIMO
%     xpf             =x(Tst(i)+m:end);
%     ypf             =out(i,Tst(i)+m:end);
%     epf             =err(i)* ones(1,s2-(Tst(i)+m)+1);
% %%%%%%%%%%%%%%%%%%%%%%%%%%%%%%%%%%%%
% % FIT PARABOLICO
% %     pars            =polyfit(xpf,ypf,2);
% %     poly            =polyval(pars,xpf);
% %     [Ampl(i),TM(i)] =max(poly);
% %%%%%%%%%%%%%%%%%%%%%%%%%%%%%%%%%%%%
%
%     bpf         =fit([xpf',ypf',epf'],'spec',[2.2e-4,-5e-3,-4e-3],
%                      'set lim 1 1e-5 10');
%     bpf         =fit([xpf',ypf',epf'],'spec',[0.7,-2e-3,-3e-5],
%                      'set lim 1 1e-3 10');
%     fun         =(bpf(1)*xpf+bpf(2)*ones(size(xpf)))
%                      .*exp(-bpf(3)*xpf); % per fit parabolico
%     fun         =bpf(1)*(ones(size(xpf))-exp(bpf(2)*xpf))
%                       .*exp(bpf(3)*xpf); % per fit 'SPEC'
%     [Ampl(i),TM(i)] =max(fun);
%     Ampl(i)         =Ampl(i)-off(i);
%     if Ampl(i)<=0
%         Ampl(i)=mean(Mm(ind)-2*error(ind));
%     end
%
% %%%%%%%%%%%%%%%%%%%%%%%%%%%%%%%%%%%%
% % BLOCCO DI PLOT
%
% %     figure
% %     plot(xpf,ypf,'.r');
% %     hold on
% %     grid on
% %     plot(xpf,fun,'b')
% %%%%%%%%%%%%%%%%%%%%%%%%%%%%%%%%%%%%
% end
%%%%%%%%%%%%%%%%%%%%%%%%%%%%%%%%%%%%%%%%%%%%%%%%%%%%%%%%%%%%%%%%%%%%%%%%%%%%%%%

% DEFINIZIONE PARAMETRI INIZIALI
pars    =[Ampl,off,Tst,ones(s,1)*[0.4,173,11,31700,250,150,1e3,
  1e3],err,ind]; %10ns
% pars    =[Ampl,off,Tst,ones(s,1)*[0.4,43,11,31700,250,150,1e3,
%     1e3],err,ind]; %10ns
% pars    =[ones(s,1)*Ampl,off,Tst,ones(s,1)*[0.5,50,500,31500,
%     100,80,1000,1e4],err,ind]
%       % si usa senza la procedura di fit
```

```
% res0=pars;
% return

% st=round(0.20*s2);
% sp=s2;
% [S1,S2]     =size(out(:,st:sp));
[S1,S2]     =size(out);

p       =zeros(S1,13);
p(:,1)  =pars(:,1);         % Ampl
p(:,2)  =pars(:,2);         % offset
p(:,3)  =pars(:,3);         % Tst
p(:,4)  =pars(:,4);         % xim
p(:,5)  =pars(:,5);         % TstTem
p(:,6)  =pars(:,6);         % TstThm
p(:,7)  =pars(:,7);         % tauf
p(:,8)  =pars(:,8);         % TauTe
p(:,9)  =pars(:,9);         % TauTh
p(:,10) =pars(:,10);        % TauDe
p(:,11) =pars(:,11);        % TauDh
p(:,12) =pars(:,12);        % stdev
p(:,13) =pars(:,13);        % ind

% ind         =pars(13);
x           =[1:S2];
erry        =p(:,12)*ones(1,S2);

BP          =zeros(S1,11);
EP          =zeros(S1,11);
CHI         =zeros(S1,1);
% h           =waitbar(0);

for i=1:S1  % PRIMO FITTING EVENTO PER EVENTO PER RICAVARE I
            % PARAMETRI DI PARTENZA PER GLOBALFIT.M
    i %#ok<NOPRT>
%     data        =[x',out(i,st:sp)',erry(i,:)'];
    data        =[x',out(i,:)',erry(i,:)'];

    choice      =[p(i,1),p(i,2),p(i,3),p(i,4),p(i,5),p(i,6),
                  p(i,7), p(i,8),p(i,9),p(i,10),p(i,11)];

% ,p(i,12)];    % Parametri iniziali.
%      choice     =[p(i,1),p(i,2),p(i,3),p(i,4),51.485,492.23,
%                   103000,143.42,88.722,919.49,1000];
```

```
%     cm1         =['fix 1'];
%     cm1         =['; set lim 1 ',num2str(0.8*p(i,1)),' ',
%                   num2str(1.1*p(i,1))];
%                       % configuro i limiti per p(1)=Ampl
%     cm1         =['set lim 1 0.72 0.78']
%     cm2         =['fix 2'];
%                       % configuro i limiti per p(2)=offset.
%     cm2         =['set lim 2 ',num2str(p(i,2)-p(i,14)/20),'',
%                   num2str(p(i,2)+p(i,14)/20)];
%     cm3         =['set lim 3 ',num2str(L1),' ',num2str(S2)];
%     mstr        =S2-3200;
%     cm5         =['; fix 5'];
%     cm6         =['; fix 6'];
%     cm6         =['; set lim 6 ',num2str(1*p(i,5)),' ',
%                   num2str(10*p(i,5))];
%                       % configuro i limiti per p(6)=TstThm
%     cm7         =['; set lim 7 ',num2str(0.7*p(i,7)),' ',
%                   num2str(1.5*p(i,7))];
%                       % configuro i limiti per p(7)=tauf
%     cm8         =['; fix 8'];
%     cm9         =['; fix 9'];
%     cm10        =['; fix 10'];
%     cm11        =['; fix 11'];
%     cm11        =['; set lim 11 ',num2str(0.5*p(i,11)),' ',
%                   num2str(1.5*p(i,11))]; % configuro i limiti.
%     cm12        =['; set lim 12 ',num2str(0.5*p(i,12)),' ',
%                   num2str(1.5*p(i,12))]; % configuro i limiti.

    mstr =S2-5000;
    cm3         =['set lim 3 ',num2str(mstr),' ',num2str(S2)];
    cm4         =['; set lim 4 0 1'];
                    % configuro i limiti per p(4)=xim
    cm5         =['; set lim 5 ',num2str(0.7*p(i,5)),' ',
                  num2str(1.4*p(i,5))];
                    % configuro i limiti per p(5)=TstTem
    cm6         =['; set lim 6 2 30'];
    cm7         =['; fix 7'];
    cm8         =['; set lim 8 ',num2str(0.15*p(i,8)),' ',
                  num2str(5.0*p(i,8))];
                    % configuro i limiti per p(8)=taue
    cm9         =['; set lim 9 ',num2str(0.2*p(i,9)),' ',
                  num2str(10.0*p(i,9))];
                    % configuro i limiti per p(9)=tauh
    cm10        =['; set lim 10 ',num2str(0.04*p(i,10)),' ',
                  num2str(10.0*p(i,10))];
                    % configuro i limiti per p(10)=taud
```

```
    cm11        =['; set lim 11 ',num2str(0.04*p(i,11)),' ',
                  num2str(10.0*p(i,11))];

    commands   =strcat(cm3,cm4,cm5,cm6,cm7,cm8,cm9,cm10,cm11,';
                       minimize; improve'); %; set print out 0')
%     commands   =strcat('minimize; improve');

    [bestpars,errorpars,chi]=SEFit(data,'mod_4',choice,commands);
    BP(i,:)     =bestpars;
    EP(i,:)     =errorpars;
    CHI(i,1)    =chi;
    pars(i,12)  =std(inp(ind(i),1:round(min(BP(i,3)-1,S2))));
    out(i,:)    =out(i,:)-BP(i,2)*ones(1,s2); % Azzeramento OFFSET

%     out(i,st:sp)=out(i,st:sp)-BP(i,2)*ones(1,S2);
%                         % Azzeramento dell'OFFSET
%     waitbar(i/S1,h);

end
% close(h);

IND =find(CHI<10);  % check per il rigetto dei dati non buoni
% IND=[1:S1]';        % li piglia tutti

% % %%%%%%%%%%%%%%%%%%%%%%%%%%%%%%%%%%%%%%%%%%%%%%%%%%%%%%%%
% BLOCCO DI PLOT

PARS=BP;
PARS(:,2)=zeros(S1,1); % AZZERAMENTO DELL'OFFSET

func='mod_4';
for i=1:1:size(IND,1)
    j=IND(i);
    % mean(erry(j,:),2);
    data =[x',out(j,:)',erry(j,:)'];
    str  =struct('func', func,'data', data);
    res  =funcplotta(PARS(j,:),str); %#ok<NASGU>
end
% % %%%%%%%%%%%%%%%%%%%%%%%%%%%%%%%%%%%%%%%%%%%%%%%%%%%%%%%%
% OUTPUT
res0=pars(IND,:);
res1=out(IND,:);
res2=BP(IND,:);
res3=EP(IND,:);
res4=CHI(IND,:);
```

```
% res1=out(IND,st:sp);

% SALVATAGGIO DATI
save RES0.txt res0 -ASCII; %#ok<USENS>
save RES1.txt res1 -ASCII; %#ok<USENS>
save RES2.txt res2 -ASCII; %#ok<USENS>
save RES3.txt res3 -ASCII; %#ok<USENS>
save RES4.txt res4 -ASCII; %#ok<USENS>
```

C.1.2 SEFit

```
function [re1,re2,re3]= SEFit(data,func,strgs,commands)

% Funzione del tutto analoga a fit ma usata specificamente da
% FITSING (o FIL).

str                     =struct('func', func,'data', data);
[bestpars,errpars,chi]  =fminuit('ChiSing',strgs,str,'-c',commands);

% re0 =funcplotta(bestpars,str); %#ok<NASGU>
re1 =bestpars;
re2 =errpars;
re3 =chi/(size(data,1)-length(strgs));
```

C.1.2.1 ChiSing

```
function res=ChiSing(p,str)

func=str.func;
data=str.data;

x       =data(:,1);
y       =data(:,2);
erry    =data(:,3);
Sx      =size(x,1);

T       =x-p(3)*ones(Sx,1);
U       =ones(Sx,1);
xim     =p(4)*U;
Texi    =(U-xim)*p(5);
Th      =p(5)*p(6);
Thxi    =xim*Th;
TauTFe  =(1/p(8)-1/p(7))^-1;
TauTFh  =(1/p(9)-1/p(7))^-1;
TauDFe  =(1/p(10)-1/p(7))^-1;
```

```
TauDFh  =(1/p(11)-1/p(7))^-1;
TauTDe  =(1/p(8)-1/p(10))^-1;

% TauTDh  =(1/p(9)-1/p(11))^-1;
% TauED   =(1/p(8)-1/p(10))^-1;
% TauHD   =(1/p(9)-1/p(11))^-1;

switch func
    case 'mod_0'
        % MODELLO AD 1 SOLO PORTATORE SENZA DETRAPPING O CON
        % DETRAPPIG MOLTO VELOCE
        TauCompl=TauDFe;
        fun=(p(2)*U+p(1)*(U-exp(-T/TauCompl)).*(T>=0).*exp(-T/p(7)));

    case 'mod_1'
        % MODELLO A DUE PORTATORI SENZA DETRAPPING
        fun=(p(2)*U+(p(1)*((TauTFe/p(5))*(U-exp(-min(T,Texi)...
            /TauTFe))+(TauTFh/Th)*(U-exp(-min(T,Thxi)/TauTFh))))...
             .*(T>=0)).*exp(-T/p(7));

    case 'mod_2'
        % MODELLO A DUE PORTATORI CON DETRAPPING DEI PORTATORI VELOCI
        fun=(p(2)*U+(p(1)*((TauTFe/p(5))*((U-exp(-min(T,Texi)
            /TauTFe)))+(TauTFh/Th)*(U-exp(-min(T,Thxi)/TauTFh))))...
            .*(T>=0)+(p(1)*TauDFe*Texi.^2/(2*p(8)*p(10)*p(5)))...
            .*exp(Texi/p(7)).*(U-exp(-(T-Texi)/TauDFe)).*(T>Texi))...
            .*exp(-T/p(7));

    case 'mod_2_bis'
        % MODELLO A DUE PORTATORI CON DETRAPPING DEI PORTATORI VELOCI
        fun=(p(2)*U+(p(1)*((TauTFe/p(5))*((1-exp(-min(T,Texi)...
            /TauTFe)))+(TauTFh/Th)*(1-exp(-min(T,Thxi)/TauTFh))))...
            .*(T>=0)+(p(1)*TauDFe*Texi.^2/(2*p(8)*p(10)*p(5)))...
            .*exp(Texi/p(7)).*(U-exp(-(T-Texi)/TauDFe)).*(T>Texi))...
            .*exp(-T/p(7));

    case 'mod_3'
        % MODELLO A DUE PORTATORI CON DETRAPPING DEI PORTATORI VELOCI
        % (PERO' UN POCO PIU' LENTI rispetto ai modelli 2 e 2bis)
        Fxi=(TauTDe-(TauTDe+(1-p(4))*p(5))*exp(-(1-p(4))*p(5)...
            /TauTDe))/p(5);
        fun=(p(2)*U+(p(1)*((TauTFe/p(5))*((U-exp(-min(T,Texi)...
             /TauTFe)))+(TauTFh/Th)*(U-exp(-min(T,Thxi)/TauTFh))))...
            .*(T>=0)+(p(1)*TauDFe*Fxi/(p(10)-p(8)))...
            .*(U-exp(-T/TauDFe)).*(T>Texi)).*exp(-T/p(7));
```

```
case 'mod_4'
    % MODELLO A DUE PORTATORI ESATTO
    fun=(p(2)*U+p(1)*(((TauTFe/p(5))*(U-exp(-min(T,Texi)...
        /TauTFe))+(TauTFh/Th)*(U-exp(-min(T,Thxi)/TauTFh)))...
        .*(T>=0)+quadv(@(z)IntDetr(z,T,p(4),p(5),p(8),p(10),...
        TauTFe,TauDFe,Th,p(9),p(11),TauTFh,TauDFh),0,...
max(p(4),1-p(4)),1e-3))).*exp(-T/p(7));

case 'mod_4bis'
    % MODELLO A DUE PORTATORI ESATTO (versione a 2 integrazioni)
    fun=(p(2)*U+p(1)*(((TauTFe/p(5))*(U-exp(-min(T,Texi)...
        /TauTFe))+(TauTFh/Th)*(U-exp(-min(T,Thxi)/TauTFh)))...
        .*(T>=0)+quadv(@(z)BGint(z,T,p(5),p(8),p(10),TauTFe,...
         TauDFe),0,1-p(4)+eps,1e-3)+quadv(@(z)BGint(z,T,Th,...
         p(9),p(11),TauTFh,TauDFh),0,p(4)+eps,1e-3)))...
         .*exp(-T/p(7));

case 'mod_4_tris'
    % MODELLO A DUE PORTATORI ESATTO CON ALTRO METODO DI
    % INTEGRAZIONE (PIU' LENTO)
    fun=(p(2)*U+p(1)*(((TauTFe/p(5))*(U-exp(-min(T,Texi)...
        /TauTFe))+(TauTFh/Th)*(U-exp(-min(T,Thxi)/TauTFh)))...
        .*(T>=0)+quadv(@(z)integrBG(z,T,p(5),p(8),p(10),...
         TauTFe,TauDFe),0,1-p(4)+eps,1e-3)+quadv(@(z)integrBG...
         (z,T,Th,p(9),p(11),TauTFh,TauDFh),0,p(4)+eps,1e-3)))...
         .*exp(-T/p(7));

case 'mod_5'
    % MODELLO A DUE PORTATORI IN CUI SI E' TRASCURATO IL
    % DETRAPPING DEI PORTATORI VELOCI
    fun=(p(2)*U+p(1)*(((TauTFe/p(5))*(U-exp(-min(T,Texi)...
        /TauTFe))+(TauTFh/Th)*(U-exp(-min(T,Thxi)/TauTFh)))...
        .*(T>=0)+quadv(@(z)BGint(z,T,Th,p(9),p(11),TauTFh,...
        TauDFh),0,p(4)+eps,1e-3))).*exp(-T/p(7));

case 'mod_6'
    % MODELLO A DUE PORTATORI IN CUI IL DETRAPPING DEI
    % PORTATORI VELOCI E' TRATTATO IN MODO APPROSSIMATO
    Fxi=(TauTDe-(TauTDe+(1-p(4))*p(5))*exp(-(1-p(4))*p(5)...
        /TauTDe))/p(5);
    fun=(p(2)*U+p(1)*(((TauTFe/p(5))*(U-exp(-min(T,Texi)...
        /TauTFe))+(TauTFh/Th)*(U-exp(-min(T,Thxi)/TauTFh)))...
        .*(T>=0)+(TauDFe*Fxi/(p(10)-p(8))).*(U-exp(-T/TauDFe))...
        .*(T>Texi)+quadv(@(z)BGint(z,T,Th,p(9),p(11),TauTFh,...
        TauDFh),0,p(4)+eps,1e-3))).*exp(-T/p(7));
```

```
    otherwise
         disp('error')
end

chiq=sum(((y-fun)./erry).^2);   %/(length(x)-length(param));
res=chiq;
```

C.1.3 MEFit

```
 function [res1,res2,res3]= MEFit(data,pars,func,strgs,commands)

% Funzione del tutto analoga a FIT e a FIT1 ma usata specificamente
da FITGLOB.

str =struct('pfix',pars(:,1:4),'data',data,'erry',pars(:,5),
'func',func,'lim',pars(:,6));
[bestpars,errpars,chi]  =fminuit('ChiGlob',strgs,str,'-c',commands);

res1 =bestpars;
res2 =errpars;
res3 =chi; %/(size(data,1)*size(data,2)-length(strgs));
```

C.1.3.1 ChiGlob

```
 function [res1,res2]=ChiGlob(p,str)

pfix=str.pfix;
data=str.data;
erry=str.erry;
func=str.func;

% lim =str.lim;
% TH=max(lim);
% TH=500;

[s1,s2]=size(data);

x       =[1:s2];
Uc      =ones(s1,1);
Ur      =ones(1,s2);
U2      =ones(s1,s2);

T       =Uc*x-pfix(:,3)*Ur; % matrice S1 per S2
Ttr     =T';                % matrice S2 per S1
err     =erry*Ur;           % matrice S1 per S2
```

```
xi      =pfix(:,4);         % matrice colonna
Texi    =p(1)*(Uc-xi);      % matrice colonna
Texi2   =Texi*Ur;           % matrice S1 per S2
Th      =p(1)*p(2);
Thxi    =Th*xi;             % matrice colonna
Thxi2   =Thxi*Ur;           % matrice s1 per S2

Tstpexi =min(T,Texi2);      % matrice s1 per s2
Tstphxi =min(T,Thxi2);      % matrice s1 per s2

TauTFe   =(1/p(4)-1/p(3))^-1;    % parametro
TauTFh   =(1/p(5)-1/p(3))^-1;    % parametro
TauDFe   =(1/p(6)-1/p(3))^-1;    % parametro
TauDFh   =(1/p(7)-1/p(3))^-1;    % parametro
TauTDe  =(1/p(4)-1/p(6))^-1;     % parametro

% TauTDh  =(1/p(5)-1/p(7))^-1;   % parametro
% TauED   =(1/p(4)-1/p(6))^-1;  % parametro
% TauHD   =(1/p(5)-1/p(7))^-1;  % parametro
% Tstp    =s2;

norm    =s1*s2;

switch func
    case 'mod_0M'
        fun=pfix(:,2)*Ur+diag(pfix(:,1))*((TauTFe*diag(p(:,1))...
        ^-1)*(U2-exp(-T/TauDFe)).*(T>=0)).*exp(-T/p(3));

    case 'mod_1M'
        fun=(pfix(:,2)*Ur+diag(pfix(:,1))*((TauTFe*diag(p(:,1))...
             ^-1)*(U2-exp(-Tstpexi/TauTFe))+TauTFh*diag(p(:,2))...
             ^-1*(U2-exp(-Tstphxi/TauTFh))).*(T>=0)).*exp(-T/p(3));

    case 'mod_2'
    %     norm=0;
        fun =zeros(s1,s2);
        chi =zeros(s1,1);
        for i=1:s1
            fun(i,:)=(pfix(i,2).*Ur+pfix(i,1)*((TauTFe/p(1))...
                .*(Ur-exp(-Tstpexi(i,:)/TauTFe))+(TauTFh/p(2))...
                .*(Ur-exp(-Tstphxi(i,:)/TauTFh))).*(T(i,:)>=0)...
                +TauDFe*(pfix(i,1)*(Texi(i)^2)/(2*p(4)*p(6)...
                *p(1)))*exp(Texi(i)/p(3)).*(Ur-exp(-(T(i,:)...
                -Texi2(i,:))/TauDFe)).*(T(i,:)>Texi2(i,:)))...
                .*exp(-T(i,:)/p(3));
```

```
    chi(i)  =sum(((fun(i,:)-data(i,:))./err(i,:)).^2,2);

%         Tstp    =ceil(min(pfix(i,3)+max(p(2),TH),s2));
%         chi(i)  =sum(((fun(i,1:Tstp)-data(i,1:Tstp))...
%                   ./err(i,1:Tstp)).^2,2);
%         norm    =norm+Tstp;
    end

case 'mod_2M'
    fun=(pfix(:,2)*Ur+diag(pfix(:,1))*((TauTFe/p(1))*...
        (U2-exp(-Tstpexi/TauTFe))+(TauTFh/p(2))*(U2-exp(...
        -Tstphxi/TauTFh))).*(T>=0)+TauDFe*(diag(pfix(:,1))*...
        diag(Texi.^2)/(2*p(4)*p(6)*p(1)))*diag(exp(Texi/p(3)))...
        *(U2-exp(-(T-Texi2)/TauDFe)).*(T>Texi2)).*exp(-T/p(3));

case 'mod_3'
    % MODELLO A DUE PORTATORI CON DETRAPPING DEI PORTATORI VELOCI
    % (PERO' UN POCO PIU' LENTI rispetto ai modelli 2 e 2bis)
    Fxi=(TauTDe-(TauTDe+(1-p(4))*p(5))*exp(-(1-p(4))*p(5)...
        /TauTDe))/p(5);
    fun=(p(2)*U+(p(1)*((TauTFe/p(5))*((U-exp(-min(T,Texi)...
         /TauTFe)))+(TauTFh/Th)*(U-exp(-min(T,Thxi)/TauTFh))))...
        .*(T>=0)+(p(1)*TauDFe*Fxi/(p(10)-p(8))).*(U-exp(...
        -T/TauDFe)).*(T>Texi)).*exp(-T/p(7));

case 'mod_4'
    fun =zeros(s1,s2);
    chi =zeros(s1,1);
    for i=1:s1
        fun(i,:)=(pfix(i,2)*Ur+pfix(i,1)*(((TauTFe/p(1)))...
            *(Ur-exp(-Tstpexi(i,:)/TauTFe))+(TauTFh/Th)...
            *(Ur-exp(-Tstphxi(i,:)/TauTFh))).*(T(i,:)>=0)...
            +quadv(@(z)IntDetr(z,Ttr(:,i),pfix(i,4),p(1),...
            p(4),p(6),TauTFe,TauDFe,Th,p(5),p(7),TauTFh,...
            TauDFh),0,max(pfix(i,4),1-pfix(i,4)),1e-3)'))...
            .*exp(-T(i,:)/p(3));
         chi(i)  =sum(((fun(i,:)-data(i,:))./err(i,:)).^2,2);
     end

case 'mod_4bis'
    % MODELLO A DUE PORTATORI ESATTO (versione a 2 integrazioni)
    fun =zeros(s1,s2);
    chi =zeros(s1,1);
    for i=1:s1
        fun(i,:)=(pfix(i,2)*Ur+pfix(i,1)*(((TauTFe/p(1)))...
            *(Ur-exp(-Tstpexi(i,:)/TauTFe))+(TauTFh/Th)...
```

```
            *(Ur-exp(-Tstphxi(i,:)/TauTFh))).*(T(i,:)>=0)...
            +quadv(@(z)BGint(1-z,Ttr(:,i),p(1),p(4),p(6),...
            TauTFe,TauDFe),0,1-p(i,4)+eps,1e-3)'+quadv...
            (@(z)BGint(z,Ttr(:,i),Th,p(5),p(7),TauTFh,...
            TauDFh),0,p(i,4)+eps,1e-3)')).*exp(-T(i,:)/p(3));
        chi(i)  =sum(((fun(i,:)-data(i,:))./err(i,:)).^2,2);
    end

case 'mod_4_tris'
    % MODELLO A DUE PORTATORI ESATTO CON ALTRO METODO DI
    % INTEGRAZIONE (PIU' LENTO)
    fun =zeros(s1,s2);
    chi =zeros(s1,1);
    for i=1:s1
        fun(i,:)=(pfix(i,2)*Ur+pfix(i,1)*(((TauTFe/p(1))*...
            (Ur-exp(-Tstpexi(i,:)/TauTFe))+(TauTFh/Th)...
            *(Ur-exp(-Tstphxi(i,:)/TauTFh))).*(T(i,:)>=0)...
            +quadv(@(z)integrBG(1-z,Ttr(:,i),p(1),p(4),...
            p(6),TauTFe,TauDFe),0,1-p(i,4)+eps,1e-3)'+quadv...
            (@(z)integrBG(z,Ttr(:,i),Th,p(5),p(7),TauTFh,...
            TauDFh),0,p(i,4)+eps,1e-3)')).*exp(-T(i,:)/p(3));
         chi(i)   =sum(((fun(i,:)-data(i,:))./err(i,:)).^2,2);
    end

case 'mod_5'
    % MODELLO A DUE PORTATORI IN CUI SI E' TRASCURATO IL
    % DETRAPPING DEI PORTATORI VELOCI
    fun =zeros(s1,s2);
    chi =zeros(s1,1);
    for i=1:s1
        fun(i,:)=(pfix(i,2)*Ur+pfix(i,1)*(((TauTFe/p(1))...
            *(Ur-exp(-Tstpexi(i,:)/TauTFe))+(TauTFh/Th)...
            *(Ur-exp(-Tstphxi(i,:)/TauTFh))).*(T(i,:)>=0)...
            +quadv(@(z)BGint(z,Ttr(:,i),Th,p(5),p(7),TauTFh,...
            TauDFh),0,p(i,4)+eps,1e-3)')).*exp(-T(i,:)/p(3));
        chi(i)  =sum(((fun(i,:)-data(i,:))./err(i,:)).^2,2);
    end

case 'mod_6'
    % MODELLO A DUE PORTATORI IN CUI IL DETRAPPING DEI
    % PORTATORI VELOCI E'TRATTATO IN MODO APPROSSIMATO
    fun =zeros(s1,s2);
    chi =zeros(s1,1);
    for i=1:s1
        Fxi(i,:)=(TauTDe-(TauTDe+(1-p(i,4))*p(1))*exp(-(1...
            -p(i,4))*p(1)/TauTDe))/p(1);
```

```
            fun(i,:)=(pfix(i,2)*Ur+pfix(i,1)*(((TauTFe/p(1))...
                *(Ur-exp(-Tstpexi(i,:)/TauTFe))+(TauTFh/Th)...
                *(Ur-exp(-Tstphxi(i,:)/TauTFh))).*(T(i,:)>=0)...
                +(TauDFe*Fxi/(p(6)-p(4))).*(1-exp(-T(i,:)...
                /TauDFe)).*(T(i,:)>Texi(i,:))+quadv(@(z)BGint(z,...
                Ttr(:,i),Th,p(5),p(7),TauTFh,TauDFh),0,p(i,4)+...
                eps,1e-3)')).*exp(-T(i,:)/p(3));
            chi(i)  =sum(((fun(i,:)-data(i,:))./err(i,:)).^2,2);
        end

    otherwise
        disp('error')
end

res2=norm-length(p);
res1=sum(chi,1)/(res2);                 % chi quadro ridotto MOD_2BIS

% res1=sum(chi,1);                      % chi quadro MOD_2BIS
% res1=sum(sum(((fun-data)./err).^2));  % chi quadro non ridotto
% res1=res1/norm;                       % chi quadro ridotto
```

C.2 Other functions

These functiosn are used to calculate the detrapping contribute, in particular the firs function is the most used, because it is the most efficient one.

C.2.1 IntDetr

```
function res=IntDetr(z,T,xi0,Te,TauTe,TauDe,TauTFe,TauDFe,Th,...
                     TauTh,TauDh,TauTFh,TauDFh)

% Funzione che calcola l'integrale della bessel per una gaussiana
% per mezzo di una interpolazione su una look-up table a due
% parametri e che fa il prodotto di questa con un esponeziale.
% Richiede che nel workspace sia definita una variabile GLOBAL
% di nome BGEP. Questa funzione \'e una evoluzione di BGint in
% quanto calcola in una sola volta il termine elettronico e quello
% lacunare, risparmiando una chiamata a QUADV

x=0:0.1:13.0;
y=0:0.1:33.2;

s=size(T,1);

Tze=z*Te*ones(s,1);
```

```
Pe=2*sqrt(Tze*TauDFe/(TauTe*TauDe));
Thetae=sqrt((T-Tze)/TauDFe).*(T>=Tze).*(z<=(1-xi0));

Tzh=z*Th*ones(s,1);
Ph=2*sqrt(Tzh*TauDFh/(TauTh*TauDh));
Thetah=sqrt((T-Tzh)/TauDFh).*(T>=Tzh).*(z<=xi0);

Theta=[Thetae;Thetah];
P=[Pe;Ph];

global BGEP; %#ok<TLEV>
if any(isnan(interp2(x,y,BGEP,Theta,P)))
    keyboard
    return
end

I2BGEP=interp2(x,y,BGEP,Theta,P).*exp((P.^2)/4-[Tze/TauTFe;Tzh...
        /TauTFh]);
res=I2BGEP(1:s,:)+I2BGEP(s+1:end,:);
```

C.2.2 BGint

```
function res=BGint(z,T,Tc,TauT,TauD,TauTF,TauDF)

% Funzione che calcola l'integrale della bessel per una gaussiana
% per mezzo di una interpolazione su una look-up table a due
% parametri e che fa il prodotto di questa con un esponeziale.
% Richiede che nel workspace sia definita una variabile GLOBAL di
% nome BG.

x=0:0.1:9.9;
y=0:0.1:24.9;
s=size(T,1);

Tz=z*Tc*ones(s,1);
P=2*sqrt(Tz*TauDF/(TauT*TauD));
Theta=sqrt((T-Tz)/TauDF).*(T>=Tz);


if sum(isnan([P,Theta]))==0

    global BGEP; %#ok<TLEV>
    res=interp2(x,y,BGEP,Theta,P).*exp((P.^2)/4-Tz/TauTF);

else
    res=nan*ones(s,1);
```

```
end
```

C.2.3 integrBG

```
 function res=integrBG(z,T,Tc,TauT,TauD,TauTF,TauDF)

% Funzione sostituta di BGint che si usa col metodo di fitting
% MOD_4_BIS

s=size(T,2);
Tz=z*Tc;
p=2*sqrt(Tz*TauDF/(TauT*TauD));
time=(T-Tz*ones(1,s));
PHI=time/TauDF;
m=find(time>0, 1 ); % min(find(time>0));

Dint=zeros(1,s);
int=zeros(1,s);
Dint(m)=quadl(@(z)besselgauss(z,p,Tz,TauTF),0,PHI(m));
% Dint(m)=quad(@(z)besselgauss(z,Tz,TauT,TauD,TauTF,TauDF),0,...
          PHI(m),1e-3);
int(m)=Dint(m);
for i=m+1:s
    Dint(i)=quadl(@(z)besselgauss(z,p,Tz,TauTF),PHI(i-1),PHI(i));
    % Dint(m)=quad(@(z)besselgauss(z,Tz,TauT,TauD,TauTF,TauDF),...
              PHI(i-1),PHI(i),1e-3);
    int(i)=int(i-1)+Dint(i);
end

res=int;
```

C.3 Acquisition program

Appendix D

Other activities

In this last appendix we present briefly other activities accomplished during the Ph.D studies.

D.1 SGRIP

The SGRIP project is a $3D$ prototype for Laue lens telescope. In this project I have dealt with the linear module design. The linear modules are electronic boards that house the detector and the electronic circuits to filter and distribute the electronic power to anodes, cathodes and polarization strips on the detector. Below we report a paper presented for the next *SPIE Astronomical Telescopes and Instrumentation* 27 June - 2 July 2010, S. Diego California (USA).

D.2 Temperature controller

This electronic circuits it has been developed to hold stable the temperature of a detector exploiting ZnO nano-wire, that must work at about $300°C$. To keep stable the temperature we use a Wheatstone bridge. In this bridge we have two branches: a low resistance branch and a higher one. The low resistance branch is composed of two resistance: a power resistance R_0 (its value is 25Ω) and the platinum resistance R_{Pt} used to heat the detector. The high resistance branch is composed of a fix resistance R_1, with a value 100 times greater than the R_0 one (2500Ω), and of settable resistance R_x. The bridge is balance when

$$R_x = 100R_0 \tag{D.1}$$

The value of R_0 varies with the temperature, and then with the current flowing inside. A PID (Proportional-Integral-Derivative) circuit has the task of keeping balanced the bridge. When the resistance is too low the bridge is unbalanced and the PID supplies further current; on the contrary, when the resistance is too high the PID lowers the flowing current, stabilizing the temperature. It

is noteworthy that the platinum resistance R_{Pt} is the heating resistance and, at the same time, the temperature sensor. Indeed, exploiting the resistance-temperature characteristic of the platinum resistance, we set the value of R_x using the relation

$$R_x = 100 R_{Pt}(T) \tag{D.2}$$

to obtain the desired temperature T with a gap lower than $1K$ degree.
Below we show the schematic:

PROCEEDINGS OF SCIENCE

A 3D CZT prototype for Laue lens telescope

Ezio Caroli[1], **Natalia Auricchio,**
INAF/IASF-Bologna
Via Gobetti 101, I-40129 Bologna, Italy
E-mail: caroli@iasfbo.inaf.it; auricchio@iasfbo.inaf.it

Carl Budtz-Jorgensen, Irfan Kuvvetli
NSI/DTU, Technical University of Denmark
Juliane Maries vej 30, DK-2100 Copenhagen, Denmark
E-mail: carl@space.dtu.dk ; irfan@space.dtu.dk

Stefano del Sordo
INAF/IASF-Palermo,
Via Ugo La Malfa 153, I-90146 Palermo, Italy
E-mail: Delsordo@ifc.inaf.it

Rui M. Curado da Silva
Departamento de Fisica, Universidade de Coimbra,
P-3004-516 Coimbra, Portugal
E-mail: ruisilva@saturno.fis.uc.pt

Luciano Milano
Dipartimento di Fisica, Università di Ferrara,
Via Saragat 1, I-44100 Ferrara, Italy
E-mail: milano@fe.infn.it

Mauro E. Quadrini, Fabio Casini
INAF/IASF-Milano,
Via Bassini 15, I-20133 Milano, Italy
E-mail: mauro@iasf-milano.inaf.it;

Andrea Zappettini
CNR/IMEM,
Parco Area delle Scienze 37/A, I- 43124 Parma, Italy
E-mail: zapp@imem.cnr.it

Massimiliano Zanichelli
Dipartimento di Fisica, Università di Parma,
Parco Area delle Scienze 37/A, I- 43124 Parma, Italy
E-mail: massimiliano.zanichelli@fis.unipr.it

[1] Speaker

PROCEEDINGS OF SCIENCE

Lorenzo Natalucci, Pietro Ubertini
INAF/IASF-Roma,
Via Fosso del Cavaliere, I-00133 Frascati, Italy
E-mail: natalucci@iasf-roma.inaf.it, ubertini@iasf-roma.inaf.it

Abstract- The importance of hard X-ray astronomy (>10 keV) is now widely recognized. Recently both ESA and NASA have indicated in their guidelines for X- and γ-ray astronomy in the next decade the development of innovative instrumentation operating in the hard X- and soft gamma ray range where important scientific issues are still open, exploiting high sensitivity for spectroscopic imaging and polarimetric observations. In this framework, the development of new focusing optics based on Laue lenses operating from ~60 keV up to a few MeV is particularly challenging.
We describe the design concepts and the undergoing development of a three dimensional (3D) position sensitive device suitable for use as the basic unit of a high efficiency focal plane detector for a Laue lens telescope. The sensitive unit is a drift strip detector based on a CZT crystal, (19×8 mm^2 area, 2.4 mm thick), irradiated transversally to the electric field direction. The anode is segmented into 8 detection cells, each comprising one collecting strip and 8 drift strips. The drift strips are biased by a voltage divider, whereas the anode strips are held at 0 V. The cathode is divided in 4 horizontal strips for the reconstruction of the Z interaction position.
The 3D prototype will be made by packing 8 linear modules, each composed of one basic sensitive unit, bonded onto a supporting layer. The readout electronics will implement the new RENA-3 Asic and the data handling system will use custom designed FPGA based electronics to provide both the ASIC operation and the acquisition logic.

The Extreme sky: Sampling the Universe above 10 keV - extremesky2009
Otranto (Lecce) Italy
October 13-17, 2009

1.Introduction

In high energy astronomy, the next decade will be characterized by the development of new space instrumentation working in the energy range from the keV to the MeV region, where many important scientific issues are still open. In particular, the development of new instrumentation based on focusing instruments based on Laue lenses operating from ~50 keV up to a few MeV is particularly challenging [1].

To exploit the performance of Laue lenses telescope, new focal plane detectors for high energy (50-1000 keV) shall be developed providing: (i) high efficiency (>80%) up to the MeV region; (ii) moderate spatial resolution (1-3 mm); (iii) 3D sensitivity to photon interaction position for background rejection and high sensitivity polarimetric measurements; (iv) good spectroscopic resolution (few % at 100 keV).

Using the up to date room temperature semiconductor technology (CZT), we have proposed a focal plane detector configuration [2] that could reach several cm thickness without increasing too much the number of layers and pixels (i.e. electronic channels) by coupling two basic ideas for the CZT sensors configuration that are described in the following section.

2.The detector sensitive basic unit

The proposed 3D prototype is based on the use of CZT crystals in the Planar Transverse Field (PTF) configuration, as proposed by our group in the 1990's [3], in which the direction of the impinging photons (i.e. the optical axis of the sensor) is perpendicular to the charge collecting field. This configuration allows to increase the photon absorption thickness without increasing the charge collection distance (i.e. avoiding severe spectroscopic performance degradation) (Fig 1A). The drawback of the PTF irradiating geometry is that all the positions between the collecting electrodes are uniformly hit by radiation leading to a stronger effect of the difference in charge collection efficiency in the spectroscopic performance with respect to the standard irradiation configuration (PPF) through the cathode (Fig. 1B).

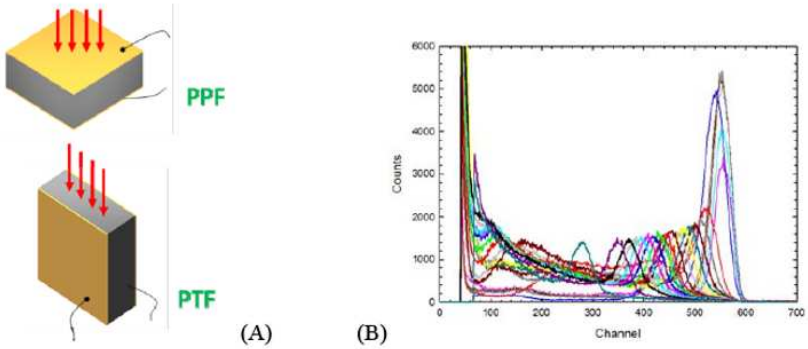

Figure 1. (A) Irradiating configurations for a solid state detector; (B) The energy spectra (measured with a IMEM/Italy CZT for a 150 keV beam at the ESRF /Grenoble) at different positions from the cathode, showing the effect on the charge collection efficiency.

Therefore in order to recover from this spectroscopic degradation and to improve the CZT sensitive unit performance, we have decided to use an anode made of an array of microstrips in a drift configuration: a thin collecting anode strip surrounded by guard strips with decreasing bias voltage. This anode configuration, proposed and studied at NSI/DTU in Copenhagen [4], allows the detector to be more sensitive to electron collection and less sensitive to hole collection, avoiding the degradation of the spectroscopic

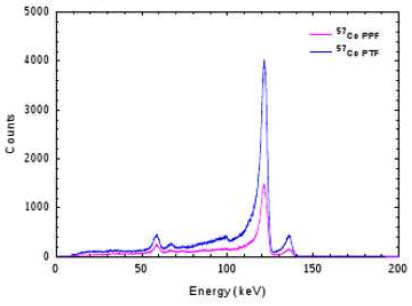

Figure 3. The spectra obtained with a CZT drift strip detector similar to the one proposed in PPF and PTF irradiation configurations. The detector shows a good spectroscopic response in both cases while the efficiency is clearly improved for PTF configuration.

response by the charge loss due to the hole trapping and providing a more uniform spectroscopic response (i.e. independent from the distance of the interaction from the collecting electrode).

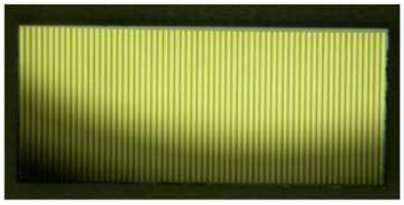

Figure 3. The CZT sensitive unit seen from the anode side that consists of a set of 63 micro-strips. The strips are 0.15 mm wide and have a pitch of 0.3 mm.

Finally in order to obtain 3D sensitivity for the photon interaction position, the cathode is segmented into 4 strips in the direction orthogonal to the anode ones. Therefore the final prototype becomes equivalent to a stack of thinner CZT horizontal layers with the advantage of not having any passive material between each layer.

Figure 3 shows the final CZT sensor unit that was realized using REDLEN Tech. CZT wafers cutting 8 single crystals of 19×8×2.4 mm^3. The microstrip set is divided in 8 equivalent pixels with a pitch of 2.4 mm, being only 8 strips connected to the readout electronics, while the others act as drift strips used, through a proper decreasing bias, to shape the charge collecting field. Each collecting strip is surrounded by 4 drift strips on each side.

3.The prototype electronics

The signals from the 64 anode collecting strips and the 32 cathodes are readout by three RENA-3 ASIC, placed on the analog front-end electronics (AFEE) [5]. The RENA-3 ASIC is a 36-channel charge sensitive amplifier self-triggering. Each channel includes a low-noise preamplifier, a shaper with sample/hold, and in addition a fast shaper that gives a trigger signal for coincident event detection. The signal range is selectable channel by channel over two full scales (equivalent to 200 keV and 1.3 MeV for CZT) as the peaking time that can ranges from 0.1 to 40 μs. The comparator thresholds can be adjusted through an 8 bit DAC on each channel in order to obtain an accurate and uniform threshold setting. A pole-zero cancellation circuit is available for minimizing pileup errors. All these features are selectable via software. Furthermore, the AFEE implements the detector high voltage power supply, low voltage power supply, the conditioning

Figure 4. The RENA-3 demo board realized to test the ASIC functionalities before the final readout electronics implementation.

electronics, the low and high voltage monitors, two temperature and humidity sensors for detector and electronics environment monitoring.

The Data Handling Electronics (DHE) is composed of a daughter board that provide the interface between the AFEE and the main data handling board. The DHE manages the detector high voltage power supply, and the energy ADC converters, the ASIC configurations, the coincidence logics, the detector operational parameters, and finally prepares the output data stream using a programmable data format (LABVIEW compatible). The main DHE board is based on a FPGA with embedded PPC and will be able to handle up to 128 independent channels via an Ethernet link.

Figure 5. The DHE main board currently under test. The FPGA (a Xlinx VIRTEX 5) core is clearly visible on the right together with the high density connectors to the I/F daughter board.

Item	*Characteristics*	N.
CZT crystal units	8×19×2.4 mm^3, used in PTF	8
Linear modules	100×30 mm^3, 0.5 mm thick Alumina	8
Active pixels/area	8×8 pixels/4 cm^2 (2.4x2.4 mm^2)	64
Active voxels /vol.	8×8×4 voxels/4 cm^3 (2.4x2.4x2 mm^3)	256
Electronics channels	128	
AFEE	Rena-3 ASIC (36 channels each)	3
CZT & ASIC's bias	250-300 V/ using DC-DC converters	2
ADC /DPE	4 ADC's and FPGA based board	
I/O Interface	LAN	
Power consumption	~20 W	

Table I. Main characteristics of the final 3D CZT prototype.

4.The 3D CZT prototype assembly

After the realisation of the basic sensitive unit, the second step is represented by assembling of the spectrometer linear module (Fig. 5a). We foresee the realisation of 8 linear modules each containing one CZT sensitive unit bonded on ceramic layer (Al_2O_3). On the ceramic layer each drift strip will be connected to the bias divider, while the anode collecting strips will be connected to front-end electronic channel pads through devoted filter circuits. On the same layer the cathode strip connections will also be realised as will the bias circuit and I/O pins to the AFEE electronics.

The final step is the packaging of the 8 linear modules to obtain the 3D position sensitive detector unit with 8×8 pixels (channels) and a total of 64×4 voxels. Figure 5b shows the current design of this support, that allows to flow an inert gas (e.g. N) inside the detector box for temperature stabilisation and humidity control. This box will be closed on the top by a light tight cover with a Be window. The detector box will be mechanical connected to the AFEE board where the linear modules I/O connectors will be mounted.

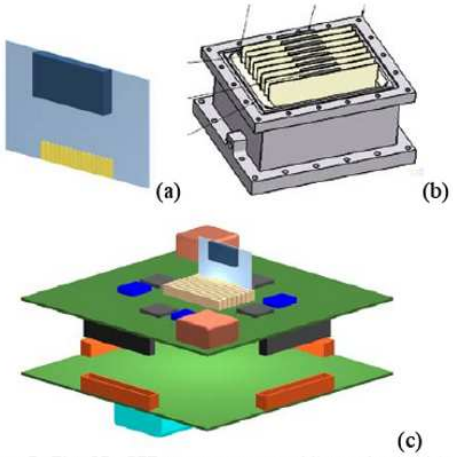

Figure 5. The 3D CZT prototype assembling scheme. (a) the CZT linear module; (b) the linear module packaging to form the detector unit; (c) a possible layout to assemble the detector unit with the AFEE (top green layer) and DHE (bottom green layer).

5.Conclusions

Currently we are realising the AFEE board and the definitive DHE board based on FPGA is under test. In the meanwhile we are going to start the realisation of the CZT linear modules. The final 3D CZT detector assembling is scheduled for next May and successively we have foreseen different test campaigns to study the performances using both radioactive sources and beam facilities.

References

[1] F. Frontera, et al., *Focusing of gamma-rays with Laue lenses: first results*, in "Ultraviolet to Gamma Ray", edited by M.J.L. Turner, K.A. Flanagan Eds, Proc. of SPIE Vol. 7011, 70111R, (2008)

[2] E. Caroli, et al., *A three-dimensional CZT detector as a focal plane prototype for Laue Lens telescope*, in "Ultraviolet to Gamma Ray", M.J.L. Turner, K.A. Flanagan Eds., Proc. of SPIE Vol. 7011, p. 70113G, (2008)

[3] F. Casali, et al., IEEE Trans. Nucl. Sci., Vol. 39, p. 598 (1992).

[4] I. Kuvvetli and C. Budtz-Jørgensen, *Pixelated CdZnTe drift detectors*, IEEE Trans. Nucl. Sci, Vol. 52, N. 5, p. 1975 (2005)

[5] T. O. Tumer, et al, *Performance of RENA-3 IC with position-sensitive solid-state detectors*, in "Hard X-Ray, Gamma-Ray, and Neutron Detector Physics X", A. Burger; L.A. Franks; R.B. James, Eds, Proc. of SPIE Vol. 7079, p. 7079F (2008)

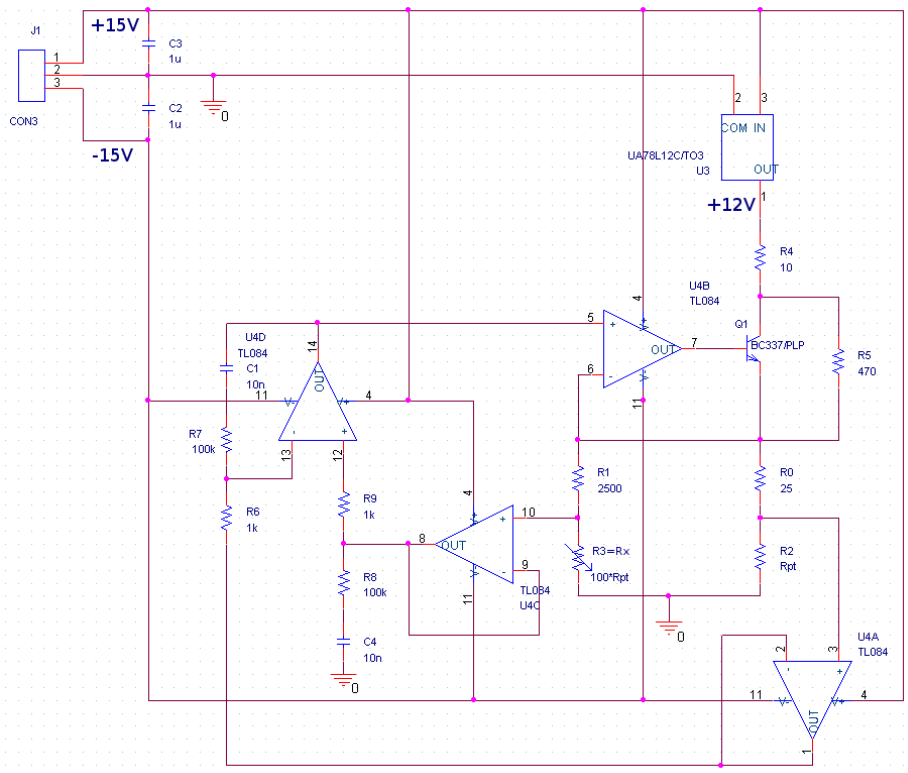

Figure D.1: Schematic

Appendix E

Pubblication and congress

E.1 Pubblication

1. *CZT X-rays detectors obtained by the boron encapsulated vertical Bridgman method*
   M.Pavesi, M.Zanichelli, E.Gombia, R.Mosca, L.Marchini, M.Zha, A.Zappettini, E.Caroli, N.Auricchio, B.Negri;
   SPIE Optics and Photonics, S. Diego (California) 26-30 Agosto 2007, Paper Number: 6706-32.

2. *Characterization of bulk and surface transport mechanisms by means of photocurrent technique*
   M. Zanichelli, M. Pavesi, A. Zappettini, L. Marchini, M. Manfredi.
   2008 IEEE NUCLEAR SCIENCE SYMPOSIUM CONFERENCE RECORD

3. *Boron Oxide Encapsulated Vertical Bridgman Grown CdZnTe Crystals as X-ray Detector Material*
   Andrea Zappettini, Mingzhenh Zha, Laura Marchini, Davide Calestani, Roberto Mosca, Enos Gombia, Lucio Zanotti, Massimiliano Zanichelli, Maura Pavesi, Natalia Auricchio, Ezio Caroli.
   2008 IEEE NUCLEAR SCIENCE SYMPOSIUM CONFERENCE RECORD

4. *Spectoscopic response of CZT detectors obtained by boron encapsulated vertical bridgman method*
   N. Auricchio, L. Marchini, E. Caroli, A. Zappettino, M. Zanichelli, M. quadrini.
   2008 IEEE NUCLEAR SCIENCE SYMPOSIUM CONFERENCE RECORD

5. *Boron Oxide Encapsulated Vertical Bridgman: a Method for Preventing Crystal-Crucible Contact in the CdZnTe Growth*
   A.Zappettini, M.Zha, M.Pavesi, M.Zanichelli, F.Bissoli, L.Zanotti, N.Auricchio and E.Caroli;

IEEE TRANSACTION ON NUCLEAR SCIENCE, Vol. 54 No. 4, August 2007.

6. *Boron Oxide Encapsulated Vertical Bridgman Grown CdZnTe Crystals as X-ray Detector Material*
   Andrea Zappettini, Mingzhenh Zha, Laura Marchini, Davide Calestani, Roberto Mosca, Enos Gombia, Lucio Zanotti, Massimiliano Zanichelli, Maura Pavesi, Natalia Auricchio, Ezio Caroli.
   IEEE TRANSACTION ON NUCLEAR SCIENCE Vol. 56 No. 4, August 2009.

7. *Characterization of bulk and surface transport mechanisms by means of the photocurrent technique*
   Massimiliano Zanichelli, Maura Pavesi, Andrea Zappettini, Laura Marchini, and Manfredo Manfredi.
   IEEE TRANSACTION ON NUCLEAR SCIENCE Vol. 56 No. 6, December 2009.

E.2 Congress

IEEE NSS-MIC-RTSD Congress 19 - 25 Ottobre 2008 Dresden, Germany.

g

Bibliography

[1] S. Ramo *Current induced by electron motion*
Proc. of I.R.E. Sept. 1939, p. 584.

[2] W. Shockley *Current to conductors induced by a moving point charge*
J. Appl. Phys. vol. 9 (1938) 635.

[3] K. Hecht, *Zum mechanismus des lichtelektrischen primärstromes in isolierenden kristallen*
Zeitschrift fur physik A, vol. 77, pp. 235-245, 1932.

[4] A. Many, *High-field effects in photoconducting cadmium sulphide*
J. Phys. Chem. Solids, vol. 26, pp. 575-585, 1965.

[5] K.R. Zanio, W.M. Akutagawa, R. Kikukhi, *Transient Current in Semi.Insulating CdTe Characteristic of Deep Traps*
J. Appl. Phys. vol. 59 n° 6, pp. 2818-2828, May 1968.

[6] W.E. Teffi *Trapping Effects in Drift Mobility Experiments*
J. Appl. Phys. Vol. 38 n° 13, pp. 5265-5272, Dec. 1967.

[7] R.M Blakney, H.P. Grunwald *Small-Signal Current Transient in Insulators with Traps*
Phys. Rev. vol. 159 n° 3, pp. 658-664, 15 Giuly 1967.

[8] D.S. Bale, C. Szeles *Multiple-Scale Analysis of Charge Transport in Semiconductor Radiation Detectors: Application to Semi-Insulating CdZnTe*
J. El. Mat. vol. 38 n°1, 2009, pp. 126-144.

[9] D.S. Bale, C. Szeles *Nature of polarization in wide-bandgap semiconductor detectors under high-flux irradiation: Application to semi-insulating* $Cd_{1-x}Zn_xTe$
Phys. Rev B vol. 77, 035205 (2008)

[10] D.S. Bale, S.A. Soldner, C. Szeles *A mechanism for dynamic polarization in CdZnTe under high-flux irradiation*
Appl Phys. Lett. vol. 92, 082101 (2008)

[11] J. Kubat, J. Franc, R. Grill, P. Horodysky, P. Hlidek, E. Belas *Screening Effects in High Resistivity CdTe for X-ray and Gamma Ray Detectors* J. El. Mat. vol. 36 n° 8, 2007, pp. 871-876.

[12] J. Franc, J. Kubat, R. Grill, P. Höschl *Influence of Space Charge and Potential Fluctuations on Photoconductivity Spectra of Samiinsulating CdTe* IEEE Trans. Nucl. Sci. vol. 54 N° 4, pp. 1416-1420, August 2007.

[13] Z. He *Review of Shockley-Ramo theorem and its application in semiconductor gamma-ray detectors* Nucl. Instr. Meth. A vol. 463 (2001), pp. 250-267

[14] H. Spieler *Semiconductor Detector System* Oxford Science Pubblications 2006.

[15] W.R. Leo *Techniques for Nuclear and Particle Physics Experiments* Springer-Verlag Berlin Heildelberg New York London Paris Tokyo.

[16] *Interazioni radiazione materia* uniroma1.it/DOCS/DISPENSE/dispense/m.mattioli/TInterazioni RadiazioneMateria2002.PDF+interazione+radiazione+materia&cd=2&hl=it&ct=clnk&gl=it&client=firefox-a

[17] T.E. Schlesinger et al. *Cadmium zinc telluride and its use as a nuclear radiation detector material* Materials Science and Engineering 32 (2001) 103-189 and references therein.

[18] M.Prokesch, C.Szeles *Accurate measurement of electrical bulk resistivity and surface leckeage of CdZnTe radiation detector crystals* J.Appl.Phys. 100 (2006) 14503.

[19] C.Szeles, *Advances in the Crystal Growth and Device Fabrication Technology of CdZnTe Room Temperature Radiation Detectors* IEEE Trans. Nucl. Sci. vol. 51, N. 3 (2004), 1242.

[20] Andrea Zappettini, Mingzheng Zha, Maura Pavesi, Massimiliano Zanichelli, Francesco Bissoli, Lucio Zanotti, Natalia Auricchio ed Ezio Caroli, *Boron Oxide Encapsulated Vertical Bridgman: a Method for Preventing Crystal-Crucible Contact in the CdZnTe Growth* IEEE Trans. Nucl. Sci., vol. 54, NO. 4, (2007), 798.

[21] A. Zappettini, T. Görög, M. Zha, L. Zanotti, G. Zuccalli, and C. Paorici, "*A new process for synthesizing high purity stoichiometric cadmium telluride* J. Crystal Growth, vol. 214–215, pp. 14–19, 2000.

[22] J.D. Wiley, Phys. Rev. B 4 (1971) 2485.

[23] K. Suzuki, N. Akita, S. Dairaku, S. Seto, T. Sawada, K. Imai, J. Cryst. Growth 159 (1996) 406.

[24] J. Toney, Ph.D. Thesis, Carnegie Mellon University, 1998.

[25] L.Marchini, *Cristalli di CdZnTe per la rivelazione di raggi X*
Degree Thesis Università degli studi di Parma, Facoltà di Fisica, Anno accademico 2006-2007.

[26] M.A. Lampert *Simplified Theory of Space-Charge Limited Currents in an Insulator with Traps*
Phys. Rev. vol. 103 No. 6, 15 September 1956, pp. 1648-1656.

[27] M.A. Lampert, A. Rose *Volume-Controlled, Two-Carrier Currents in Solids: The Injected Plasma Case*
Phys. Rev. vol. 121 No. 1, 1 January 1960, pp. 26-37.

[28] M.A. Lampert, *Double Injection in Insulators*
Phys. Rev. vol. 125 No. 1, 1 January 1961, pp. 126-141.

[29] K.L. Ashley, A.G. Milnes, *Double Injection in Deep-Lying Impurity Semiconductors*
J. Appl. Phys. vol. 35 No. 2, February 1964.

[30] R. Baron, *Effects of Diffusion on Double Injection in Insulators*
Phys. Rev. vol. 137 No. 1A, 4 January 1965

[31] G. Lutz, *Semiconductor Radiation Detectors*
Springer (2007)

[32] Y. Nemirovsky, A. Ruzin, G. Asa, and J. Gorelik, *Study of the Charge Collection Efficiency of CdZnTe Radiation Detectors*
J. El. Mat. vol. 25 No. 8, 1996, pp.1221-1231.

[33] Y. Nemirovsky, A. Ruzin, G. Asa, and J. Gorelik, *Study of Contacts to CdZnTe Radiation Detectors*
J. El. Mat. vol. 26 No. 6, 1997, pp. 756-764.

[34] R.T. Tung, *Recent advances in Shottky barrier concepts*
Mat. sci & Eng. R 35 (2001) pp. 1-138.

[35] A. Zappettini, M. Zha, L. Marchini, D. Calestani, R. Mosca, E. Gombia, M. Zanichelli, M. Pavesi, N. Auricchio, and E. Caroli, *Boron Oxide Encapsulated Vertical Bridgman Grown CdZnTe as X-ray Detector Material*
IEEE Trans. Nucl. Sci. VOL. 56, NO. 4, AUGUST 2009. 2008 IEEE Nuclear Science Symposium Conference Record R05-1.

[36] M. Briza, J. Willekens, M.L. Benkhedir, E.V. Emilianova, G.J. Adriaenssens, *Photoconductivity methods in materials research*
J. Mat. Sci.: Mat. in El. 16 (2005) pp. 703-713.

[37] R.H. Bube, *Photoelectronic Properties of Semiconductors* Canbridge University Press (2004)

[38] T.S. Moss, *Photoconductivity*
Rep. Prog. Phys. 28 1965, pp.15-60.

[39] S. Sikorski, T. Piotrowski, *Photovoltaic phenomena in inhomogeneous semiconductors*
Prog. Quant. El. 27 (2003) 295–365, Review.

[40] Y. Cui, M. Groza, D. Hillman, A. Burger, and R.B. James, *Study of surface recombination velocity of* $Cd_{1-x}Zn_xTe$ *radiation detectors by direct current photoconductivity*
J. of Appl Phys. 92, p. 2556 (2002)

[41] J. Franc, P. Hlidek, E. Belas, V. Linhart, S. Propisil, and R. Grill, *Photoconductivity Spectroscopy of Deep Levels in CdTe*
IEEE Trans. Nucl. Sci. vol. 52 N° 5, pp. 1956-1960, October 2005.

[42] A. Zumbiehl, S. Mergui, M. Ayoub, M. Hage-Ali, A. Zerrai, K. Cherkaoui, G. Marrakchi, and Y. Darici, *Compensation origins in II-VI CZT materials*
Mater. Sci. Eng. B, vol. 71, no. 1, p. 297, 2000.

[43] Y. Du, J. LeBlanc, G.E. Possin, B.D. Yanoff, and S. Bogdanovich, *Temporal Response of CZT Detectors Under Intense Irradiation*
IEEE Trans. Nucl. Sci, vol. 50, No. 4, August 2003

[44] M. Pavesi, M. Zanichelli, E. Gombia, R. Mosca, L. Marchini, M. Zha, A. Zappettini, E. Caroli, N. Auricchio, B. Negri *CZT X-ray detectors obtained by the boron encapsulated vertical Bridgman method*
Proc. of SPIE Vol. 6706 67060X-2 S. Diego (CA) 2007.

[45] M. Zanichelli, M. Pavesi, A. Zappettini, L. Marchini, N. Auricchio, E. Caroli, and M. Manfredi, *Characterization of Bulk and Surface Transport Mechanisms by Means of the Photocurrent Technique*
IEEE Trans. Nucl. Sci vol. 56 No 6, december 2009, pp. 3591-3596.

[46] N. Auricchio, L. Marchini, E. Caroli, A. Donati, A. Zappettini, M. Zanichelli, and M. Quadrini, *Spectroscopic response of CZT detectors obtained by the boron encapsulated vertical Bridgman mathod*
2008 IEEE Nuclear Science Symposium Conference Record R12-30.

[47] Y. Cui, M. Groza, A. Burger, and R.B. James, *Effects of surface Processing on the performance of Cd1-xZnxTe radiation detectors*
IEEE Trans. Nucl. Sci. vol. 51 (3), p. 1172 (2004)

[48] T.H. Prettyman, M.A. Hoffbauer, J.A. Rennie, S. Cook, J.C. Gregory, M.A. George, P.N. Luke, M. Amman, S.A. Soldnre, and J.R. Earnhart, *Performance of CdZnTe detectors passivated with energetic oxigen atoms*
Nucl. Instr. Meth. Phys. Res. A 422, p. 179 (1999)

[49] Q. Li, W. Jie, L. Fu, and G. Zha, *Investigation on interface barrier of Au–CdZnTe contacts*
Nucl. Instr. Meth. Phys. Res. A 564, p. 544 (2006)

[50] G. Zha, W. Jie, T. Tan, and X. Wang, *Effect of surface treatments on the electrical and optical properties of CdZnTe single crystal*
Nucl. Instr. Meth. Phys. Res. A 566, p. 495 (2006)

[51] J.M. Cardoso, J. Basílio Simões, T. Menezes, and C.M. B. A. Correia, *CdZnTe spectra improvement through digital pulse amplitude correction using the linear sliding method*
Nucl. Instr. Meth. Phys. Res. A 505, p. 334 (2003)

[52] N. Auricchio, A. Basili, E. Caroli, A. Donati, T. Franceschini, F. Frontera, M. Hage-Ali, G. Landini, A. Roggio, F. Schiavone, J. Buchan Stephen, and G. Ventura, *Compensation of CdZnTe signals using a twin shaping filter technique*
IEEE Trans. Nucl. Sci. vol. 51 (5), p. 2485 (2004)

[53] Y. Cui, G.W. Wright, X. Ma, K. Chattopadhyay, R.B. James, and A. Burger, *DC photoconductivity study of semi-insulating $Cd_{1-x}Zn_xTe$ Crystals*
J. of El. Mat. 30, p. 774 (2001)

[54] K. Hoshikawa, H. Nakanishi, H. Kohda, and M. Sasaura, *Liquid encapsulated, vertical bridgman growth of large diameter, low dislocation density, semi-insulating GaAs*
J. Crystal Growth 94, p. 643 (1989)

[55] F. Matsumoto, Y. Okano, I. Yonenaga, K. Hoshikawa, and T. Fukuda, *Growth of twin-free ¡100¿ InP single cystals by the liquid encapsulated vertical Bridgman technique*
J. Crystal Growth 132 p. 348 (1993)

[56] K. Nakagawa, K. Maeda, and S. Takeuchi, *Observation of dislocations in cadmium telluride by cathodoluminescence microscopy*
Appl. Phys. Lett. 34, p. 74 (1979)

[57] S. Wenbin, W. Kunshu, M. Jiahua, T. Jianyoung, Z. Qi, and q. Yongbiao, *A novel two-step chemical passivation process for CdZnTe detectors*
Semicond. Sci. Technol. 20, 343 (2005)

[58] C.J. Johnson, E.E. Eissler, S.E. Cameron, Y. Kong, S. Fan, S. Janovic, and K.G. Lynn in R.B. James, T.E. Schlesinger, P. Siffert, and L. Franks, Editors, *Semiconductors for room-temperature radiation detector applications* vol. 302, Academic Press, New York (1993), p.463

[59] N. Krsmanovic, K.G. Lynn, M.H. Weber, R. Tjossem, Th. Gessmann, C. Szeles, E.E. Eissler, J.P. Flint, and H.L. Glass, *Electrical compensation in*

CdTe and $Cd_{0.9}Zn_{0.1}Te$ by intrinsic defects
Phys. Rev. B 62 (24), pp. R16279-82 (2000)

[60] P. Höschl, Yu.M. Ivanov, E. Belas, J. Franc, R. Grill, P. Hlidek, P. Moravec, M. Zvara, H. Sitter and A.L. Toth, *Electrical and luminescence properties of (CdZn)Te single crystals prepared by the vertical gradient freezing method*
J. Crystal Growth, vol. 184–185 p. 1039 (1998)

[61] G. Yang and W. Jie, *Photoluminescence analysis of $Cd_{1-x}Zn_xTe$ single crystals annealed by a two-step method*
J. Crysal Growth, vol. 294 (2), pp. 250-253 (2006)

[62] S. Del Sordo, L. Abbene, M. Zora, G. Agnetta, B. Biondo, A. Magnano, F. Russo, E. Caroli, N. Auricchio, A. Donati, F. Schiavone, J.B. Stephen, G. Ventura, G. Bertuccio, S. Caccia, and M. Sampietro, *Characterization of a CZT focal plane small prototype for hard X-ray telescope*
IEEE Trans. Nucl. Sci., vol. 52, pt. Part 2, pp. 3091-3095 (2005)

[63] I. Farella, A. Cola, E. CAroli, A. Donati, W. Dusi, G. Ventura, and E: Perillo, *Charge transients locally induced by laser pulses in CdTe planar and multi-strip detectors*
IEEE Trans. Nucl. Sci., vol. 52, pp. 1968-1974 (2005)

[64] J. Franc, P. Hlidek, E. Belas, V. Linhart, S. Prospisil, and R. Grill, *Photoconductivity Spextroscopy of Deep Levels in CdTe*
IEEE Trans. Nucl. Sci. vol. 52 No. 5, October 2005.

[65] A. Iribarren, E. Menéndez-Proupin, R. Castro-Rodríguez, V. Sosa, J.L. Peña, and F. Caballero-Briones, *Experimental evidence of compositional CdTeO films grown by radio frequency sputtering*
J. Appl. Phys., vol. 86, p. 4688, 1999.

[66] H. Tetsuka, Y. J. Shan, K. Tezuka, and H. Imoto, *Electronic structure calculations of transparent conductor Cd TeO : Optical properties and the effect of In-substitutio*
Solid State Commun., vol. 137, p. 345, 2006.

[67] A.A. Dakhel and F.Z. Henari, *Optical characterization of thermally evaporated CdO films*
Cryst. Res. Technol., vol. 38, p. 979, 2003.

[68] Y. Cui, M. Groza, G.M. Wright, U.N. Roy, A. Burger, L. Li, F. Fu, M.A. Blank, and R.B. James, *Characterization of $Cd_{1-x}Zn_xTe$ Crystals Grown from a Modified Vertical Bridgmann Technique*
J. of El. Mat. vol. 35 No. 6 2006, pp.1267-1274.

[69] J. D. Eskin, H.H. Barrett, and H. B. Barber, *Signals induced in semiconductor gamma-ray imaging detectors*
J. Appl. Phys. vol. 85, No. 2, 15 January 1999.

[70] A. Gliere, M. Rosaz, L. Verger, *Simulation of CdZnTe gamma-ray spectrometer response*
N.I.M. A 442 (2000) 250-254

[71] M. Picone, A. Gliere, P. Massé, *A three-dimensional model of CdZnTe gamma-ray spectrometer*
N.I.M. A 504 (2003) 313–316.

[72] N. Auricchio *Rivelatori di CdZnTe sensibili alla posizione per missioni spaziali in raggi X duri*
Ph. D. thesys, Università degli studi di Bologna, Dottorato di ricerca in Fisica XVII Ciclo.

[73] N. Auricchio, L. Amati, A. Basili, E. Caroli, A. Donati, T. Franceschini, F. Fontera, G. Landini, A. Roggio, F. Schiavone, J.B. Stephen, and G. Ventura. *Twin Shaping Filter Techniques to Compensate the Signals From CZT/CdTe Detectors* IEEE Trans. Nucl. Sci. vol. 52, No. 5, October 2005

[74] R. Redus, M. Squillante, J. Lund, *Electronics for high resolution spectroscopy with compound semiconductors* N.I.M. A 380 (1996) 312-317

[75] J.C. Lund, R.Olsen, J.M.Van Scyoc ,and R.B. James, *The Use of Pulse Processing Techniques to Improve the Performance of $Cd_{1-x}Zn_xTe$ Gamma-Ray Spectrometers*
IEEE Trans. Nucl. Sci. vol. 43, No. 3, June 1996.

[76] C. Bargholtz, E. Fumero, L. Martensson, S. Wachtmeister, *Digital pulse-shape processing for CdTe detectors* N.I.M. A 471 (2001) 290–292